UNIVERSITY of CALIFORNIA
Santa Barbara

Effective temperature and strain localization in amorphous solids

A dissertation submitted in partial satisfaction of the
requirements for the degree of

Doctor of Philosophy

in

Physics

by

M. Lisa Manning

Committee in charge:

Professor Jean M. Carlson, Chair
Professor Ralph J. Archuleta
Professor James S. Langer

September 2008

The dissertation of M. Lisa Manning is approved:

Professor Ralph J. Archuleta

Professor James S. Langer

Professor Jean M. Carlson, Chair

May 2008

Effective temperature and strain localization in amorphous solids

M. Lisa Manning

To Mom and Dad

Acknowledgements

First I would like to thank Jean Carlson and Jim Langer for their incredible mentorship. I am grateful that Jean continuously encouraged me to work broadly and collaboratively. I never would have chosen to give that many group presentations, but now I'm very glad I did. I would like to thank Jim for being patient and encouraging. He made me feel like a peer, even though it took me awhile to catch up with his thinking about new concepts. Jean and Jim have obviously worked to create an environment where academic research is fun and there is no such thing as a stupid question. I hope to pass on this sense of adventure and openness to my own students someday.

I would also like to thank Bassam Bamieh for all of his insight and persistence. He was willing to work through the details of fluid dynamics calculations when no one else would, and he was patient while I learned the rudiments of numerical differentiation and integration.

Many thanks to my officemates and fellow troublemakers Sean and Eric. They put up with my cursing at inanimate objects and sports teams, and generally made life a lot better when they weren't stealing my tissues. I'd especially like to thank Morgan for her friendship, support, and great advice. I'm know that I couldn't have handled all the things that go with being a woman in physics without her, and I really appreciate her blazing a trail ahead of me and sharing her wisdom. Thanks, too to Eric Dunham for his timely advice concerning graduate schools and his instrumental support during job hunting season.

I'd also like to recognize all the people who have helped me with research questions and problems. Thanks to Craig Maloney and Anthony Foglia for discussing the nuances of molecular dynamics simulations and STZ theory. Thanks to Michael Falk, Yunfeng Shi, and Thomas Haxton for sharing their time, expertise, and simulation data. For useful discussions I'd like to thank Gregg Lois, Gregor Hillers, Doron Bergman, Boris Shraiman, Ralph Archuleta, Ben Callahan, and Wouter Ellenbroek.

Finally, I can't begin to express my thanks to Will. He's been my rock through five years of graduate school – his love, support, generosity, and encouragement made my success possible. Many men would be intimidated or threatened by a strong-willed physics Ph.D. student, but Will has always encouraged me to reach as high as I can. Thank you for everything!

Curriculum Vitæ

M. Lisa Manning

Education

2008	PhD in Physics, University of California, Santa Barbara
2005	MA in Physics, University of California, Santa Barbara
2002	BSc in Physics, University of Virginia
2002	BA in Mathematics, University of Virginia

Publications

M. Manning, J. M. Carlson, and J. Doyle, "Highly Optimized Tolerance in dense and sparse resource regimes," *Phys. Rev. E* **72**, 016108 (2005).

M. L. Manning, J. S. Langer, and J. M. Carlson, "Strain localization in a shear transformation zone model for amorphous solids," *Phys. Rev. E* **76** 056106 (2007).

J. S. Langer and M. L. Manning, "Steady-state, effective-temperature dynamics in a glassy material," *Phys. Rev. E* **76** 056107 (2007).

M. Lisa Manning, B. Bamieh, and J. M. Carlson. "Eliminating spurious eigenvalues in the analysis of hydrodynamic stability," ArXiV 0705.1542 (2007).

E. G. Daub, M. L. Manning, and J. M. Carlson, "Shear strain localization in elastodynamic rupture simulations," *Geophys. Res. Lett.* (2008).

Honors and Awards

2008. Princeton Center for Theoretical Physics Postdoctoral Fellowship.
Princeton University

2004-present. National Science Foundation Graduate Research Fellowship.
National Science Foundation

2007. Department Chair's Certificate of Appreciation.
UCSB Department of Physics

2007. Southern California Earthquake Center Research Grant.
PI: Jean Carlson

2006. Boulder School for Condensed Matter Physics.
University of Colorado, Boulder

2003-2004. National Science Foundation Graduate K-12 Education Fellowship.
National Science Foundation

2004, 2005, 2006. Physics Circus Outreach award.
UCSB Department of Physics

2002. Barry M. Goldwater Scholarship. *University of Virginia*

2002. Elected to Phi Beta Kappa. *University of Virginia*

2001. Elected to Pi Mu Epsilon. *University of Virginia*

Abstract

Effective temperature and strain localization in amorphous solids

by

M. Lisa Manning

Many important natural and fabricated systems, such as dense complex fluids, plastically deforming solids, and earthquake faults are currently described by phenomenological models. While these models are useful for predicting macroscopic behavior in typical situations, they may fail in extreme situations and provide little insight into the microscopic mechanisms that give rise to the large-scale behavior. A more detailed theory for the microscopic dynamics generates macroscopic relations which are more accurate and widely applicable than those currently used, for example, to model physical processes from nano-fabrication to earthquake simulations. Conversely, insights from studying far-from-equilibrium systems with many degrees of freedom can be used to generalize concepts from statistical physics and suggest new directions for theory and experiments.

The goal of this work is to characterize and predict deformation and failure in amorphous or disordered solids, such as bulk metallic glasses, granular fault gouge, dense colloids, and bubble rafts. In this dissertation, a micro-structural Shear Transformation Zone (STZ) model is shown to capture features such as strain localization and onset of material failure in amorphous materials. We identify the effective temperature, which specifies the configurational disorder of the particles, as an important state variable or order parameter.

Using data from steady-state simulations of an amorphous solid over a wide range of temperatures and applied strain rates, we find that a rate-dependent effective temperature governs plasticity in these materials. In addition, we show that the rate-dependence can be understood as a glassy process where plasticity is activated by the effective temperature. We explain strain localization as a transient feature generated by feedback between energy dissipation and effective-temperature governed plasticity, and show that a frozen-time instability in the transient dynamics predicts shear band formation based on the initial conditions alone. Quantitative agreement between the STZ model and time-varying simulations validate this model.

We determine a deformation map which predicts the type of deformation (homogeneous, thick shear band, thin shear band, or melting/failure) as a function

of applied strain rate and the quenching procedure, which determines the initial structural disorder. This work explains the experimental result that shear banding is not governed by thermal temperature, and it predicts that slowly quenched amorphous systems are more likely to fail via shear banding than quickly quenched systems. In addition, a model for gouge on earthquake faults which includes rate-dependent effective temperature is shown to generate thin failure bands and dynamic weakening, and provides a novel explanation for these phenomena which are seen in observations of earthquake faults and friction experiments.

This work suggests that universal features in a wide range of amorphous materials can be explained using a simple continuum model, analogous to the Navier-Stokes equation for simple fluids, which explicitly accounts for configurational disorder.

Contents

Chapter 1

Introduction

1.1 Models for friction and deformation

Strength, flexibility, plasticity, resilience, aging, and wear are among the essential mechanical properties describing a wide range of natural and manufactured materials. In recent years it has become increasingly clear that developing reliable estimates for the characteristics of materials under stress requires more sophisticated information than can be obtained from traditional laboratory measurements.

For engineering or design purposes, materials like films, foams, and rocks are currently described by phenomenological laws based on fits to data. While these laws are useful for predicting macroscopic behavior in most typical situations, they do not predict the onset of fracture, deterioration, and propagation of cascading failure, which can be sudden, unexpected, and extremely sensitive to the history of the material. Such fragilities are often intrinsically linked to feedback between systems at different scales, such as granular fault gouge and networks of faults spanning hundreds of miles.

One example of this paradigm is friction models for sheared rock or granular surfaces. The simplest is the static-dynamic model found in elementary physics texts, which states that the ratio of the shear stress to the normal stress is a constant, μ_s, under static conditions, and a different constant, μ_k, once the surfaces begin to move. Figure 1.1(a) is a diagrammatic plot of the stress as a function of slip in this model. Note that the stress changes instantaneously from one value to another, which is unphysical and problematic. A more reasonable model, often used to fit seismic data, is "slip-weakening", where the friction coefficient decays linearly from its static value to a dynamic sliding value as shown in Fig. 1.1(b). Note that the friction is a single-valued function of a single variable: $\mu = \mu(d)$. The Stribeck curve, which models thin film lubricants, predicts that the friction

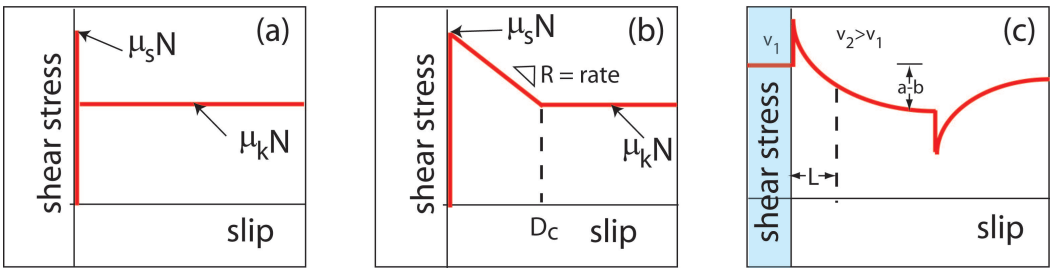

Figure 1.1: A schematic diagram of the friction response for various theoretical friction models. (a) Shear stress vs. slip for the simplest static-dynamic friction law. The difference between the static and dynamic stress is called the "stress drop".This model is unphysical because the macroscopic stress variable changes instantaneously. (b) Shear stress vs. slip for the linear slip-weakening law. R represents the weakening rate, and D_c is the distance over which the friction coefficient evolves. (c) Shear stress vs. slip for a velocity step experiment described by rate-and-state friction. In this case the slip velocity must be specified because the state variable changes as a function of time and driving velocity.

coefficient decays with velocity, $\mu = \mu(v)$. Although these laws are useful, they fail to capture important an features of real friction experiments — history dependence. Models that depend on a single variable predict the same behavior independent of age or other initial conditions. In contrast, thin films, rocks, and granular materials exhibit a frictional response that depends on how long the system has been at rest and how fast it is driven.

This aging and history dependence suggests that the internal state of the interface changes as a function of time. In other words, the interface possesses internal degrees of freedom that must be accounted for in frictional models. In principle, these internal degrees of freedom could be arbitrarily numerous and complex. However, it would be fortuitous if the state dynamics could be approximated by a few or even a single parameter, much as the thermal temperature determines the properties of a thermodynamic equilibrium ideal gas.

This is exactly the assumption made in the widely used rate-and-state friction models. These models write the friction parameter as a function of the velocity (v) and a state variable (θ) that evolves dynamically in time, $\mu = \mu(v, \theta)$. They are attractive because they predict that different histories lead to different dynamic friction coefficients, as seen in experiments. One example that is popular in the

earthquake community is the Dieterich-Ruina rate-and-state friction law [1, 2]:

$$\mu = \mu_0 + a \ln \left(\frac{V}{V_0} \right) + b \ln \left(\frac{V_0 \theta}{D_c} \right) \tag{1.1}$$

$$\frac{d\theta}{dt} = 1 - \frac{V\theta}{D_c} \tag{1.2}$$

where μ is the friction coefficient, θ is a phenomenological state variable with the dimensions of time, V is the slip velocity, D_c is a critical slip distance and a and b are material-dependent parameters. Figure 1.1(c) is a plot of the DR prediction for stress vs. slip in a velocity step experiment.

This law provides an accurate description of dynamic friction for many different materials at the low velocities studied in typical friction laboratory experiments. Furthermore, the state variable θ has been associated with a physical process: the increase of contact area between surfaces with contact age, and θ is interpreted as the amount of time that asperities have been in contact [3]. However, there is no theoretical derivation for the equation of motion for θ — what microscopic dynamics give rise to this macroscopic behavior, and why is a single macroscopic state variable sufficient to capture the low-velocity dynamics?

Understanding the answers to these questions becomes particularly important in light of more recent high velocity experiments. Many traditional experiments study friction at velocities on the order of 1 μm/s [4], while earthquakes rupture at speeds in excess of 1 m/s. More recent experiments at near-seismic speeds provide evidence for dynamic weakening: the friction coefficient drops from 0.6 to about 0.2 or less at high speeds [5, 6]. Unfortunately, because the rate-and-state laws are essentially a fit to data, they neither predict nor explain these high velocity experiments. An additional phenomenological term has recently been added to the Dieterich-Ruina law to model this dynamic weakening [7], but this is also simply a fit to data. In order to explain and predict friction in atypical or novel situations, we must be able to derive these friction laws from microscopic physics. This has never before been accomplished.

Much of this dissertation is devoted to developing and analyzing such a model. Interestingly, we find that in many cases a quasi-thermodynamic state variable is able to adequately describe the state of a sheared interface, although the dynamics of the state variable are far from trivial. These small-scale details are important because studies have shown that changes to the details of the rate-and-state equation lead to large changes in seismic waves away from the fault [8, 9, 10], with far-reaching implications for hazard analysis [4, 10].

In addition to earthquake faults bridged by granular fault gouge, there are many examples of important engineering materials that exhibit interesting and

unexpected frictional behavior or failure modes when driven out of equilibrium by shear forces. We now discuss thin film lubricants and bulk metallic glasses, two seemingly disparate systems which are similar to fault gouge in that they possess an amorphous structure. As discussed in Section 1.2, these materials may appear to be very different but their disordered configurational state leads to universal deformation mechanisms.

At the smallest scales, control systems for engineered nanoscale devices require an accurate model for friction between sheared, lubricated interfaces. However, simple friction laws can not capture the rich behavior of these microscopically thin films, which exhibit a yield stress like a solid and can be either amorphous or ordered. A surface force apparatus (SFA) [11, 12], which measures shear forces on a microscopically thin layer of lubricant between atomically smooth surfaces, reveals a wide range of interesting behavior such as crystal-like layering [13, 14] and stick-slip instabilities [15, 16].

Bulk metallic glasses are another type of amorphous materials useful for engineering purposes. In contrast to typical metals, which are crystalline within grain boundaries, these novel multi-component metals have been quenched rapidly and remain in a structurally amorphous state. Bulk metallic glasses are extremely tough and show great promise as structural materials [17], but they fail catastrophically via shear banding [18]. Shear bands are extremely thin regions where the material deforms rapidly and eventually breaks.

Before these materials can be used reliably in manufacturing, the mechanisms that generate shear bands must be understood so that material failure can be predicted. An old explanation, first proposed by Griggs and Baker [19], is that thermal temperature-viscosity feedbacks explain these bands. They suggest that heat generated by plastic work raises the thermal or kinetic temperature. Regions with higher thermal temperatures have a lower viscosity and deform more easily, resulting in more plastic energy dissipation.

However, Lewandowski and Greer [20] have shown that in a bulk metallic glass the thermal temperature diffuses too quickly to control shear localization in an adiabatic description. Adiabatic temperature rise and diffusion predicts a shear band width of 100-240 nm, while experiments measure the width to be 10-20 nm [20]. Therefore a new theory is required to explain strain localization in these materials, as well as in athermal materials such as granular fault gouge.

1.2 Amorphous materials: definition and phenomena

Although ruptures on earthquake faults, nanoscale friction measured using a SFA, and deformation in bulk metallic glasses appear to be very different phenomena, they share a common feature: the region where deformation or slip occurs is populated by an amorphous material. Amorphous solids are comprised of particles (atoms, grains, bubbles, molecules) arranged so that the locations of their centers of mass are disordered; their structure is essentially indistinguishable from a liquid. However, these materials are "jammed" and exhibit a yield stress like a solid. Other examples of amorphous materials include colloids and emulsions, foams, glass-forming molecular liquids, traffic jams, and even living tissue.

While amorphous materials differ in important and significant ways, they exhibit common features which we explain using a single continuum formalism. One such feature is a mode of deformation or failure called shear banding or strain localization. Strain localization is the spontaneous development of coexisting flowing and stationary regions in a sheared material. Newtonian fluids exhibit a simple relationship between shear stress and strain rate:

$$\text{stress} = \text{viscosity} \times \text{strain rate} \tag{1.3}$$

Fig. 1.2(a) illustrates the steady state of a fluid driven in simple shear. The fluid maintains a constant shear stress, resulting in a constant strain rate and a linear Couette velocity profile. In contrast, amorphous materials driven in simple shear often exhibit a very different velocity profile, shown diagrammatically in Fig. 1.2(b). In this case, two pieces of the material move with the boundaries, resulting in a thin band of deformation somewhere in between. The resulting spike in the strain rate as a function of position is called a shear band. The band is shown in the center of the specimen in Fig. 1.2(b), but it can also occur along the boundaries.

Strain localization has been identified and studied experimentally in granular materials [21, 22], bubble rafts [23, 24], complex fluids [25, 26], and bulk metallic glasses [18, 27]. Localization is a precursor to fracture in bulk metallic glasses [18] and occurs in small scale experiments on granular materials [28]. Figure 1.3 is a photograph of a bulk metallic glass that failed under compression via a thin shear band.

Significantly, exhumed earthquake faults also exhibit a narrow shear band called a *prominent fracture surface* that occurs within the gouge layer that exists at fault interfaces, as shown in the monograph of the exhumed Punchbowl fault

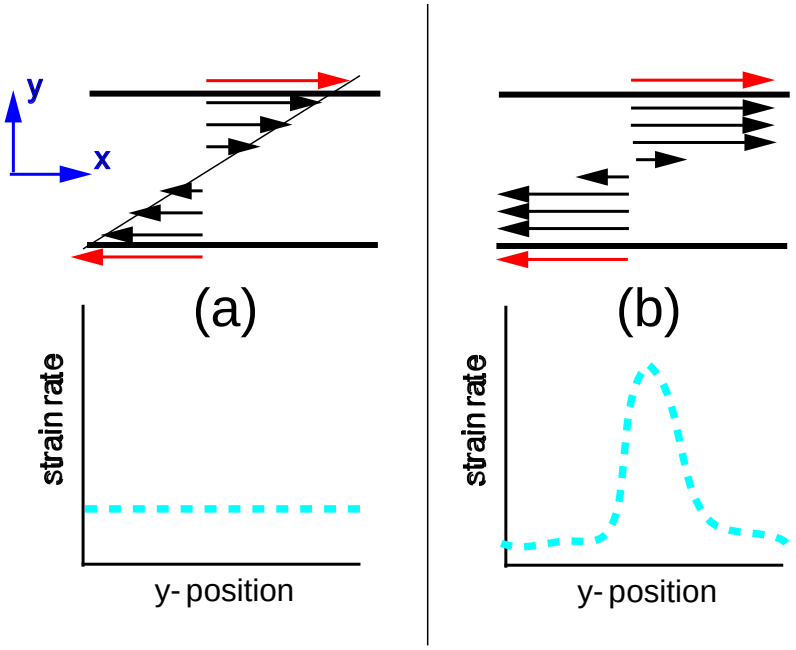

Figure 1.2: Schematic diagram comparing (a) homogeneous flow to (b) shear localization. Newtonian fluids exhibit a linear Couette velocity profile (top left) and constant strain rate(bottom left). In contrast, many amorphous solids deform inhomogeneously, where the velocity profile changes rapidly at a particular location (top right) and the strain rate has a sharp peak (bottom right).

in Fig. 1.4 [29]. One goal of this work is to understanding the mechanisms that lead to strain localization.

It seems likely that not all shear bands are generated by the same mechanism. Recently, Falk *et al.* have shown that stress variations are likely responsible for the shear bands seen in granular solids filling a circular Couette cell [30]. In contrast, this work focuses on shear bands that arise in simple shear, where the shear stress rapidly equilibrates to a constant within the material. Although stress-mediated shear bands are interesting, the bands that occur even when the stress is constant indicate that there must be another internal state parameter that determines the preferred local strain rate. Focusing on these bands allows us to understand the structural changes that lead to failure in a wide range of materials.

The Navier-Stokes equations are an excellent continuum model for predicting stress and strain in Newtonian fluids; a similar continuum description for amorphous solids has remained elusive. Amorphous materials require more complicated constitutive equations than simple fluids or crystalline solids. They flow like a fluid

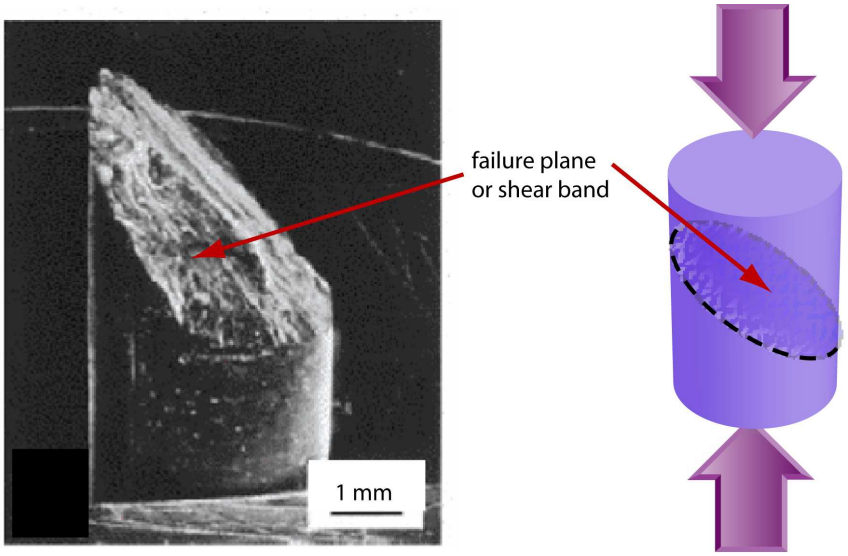

Figure 1.3: Photograph from W. Johnson's experimental group at Caltech showing bulk metallic glass failure. A rod of the glass is placed under compression and fails along a very thin shear band. The surface where failure occurs exhibits fluid-like flow structures, suggesting ductile deformation before failure [18].

under large stresses, creep or remain stationary under smaller stresses, and exhibit complex, history-dependent behavior such as strain localization. Beach sand provides a familiar example of this behavior. Dry sand supports the static load of a person standing on the beach (unlike water or quicksand), but flows like a fluid through the fingers of a person who picks up a handful.

The microscopic mechanisms that give rise to the macroscopic Navier-Stokes equations are well-understood. In contrast, engineers generally use empirical laws determined from fits to data to model friction and deformation in amorphous solids. These laws provide little insight into the microscopic mechanisms and feedbacks that give rise to the macroscopic behavior. Another goal of this work is to provide a model based on microscopic mechanisms to describe deformation and friction in amorphous solids such as granular fault gouge and bulk metallic glasses. Parameters of this model can be associated with physical attributes, such as grain size and stress activation energies. Another attractive feature of microscopic models is that they remain valid at high speeds and identify physical mechanisms for dynamic weakening and shear banding.

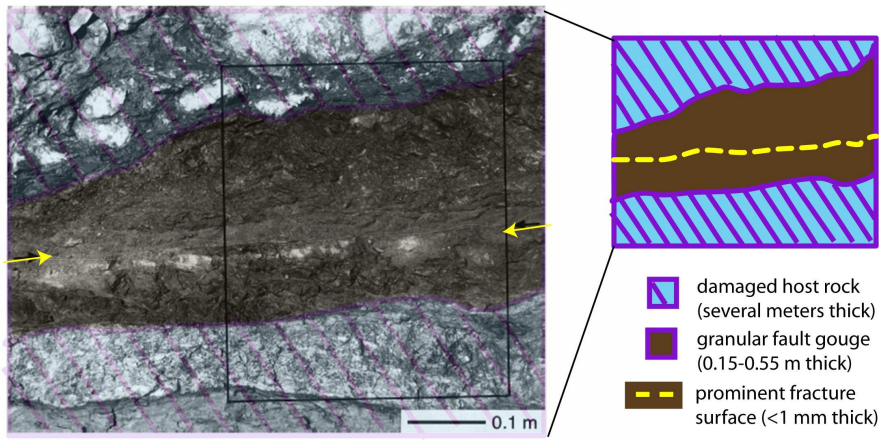

Figure 1.4: Photograph by Chester and Chester of exhumed punchbowl fault [29]. Damaged rock extends far beyond the fault zone, while granular fault gouge extends for 0.15-0.55 m. Chester and Chester find that most of the slip is accommodated in a 1 mm wide *prominent fracture surface* within the fault gouge. This suggests that strain localization occurs within the gouge.

1.3 The physics of far from equilibrium systems

If amorphous materials are ubiquitous in important natural and engineering applications, why are they still so poorly understood? One reason is that these materials are far from equilibrium. To create a glassy state in many molecular liquids, for example, one must cool or quench the system quickly to ensure that it gets stuck in a metastable disordered state instead of the lowest energy equilibrium crystalline state. The nature of the glass transition [31] – whether it is a true thermodynamic phase transition or if it possesses universal characteristics – is a fundamental question in physics that has been studied for over 50 years and remains unresolved.

Recently, focus has broadened to the more general *jamming* transition which occurs when a disordered gas or liquid suddenly develops a yield stress as a control parameter is varied. Liu and Nagel have proposed a jamming phase diagram as a function of three independent control parameters: the particle density, the thermal temperature, and the applied stress [32]. Although the thermal temperature has often been used as a control parameter for investigating glassy dynamics, new insights from density and shear stress studies continue to shed light on the

jamming transition. In particular, work to characterize the relationship between jamming, local structural order, and global boundary conditions have discovered new signatures of the jamming transition, such as a plateau in the density of states at low frequencies [33]. Additionally, Henkes *et al.* have shown that a conservation principle based on the mechanical stress tensor leads to a statistical framework for static amorphous packings near the jamming transition [34].

One difficulty in describing non equilibrium systems is that the thermal temperature no longer completely characterizes probability distributions for the system's many degrees of freedom. For example, the thermal temperature specifies the velocity and position distributions of particles in an equilibrium gas, while the thermal temperature reveals very little about a glass-forming liquid well below the glass temperature or a dense colloidal suspension driven in simple shear. Physicists have long searched for an internal variable that can be used to characterize far from equilibrium systems.

Mehta and Edwards [35] were perhaps the first to point out that although thermal temperature does not determine statistical distributions for macroscopic particles such as powders, the statistical properties of these systems could still be characterized by a small number of macroscopic state variables, such as free volume. The fundamental thermodynamic definition of the temperature is:

$$\frac{1}{T} = \frac{\partial S}{\partial E}, \tag{1.4}$$

where T is the thermal temperature, E is the energy and S is the entropy [36]. In analogy, Mehta and Edwards proposed that in stirred or shaken powders, the *compactivity*, χ plays the role of temperature:

$$\frac{1}{\chi} = \frac{\partial S}{\partial V}, \tag{1.5}$$

where V is the volume occupied by powder grains. This definition is based on the intuition that for many systems thermal temperature is not sufficient to cause configurational rearrangements, but slow shearing or stirring causes the particles to ergodically explore configuration space. This is an *entropic* definition of effective temperature.

Additionally, Cugliandolo, Kurchan, and Peliti [37] have shown that an effective temperature describes violation of the fluctuation-dissipation theorem (FDT) seen in slowly stirred and aging glassy systems. In several example systems, they show that the relationship between fluctuation and response is given by $1/T$ (as predicted by FDT) over short time scales but is given by X/T over longer time scales, where X is an FDT violation parameter. In other words, a thermometer

in contact with a glass will read the thermal temperature if the the response time for the thermometer is fast, but a thermometer with a slow response time will read a different, *effective temperature*, $\chi = T/X > T$. (Thermometers used in everyday life are "fast" – they respond quickly to changes in temperature, but a "slow" thermometer can be constructed from a system with a very slow relaxation time, such as a viscous fluid.) While some simple models predict a single effective temperature, other models possess an entire hierarchy of effective temperatures at different response frequencies. This is a *FDT* definition of effective temperature.

Simulations of a densely packed, sheared foam by Ono *et al.* [38] suggest that both the entropic and FDT equations define the *same* effective temperature. In these simulations the authors first calculate effective temperatures using various FDT definitions: they measure the fluctuations and linear response of several observables (pressure, shear stress, energy and particle diffusivity) and find that a single strain-rate dependent effective temperature describes the system response. In addition, they calculate the effective temperature using an entropic definition, $1/\chi = \partial E/\partial S$, where E is the total potential energy of the foam, and the entropy S is calculated by counting the number of possible configurations of the foam bubbles. (There is no kinetic contribution to the energy because the bubbles are massless.) While the FDT and entropic definitions can only be measured in non-overlapping strain rate regimes, the data are consistent with a single effective temperature.

These results are very encouraging; they suggest that a single effective temperature describes the configurational degrees of freedom in slowly sheared amorphous packings. In other words, the effective temperature is a internal state parameter, much like an order parameter, that specifies the disorder in configurational packings. By combining a heat equation that accounts for effective temperature with a model for particle rearrangements, we generate a model for deformation in amorphous materials.

1.4 Macroscopic models for disordered solids

There are several complementary approaches to modeling disordered solids. On the smallest scales, molecular dynamics and quasi-static simulations generate a wealth of information about particle interactions and emergent macroscopic behavior — including shear banding [39, 40, 41] — but they are limited to smaller numbers of particles and time scales. On the largest scales, phenomenological models such as viscoelasticity and the Dieterich-Ruina friction law (Eq. 1.1) describe stress-strain step and frequency responses, but to date these laws have not

been derived from microscopic dynamics.

A third approach focuses on the dynamics of collections of particles and their configurations. Examples of this approach include the Spot Model for granular materials [42], Soft Glassy Rheology (SGR) [43], and the theory of Shear Transformation Zones(STZs). The Spot Model generalizes dislocation dynamics in crystalline solids by postulating that a *spot*, a region of extra free volume shared among a collection of particles, executes a random walk through the material. Both SGR and STZ theories postulate that there are meso-scale *configurational soft spots* which are more susceptible than the surrounding material to yield under shear stress.

In this work we model sheared material interfaces using STZ theory. Spaepen first postulated that plastic flow could be modeled by tracking localized zones or regions of disorder [44]. Argon and Bulatov developed mean-field equations for these localized regions [45, 46]. Building on this work, Falk and Langer [47] introduced a mean-field theory which postulates that the zones, which correspond to particle configurations that are more susceptible to plastic rearrangements than the surrounding particles, could reversibly switch between two orientational states in response to stress. Additionally, these zones are created and annihilated as energy is dissipated in the system.

This theory captures many of the features seen in experiments, such as work hardening and yield stress [48, 49, 50]. The yield stress distinguishes an amorphous solid from a fluid. It is defined as the stress at which a material first stops deforming elastically and begins to respond plastically. (Fluids have zero yield stress.) Work hardening is the process of strengthening a material via a series of oscillating shear or compressive strains.

Early STZ formulations postulated that the STZs flip at a rate which is activated by the compactivity or free volume; regions with more free volume flip faster [51, 44]. While this idea is intuitively attractive, it requires an equation of motion for the free volume, which is difficult to determine from first principles.

A more recent idea is that an effective temperature governs the density of shear transformation zones [52]. In this case the structure of the packing is specified by the effective temperature, as opposed to the dynamics being activated by the free volume. The effective temperature approach is appealing because heat dissipation and energy balance can be used to determine the equation of motion for this internal state parameter.

Although we make no attempt to calculate the entropy from first principles, we postulate that because the material is being sheared slowly, configurational (as opposed to kinetic) degrees of freedom are the dominant contributions to the entropy. In steady state, the statistical distribution of configurations maximizes

this entropy and therefore the configurations are described by an effective temperature.

1.5 Dissertation Outline

The broad aim of this project is to characterize the underlying processes involved in deformation at the microscopic scale and incorporate the results into predictive tools applicable both to natural and man made systems.

Figure 1.5 uses an earthquake fault interface to illustrate the broad range of scales involved in these processes and summarizes our method for describing and modeling these multi-scale systems. Using data from experiments and simulations of amorphous materials (Fig. 1.5(c)), we develop a set of continuum STZ equations and material-specific parameters to describe deformation in theses solids. We determine a physically meaningful equation of motion for the effective temperature based on microscopic energy balance and study the behavior of the STZ model for a material driven between sliding interfaces. Using a combination of microscopic information (such as particle size) and fits to simulation and observational data, we determine the continuum model parameters. The resulting model can then be used to predict small-scale phenomena, such as strain localization (Fig. 1.5(b)), or be used in simulations of large scale phenomena like earthquake rupture simulations (Fig. 1.5(a)). A particularly exciting result is that transient feedback between the effective temperature and local strain rate leads to shear banding and dynamic weakening in fault gouge.

We first review the STZ model in its entirety in Chapter 2, and discuss various regimes where the STZ equations can be simplified. Chapter 3 focuses on homogeneous, steady state deformation in amorphous materials, where the total strain rate equals the plastic strain rate. We compare the STZ model to simulations of a glassy material by Haxton and Liu [53] and find that the simulation data tightly constrain the equation of motion for the effective temperature, as well as the rates at which STZs flip as a function of the stress and the steady state effective temperature $\hat{\chi}$.

In particular, we find that below the *thermal* glass transition temperature, the steady state strain rate as a function of the effective temperature exhibits Arrhenius and super-Arrhenius regimes, much like the viscosity as a function of the thermal temperature in glass-forming liquids. In addition, we develop an equation for the steady state value of χ above the thermal glass transition temperature that matches simulations.

An Arrhenius plot is a plot of the log of a time scale vs. the inverse of a

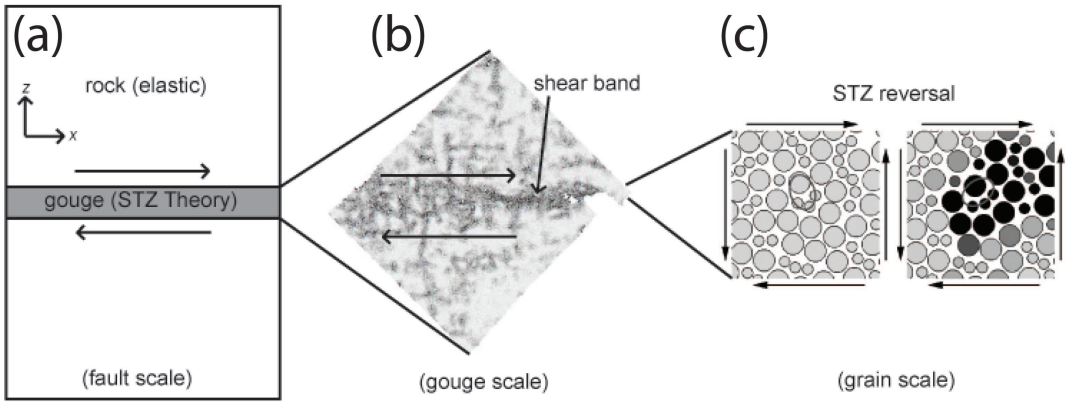

Figure 1.5: A schematic diagram which uses an earthquake fault interface to illustrate the broad range of scales in many types of amorphous systems. The smallest scale (c) involves plastic deformation at the particle scale. An intermediate scale (b) the sheared material exhibits interesting collective behavior, such as strain localization, while at the largest scales (a) the system couples to the outside driving system and defines the friction law on an interface.

temperature. Processes which involve a single step activated by the temperature should occur at a rate which is proportional to $\exp[E_A/(k_bT)]$, where E_A is the activation energy. These processes appear as a straight line on an Arrhenius plot. In contrast, super-Arrhenius processes are ones that require collective behavior at lower temperatures, so that the activation energy is no longer constant, and instead increases as the temperature decreases. These appear as a concave curve on an Arrhenius plot. Therefore, the fact that the steady-state plastic strain rate exhibits Arrhenius and super-Arrhenius regimes as a function of the effective temperature suggests that the effective temperature activates single and then collective plastic events as the effective temperature decreases.

While the effective temperature formalism described in Chapter 3 matches simulation data, a free volume STZ formalism has also been shown to capture important features of experimental data [51, 54]. These two models are conceptually different; in one case the effective temperature activates structures with higher potential energies, while in the other case the free volume affects the *dynamics* of STZ switching (and not the structure or density of STZs). Chapter 4 shows that although the models are conceptually different, they produce nearly the same set of partial differential equations. This indicates that an effective temperature formalism might be able to describe data previously explained by free-volume

models.

In contrast to the steady state dynamics described in Chapter 3, Chapter 5 focuses on transient dynamics in the low temperature, small strain rate regime. In this regime, simulations by Shi *et al.* have shown that amorphous systems develop shear bands [40]. We show that the STZ model generates shear bands and matches this simulation data. In addition, we find that an instability in the time-varying system trajectory is responsible for shear band formation; these bands will not occur in steady state. Additionally, shear bands will only form if the instability grows quickly compared to the underlying time-varying state, which allows us to develop a criterion for localization based on the average initial effective temperature of the system and amplitude of perturbations.

Having characterized shearing band formation in the low strain rate limit, Chapter 6 combines the results of Chapters 3 and 5 to study rate-dependent shear bands. We find that the type of shear localization and magnitude of dynamic weakening vary as a function of the initial system preparation (the initial effective temperature) and the applied strain rate. We also suggest that localization is a mechanism for the dynamic weakening seen at high strain rates on earthquake faults.

Finally, Chapter 7 discusses the significance of these results and highlights direction for future research.

Chapter 2

STZ model equations

Because amorphous solids exhibit rich behaviors spanning a wide range of length and time scales, we formulate and analyze the STZ model in several different regimes. In this chapter, we begin with a synopsis of the major assumptions and features of the STZ description. We then review the mean-field model that gives rise to the STZ partial differential equations, and describe material-dependent details such as the equation of motion for the effective temperature. Finally, we identify simplified equations that can be used in each of the regimes covered in later chapters.

2.1 Synopsis of the STZ model

As discussed in the introduction, the STZ formulation uses a model for the microscopic structural dynamics of an amorphous solid to generate continuum equations that relate the stress to the strain rate and other internal state variables. A critical postulate is that the effective temperature specifies probability distributions for the configurational degrees of freedom, and that STZs correspond to low-probability, high-energy configurational states. Therefore, in steady state the density of STZs is given by a Boltzmann distribution,

$$\hat{\Lambda} = \exp[-E_Z/k_B T_{eff}] \equiv \exp[-1/\chi], \tag{2.1}$$

where χ is the dimensionless effective temperature. In general, variables with a $\widehat{(\cdot)}$ represent steady state solutions.

Let q be the dimensionless plastic strain rate, $q = 2\overline{D^{pl}}\,\tau_0$, where D^{pl}_{ij} is the plastic rate of deformation tensor, τ_0 is an internal time scale such as the phonon frequency, and $\overline{D^{pl}} = \sqrt{(1/2)D^{pl}_{ij}D^{pl}_{ij}}$. Because the strain is accommodated by STZ

flips, the strain rate is proportional to the STZ density. Therefore the equation for q can often be simplified to the following form:

$$q \equiv 2\, e^{-1/\chi}\, f(s), \tag{2.2}$$

where $f(s)$ is a function of the stress s which we discuss below. The separation between the stress-dependent and χ-dependent parts of the plastic strain rate is a feature of STZ theory (as well as several free volume formulations) that has been emphasized recently by Shi, *et al.*[40].

Another critical assumption of STZ theory is that the elastic and plastic components of the rate of deformation tensor D_{ij} are independent and additive. In pure shear, the off-diagonal (xy)-component is given by:

$$D_{xy} = \frac{\mu^*}{2}\frac{ds_{xy}}{dt} + D^{pl}_{xy}. \tag{2.3}$$

The first term on the right-hand side is the elastic component of the deformation, which is proportional to the rate of change in the deviatoric stress (s_{xy}). The parameter μ^* is the ratio of the STZ stiffness to the elastic material stiffness.

Together, Eqs. 2.1, 2.2 and 2.3 form the framework of the STZ description. To complete the model, we must introduce an equation of motion for the effective temperature, define the function $f(s)$, and specify boundary conditions for the stress or the strain rate. These details are discussed below.

2.2 Plastic strain rate and energy dissipation

A mean field theory for shear transformation zones, first derived by Argon [45], has been developed in a series of papers [47, 48, 52, 50]. This section reviews the details of the STZ equations and emphasizes their similarity to other models for elastic and plastic flow.

When describing systems that undergo plastic and elastic deformation, it is convenient to break up the total stress tensor into hydrostatic and deviatoric components, $\sigma_{ij} = -p\delta_{ij} + s_y s_{ij}$, because hydrostatic stress generally does not cause yield. To simplify notation, the deviatoric stress has been nondimensionalized by an effective shear modulus s_y that specifies the stiffness of the STZs. The stress scale s_y also characterizes the stress at which the material begins to deform plastically. This yield stress is distinct from the maximum stress attained, s_m, and the steady state flow stress, s_f, both of which are sometimes also referred to as the yield stress in the literature.

In the slowly sheared materials we are modeling, the speed of sound in the material is very fast compared to the rate of plastic deformation. In this case the stress gradients equilibrate very quickly, and we take the zero density limit of the momentum conservation equations. This results in static elastic equations for the stress:

$$\frac{\partial \sigma_{ij}}{\partial x_j} = 0. \tag{2.4}$$

The rate of deformation tensor is the sum of elastic and plastic parts:

$$\begin{aligned} D_{ij}^{total} &= \frac{1}{2}\left(\frac{\partial v_i}{\partial x_j} + \frac{\partial v_j}{\partial x_i}\right) \\ &= \frac{\mathcal{D}}{\mathcal{D}t}\left(-\frac{p}{2K}\delta_{ij} + \frac{s_y}{2\mu}s_{ij}\right) + D_{ij}^{plast}, \end{aligned} \tag{2.5}$$

where $\mathcal{D}/\mathcal{D}t$ is the material or co-rotational derivative defined as:

$$\frac{\mathcal{D}A_{ij}}{\mathcal{D}t} = \frac{\partial A_{ij}}{\partial t} + v_k\frac{\partial A_{ij}}{\partial x_k} + A_{ik}\omega_{kj} - \omega_{ik}A_{kj}, \tag{2.6}$$

and $\omega_{ij} = 1/2(\partial v_i/\partial x_j - \partial v_j/\partial x_i)$. We also use the notation $\dot{A}_{ij} = \partial A_{ij}/\partial t$.

The plastic rate of deformation tensor can be written in terms of dynamical variables from STZ theory. We postulate that under shear stress, each STZ deforms to accommodate a certain amount of shear strain, and cannot deform further in the same direction. This is modeled by requiring that each STZ be in one of two states: oriented along the principle stress axis in the direction of applied shear, which we will denote "+", or in the perpendicular direction, "−".

Under applied strain, the STZ will *flip* in the direction of strain, from "−" to "+". Under shear stress in the opposite direction, the STZs can revert to their original configurations, which corresponds to a flip from "+" to "−". We assume that the STZ density is small and each STZ interacts with other STZs through continuum fields such as the stress. Therefore the rearrangements or *flips* occur at a rate $R(s)/\tau_0$, which depends on the stress and a characteristic attempt frequency τ_0. Figure 2.1 illustrates an STZ flipping event. The two panels are snapshots from a molecular dynamics simulation by M. Falk at two different times [47]. Dark particles have undergone non-affine or plastic displacements under shear; the four particles bounded by the oval exchange nearest neighbors during a plastic event. The oval is drawn to guide the eye – it shows a switch from a "−" orientation to a "+" orientation.

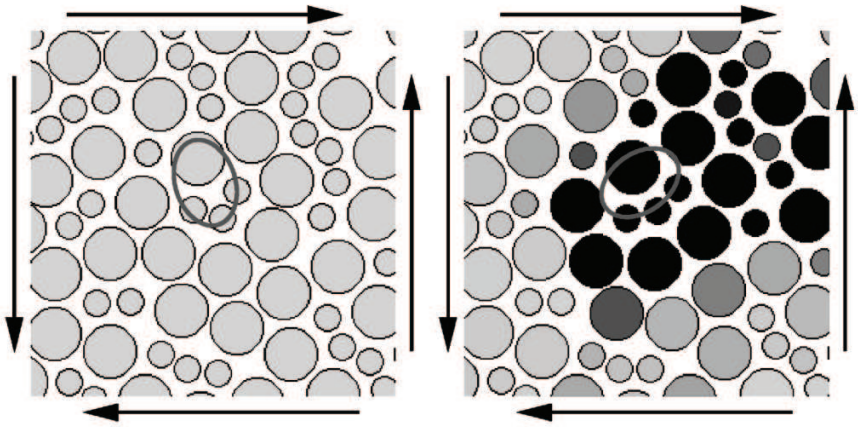

Figure 2.1: Snapshots from a molecular dynamics simulation by M. Falk, illustrating an STZ flipping event [47]. The shading indicates the magnitude of non-affine deformation that occurs between the two snapshots (darker = more deformation). The oval is drawn to guide the eye.

While this mean-field theory accurately models simulations at finite temperatures and strain rates, it may break down in the quasi-static (QS) limit. In that limit, Maloney and Lemaître [55] have shown that a localized elastic disturbance generated by a single STZ flip can lead to an avalanche of spatially correlated STZ rearrangements. These transient elastic cascades occur during an infinitesimal strain step, fluctuate spatially as the system is sheared, and are very different from the persistent localized shear bands generated by changes in the configurational disorder. An important question is whether these QS simulations, which use a conjugate gradient method to track the potential energy landscape, are relevant to real materials. Simulations by Argon and Demkowicz [56] show that molecular dynamics (MD) and QS methods generate significantly different results even though they ostensibly simulate the same material. One explanation is that the large-scale cascades found in QS simulations are cut off in real materials and MD simulations by processes that occur on inherent material timescales (such as the inverse phonon frequency). In other words, perhaps it is not possible to drive the system more slowly than any internal time scale.

Because each STZ can flip at most once in the direction of applied strain, STZs must be created and annihilated to sustain plastic flow. Based on these considerations, the number density of STZs in each direction, $n_\pm$ obeys the following

differential equation

$$\tau_0 \dot{n}_\pm = R(\pm s) n_\mp - R(\mp s) n_\pm + (\Gamma + \rho) \left(\frac{n_\infty}{2} e^{-1/\chi} - n_\pm \right), \tag{2.7}$$

where $R(\pm s)/\tau_0$ is the rate of switching per STZ as a function of stress, $\Gamma + \rho$ is the rate at which energy is dissipated per STZ, and $n_\infty e^{-1/\chi}$ is the steady state density of STZs in equilibrium.

The first two terms in Eq. (2.7) correspond to STZs switching from "+" to "−" states and vice-versa, while the last term enforces detailed balance: STZs are created at a rate proportional to $n_\infty e^{-1/\chi}$ and annihilated at a rate proportional to their density. The plastic rate of deformation tensor is given by the rate at which STZs flip:

$$D^{pl} = \frac{\epsilon_0}{n_\infty \tau_0} \left(R(s) n_- - R(-s) n_+ \right), \tag{2.8}$$

where ϵ_0 is a strain increment of order unity and n_∞ is a density roughly equal to the inverse of the volume per particle.

Pechenik [49] generalized Eqs. (2.7) and (2.8) to the case where the principal axes of the STZ orientation tensor n_{ij} are not aligned with principal axes of the stress tensor s_{ij}. These generalized equations can be written in terms of two new variables. The first is $\Lambda \equiv n_{tot}/n_\infty$, where n_{tot} is the tensorial generalization of $(n_+ + n_-)$, and corresponds to the total density of zones in a sample. The second is $m_{ij} \equiv n_{ij}/n_\infty$, where n_{ij} is the tensorial generalization of $(n_+ - n_-)$ and corresponds to the STZ orientational bias. Substituting these definitions into Eq. 2.7, we find that the STZ number density Λ is driven towards a Boltzmann distribution of the effective temperature as energy is dissipated in the system:

$$\dot{\Lambda} = (\Gamma + \rho) \left(e^{-1/\chi} - \Lambda \right). \tag{2.9}$$

The orientational bias of the STZs m_{ij} is incremented to accommodate plastic strain, and reset as energy is dissipated in the system:

$$\frac{\mathcal{D} m_{ij}}{\mathcal{D} t} = \frac{2}{\tau_0} \mathcal{C}(\overline{s}) \left(\frac{s_{ij}}{\overline{s}} \mathcal{T}(\overline{s}) - m_{ij} \right) - (\Gamma + \rho) m_{ij} \frac{e^{-1/\chi}}{\Lambda}. \tag{2.10}$$

The plastic strain rate can be written:

$$D^{pl}_{ij} = \frac{\epsilon_0}{\tau_0} \Lambda \mathcal{C}(\overline{s}) \left(\frac{s_{ij}}{\overline{s}} \mathcal{T}(\overline{s}) - m_{ij} \right). \tag{2.11}$$

The rate at which STZs are created/destroyed, denoted by $\Gamma + \rho$, is an important, positive quantity. The term ρ is a function of the thermal temperature θ and represents the thermal component of this rate, which is zero below the thermal glass transition temperature. The function Γ represents the mechanical component.

Falk and Langer [47] first proposed that Γ should be proportional to the rate of plastic work done on the system. Pechenik [49] refined this idea, noting that the rate of plastic work could be negative since energy could be stored in the plastic degrees of freedom. He proposed an alternative definition for Γ: the rate at which energy is dissipated per STZ, which is always positive. We adopt this important assumption in our STZ model.

Above the thermal glass transition temperature the functional form of Γ is necessarily complicated because thermally activated switching can release energy stored in the plastic degrees of freedom, [49, 52]. To solve for Γ, we first assert that the rate of plastic work is the sum of two terms: the rate of change in the recoverable energy (Ψ) stored in the plastic degrees of freedom, and Q, the rate of energy dissipation per unit volume

$$D^{pl}_{ij} s_{ij} = \frac{d\Psi}{dt} + Q. \tag{2.12}$$

Then following Pechenik,

$$Q = s_0 \frac{\epsilon_0}{\tau_0} \Lambda \Gamma, \tag{2.13}$$

where s_0 is an important stress scale that is discussed below. Combining Eq. 2.12 and 2.13, we derive the following equation for the dissipation rate per STZ, $\Gamma(s, \theta)$:

$$\Gamma(\overline{s}, \theta) = \frac{2\,\mathcal{C}(\overline{s})\Big[\mathcal{T}(\overline{s}) - m\Big]\Big[\overline{s}/s_0 - \xi(m)\Big] + m\,\xi(m)\,\rho(\theta)}{1 - m\,\xi(m)}, \tag{2.14}$$

where

$$\overline{s}^2 = 1/2\; s_{ij}\; s_{ij}, \tag{2.15}$$

$$\mathcal{C}(\overline{s}) = 1/2\left(R(\overline{s}) + R(-\overline{s})\right), \tag{2.16}$$

and

$$\mathcal{T}(\overline{s}) = \left(R(\overline{s}) - R(-\overline{s})\right) / \left(R(\overline{s}) + R(-\overline{s})\right). \tag{2.17}$$

The function $\xi(m)$ is the inverse of the function $\mathcal{T}(s)$, so that $\mathcal{T}[s_0\,\xi(m)] = m$ or

$$s_0\,\xi(m) = \mathcal{T}^{-1}(m). \tag{2.18}$$

For thermal temperatures below the glass transition ($\rho(\theta) = 0$), Eq. 2.14 can be simplified:

$$\Gamma(s) = \frac{2}{s_0 \epsilon_0}\, s\, f(s), \tag{2.19}$$

where the function $f(s)$, which also appears in Eq. 2.2, is defined as follows:

$$f(s) = \epsilon_0 \mathcal{C}(s)\Big[\mathcal{T}(s) - m(s)\Big]. \tag{2.20}$$

This confirms that the energy dissipated is equal to the work done on the system when configurational relaxation cannot occur via thermal fluctuations alone. Together, Eqs. (2.8), (2.14), and the tensorial generalization of Eq. (2.7) describe the evolution of the density of STZs and the orientational bias of STZs.

As emphasized by Langer [57], s_0 is a fundamental quantity that sets the scale of the yield stress and determines the fraction of the entropy in the configurational (as opposed to the kinetic) degrees of freedom. We first discuss how s_0 determines the scale of the yield stress. Note that for temperatures below the thermal glass transition temperature, when $\rho = 0$ and a yield stress exists, the equation of motion for the STZ bias has two steady states:

$$m_{ij}(\overline{s}) \to \begin{cases} s_{ij}\mathcal{T}(\overline{s})/\,\overline{s} & \text{for } \overline{s} < s_y \\ s_{ij}s_0/\,\overline{s}^2 & \text{for } \overline{s} > s_y, \end{cases} \tag{2.21}$$

where s_y is the stress at which the two stability branches intersect: $s_y\mathcal{T}(s_y) = s_0$. Below the yield stress the deformation is almost entirely elastic, while above the yield stress the system flows plastically as the STZs flip. In the athermal limit, $R(-s) = 0$, so that $\mathcal{T}(s) = 1$ and $s_y = s_0$. Note that above the thermal glass transition temperature the stress scale s_0 remains well-defined, although the system does not have a yield stress.

The term s_0 is also inversely proportional to the fraction of the energy dissipated in the configurational degrees of freedom [57]. Langer postulates that the product of the STZ density and the STZ creation rate is proportional to the rate at which configurational entropy is being produced by mechanical deformation:

$$\frac{\epsilon_0}{\tau_0}\Lambda\Gamma = \frac{\Omega}{k_B\nu_Z}\left(\frac{dS_c}{dt}\right)_{mech}, \tag{2.22}$$

where Ω is a volume per molecule and $k_B\nu_Z$ is the entropy per STZ. Let Q_c be the rate of energy dissipated into the configurational degrees of freedom per unit volume. Then $Q_c = T_{eff}\left(\frac{dS_c}{dt}\right)_{mech}$ is the fraction ϕ of the total energy dissipation rate per unit volume ($Q_c = \phi Q$) that affects the configurational degrees of freedom. Combining Eqs. 2.13 and 2.22 results in an expression for ϕ that is proportional

to $1/s_0$:

$$\begin{aligned} T_{eff}\frac{\epsilon_0 k_B \nu_Z}{\tau_0 \Omega}\Lambda\Gamma &= \phi s_0 \frac{\epsilon_0}{\tau_0}\Lambda\,\Gamma; \\ \phi &= \frac{k_B \nu_Z T_{eff}}{s_0 \Omega}. \end{aligned} \tag{2.23}$$

Next we discuss the details of the stress rate functions, $R(s)$, $C(s)$, and $f(s)$.

2.3 Rate switching function $R(s)$

There are two approaches to specifying $R(s)$, the rate at which STZs flip as a function of the stress. One approach is to define a minimal model, with as few parameters as possible, that satisfies the physical constraints. Based on physical considerations, $\mathcal{C}(s)$ is symmetric function of the stress that approaches zero as the stress approaches zero and approaches a line with a slope of unity as the stress becomes large. Bouchbinder *et al.* [50] describe a one-parameter family of functions with the correct properties. In the athermal, low temperature regime (Chapter 5) we use the simplest of these: $\mathcal{C}(s) = -2 + |s| + \exp(-|s|)(2 + |s|)$ and $\mathcal{T}(s) = 1$.

The extensive data set of Haxton and Liu [53] strongly constrains $R(s)$, and the simplified model discussed above is not sufficient to describe all the data. An alternative approach is to utilize our knowledge of the microscopic physics that gives rise to $R(s)$ to define a more realistic function. This also allows us to specify orders of magnitude for several parameters based on physical grounds rather than fits to data.

Determining an exact function $R(s)$ from first principles is an extremely difficult many-body problem. However, we do know how $R(s)$ behaves in the limits of very small and very large stresses, and we choose a function that smoothly interpolates between these two regimes. $R(s)$ exhibits Eyring-like behavior far below the yield stress, and power law behavior above the yield stress:

$$R(s) = \exp\left[-\frac{\theta_E}{\theta}\, e^{-s/\tilde{\mu}}\right]\left[1 + \left(\frac{s}{s_1}\right)^2\right]^{n/2}. \tag{2.24}$$

The first factor on the right-hand side of Eq.(2.24) is the Eyring rate in a form similar to that used in [47], where the exponential function of $s/\tilde{\mu}$ causes the rate to saturate at large s. Here, θ_E is the height of the Eyring activation barrier in units of T_Z. The energy θ_E should be less than one so that the barrier opposing

STZ transitions from one state is less than the barrier opposing creation of new STZs. The parameter $\tilde{\mu}$ is related to the curvature of this barrier at its peak. It appears here in the same place where $\bar{\mu}$ appeared in [52], but now it has no direct connection to the yield stress. In the limit of small stress, we recover an Eyring rate factor in the form

$$R(s) \approx \exp\left[-\frac{\theta_E}{\theta}\left(1 - s/\tilde{\mu}\right)\right]; \tag{2.25}$$

therefore

$$\mathcal{C}(s) \approx e^{-\theta_E/\theta} \cosh\left(\frac{\theta_E\, s}{\theta\, \tilde{\mu}}\right); \tag{2.26}$$

and

$$\mathcal{T}(s) \approx \tanh\left(\frac{\theta_E\, s}{\theta\, \tilde{\mu}}\right). \tag{2.27}$$

The second factor on the right-hand side of Eq.(2.24) converts the saturated Eyring function at large s to a power law:

$$\mathcal{C}(s) \approx \left(\frac{s}{s_1}\right)^n; \quad \mathcal{T}(s) \approx 1. \tag{2.28}$$

Here, s_1 is a temperature independent stress scale. The crossover stress s_1 determines when the system departs from Eyring stress-activated behavior.

The exponent n in Eq.(2.24) specifies the large stress power-law behavior. In the large stress limit where $\chi \to \infty$, (Eq. 2.2) requires that the plastic strain rate $\dot{\gamma}$ scale with $\mathcal{C}(s)$. For a fluid-like system with strong molecular interactions and dissipative forces the stress scales directly with the strain rate and we expect $n = 1$. For a hard-sphere system which is dominated by nearly elastic collisions, we instead expect Bagnold scaling [58]. Bagnold scaling occurs because hard spheres possess no natural energy scale. Then dimensional analysis suggests that the strain rate is proportional to the square root of the stress and $n = 1/2$. Analysis of simulation and experimental data suggest that the $n = 1$ is valid for bulk metallic glasses [57] while $n = 1/2$ is relevant for purely repulsive harmonic disks (See Chap. 3).

2.4 Effective temperature dynamics

To close the system of equations we require an equation of motion for the effective temperature. As mentioned earlier, the dimensionless effective temperature

χ is defined as the ratio of the dimensional effective temperature times the Boltzmann constant, $T_{eff}k_B$, to the energy scale for STZ density fluctuations, E_z. The steady state number density of STZs is $\exp[-E_z/(k_BT_{eff})] = \exp[-1/\chi]$. An approximate equation for energy balance is used to specify the effective temperature dynamics.

As detailed in [57], we assume that the heat content in the configurational degrees of freedom is driven by two independent sources, mechanical work and thermal fluctuations. As discussed in Section 2.2, the rate of heat per unit volume that enters the configurational degrees of freedom is $Q_c = T_{eff}\left(dS_c/dt\right)_{mech}$. Ono *et al.* [38] show that at low strain rates the system is driven towards a specific steady state of disorder $\hat{\chi}$. Therefore we assume that the mechanical heat drives the effective temperature towards $\hat{\chi}$ according to the conventional linear law of heating. In addition, we postulate that the heat produced by thermal fluctuations, $Q_T = T_{eff}\left(dS_c/dt\right)_{therm}$, drives the effective temperature towards the thermal equilibrium bath temperature θ according to the linear law of cooling. The resulting equation of motion for χ is:

$$\begin{aligned} C_{eff}T_z\dot{\chi} &= T_{eff}\left(\frac{dS_c}{dt}\right)_{mech}\left[1-\frac{\chi}{\hat{\chi}}\right] \\ &\quad + T_{eff}\left(\frac{dS_c}{dt}\right)_{therm}\left[1-\frac{\chi}{\theta}\right] + D\frac{\partial^2\chi}{\partial y^2}, \end{aligned} \tag{2.29}$$

where C_{eff} is a specific heat, $T_z = E_z/k_B$ is the STZ formation energy in temperature units, and the last term represents diffusion of effective temperature.

Because χ is driven towards $\hat{\chi}$ through configurational rearrangements, we assume that a gradient in the effective temperature as a function of position leads to a corresponding flux. This flux, which is proportional to the strain rate, implies a diffusion term in the equation for χ. Diffusion of potential energy (which corresponds to diffusion of effective temperature) is seen in simulations by Shi *et al*, as we will discuss in detail in Chapter 5.

The paramter D can be represented as the ratio of a length scale squared to a time scale: a^2/τ_D. In STZ theory there are two candidates for the attempt frequency $1/\tau_D$: the inherent material attempt frequency $1/\tau_0$ and the local plastic strain rate $\dot{\gamma}_{pl}$. The first possibility implies that the diffusivity is a constant material property, while the second indicates that the local potential energy diffuses at a rate proportional to the rate of local particle rearrangements. Because the effective temperature is the derivative of the configurational degrees of freedom with respect to the energy, only configurational rearrangements, i.e. plastic events, permit diffusion of the effective temperature. This suggests that the diffusivity

should vary with strain rate, so that $D = a^2\dot{\gamma}_{pl}$, where a is a length scale that corresponds to the radius of an STZ.

Now we are in a position to discuss the thermal and mechanical entropy contributions to the effective temperature. The mechanical rate of change in the entropy per unit volume, $(dS_c/dt)_{mech}$ is given by Eq. 2.22. In analogy to Eq. 2.22, the thermal rate $(dS_c/dt)_{therm}$ is proportional to the product of a thermal noise term $\rho(\theta)$ and an effective temperature activation term $\exp[-\beta/\chi]$ [57]. The parameter β is a free energy describing all states that are able to relax via thermal fluctuations. Since there are more of these "thermally relaxable" states than STZs (which are more specific stress-susceptible states), we expect $\beta < 1$. The thermal noise term, $\rho(\theta)$, is zero below the thermal glass transition temperature and specifies the Newtonian viscosity in the limit of zero stress at higher temperatures. Because the viscosity exhibits super-Arrhenius behavior near the glass transition, Langer [52, 57] has proposed that ρ has the following form:

$$\rho(T) = \begin{cases} e^{-\alpha(T)} & \text{for } T > T_0 \\ 0 & \text{otherwise} \end{cases} \tag{2.30}$$

where α is given by:

$$\alpha(T) = \frac{T_1}{T - T_0} \exp[-a(T - T_0)/(T_A - T_0)], \tag{2.31}$$

and T_0 is the thermal glass transition temperature, T_A is the temperature at which the system begins to exhibit Arrhenius behavior, and T_1 is a fit parameter. The details are discussed in Chapter 3.

In addition, Haxton and Liu's [53] recent simulations suggest that the steady-state effective temperature is governed by a similar equation:

$$\frac{1}{q(\hat{\chi})} = \frac{1}{q_0} \exp\left[\frac{A}{\hat{\chi}} + \alpha_{eff}(\hat{\chi})\right], \tag{2.32}$$

also detailed in Chapter 3.

Putting everything together, we arrive at an equation of motion for the effective temperature:

$$\begin{aligned} \tau_0 c_0 \dot{\chi} &= e^{-1/\chi}\Gamma(\overline{s})\chi\left[1 - \frac{\chi}{\hat{\chi}}\right] \\ &\quad + \kappa e^{-\beta/\chi}\rho(T)\chi\left[1 - \frac{\chi}{\theta}\right] + a^2\dot{\gamma}_{pl}\frac{\partial^2\chi}{\partial y^2}. \end{aligned} \tag{2.33}$$

In steady state, which is discussed in Chapter 3, the left hand side of Eq. 2.33 is zero and the system deforms homogeneous, so there is no diffusion. This results in the following equation for χ:

$$e^{-1/\chi}\,\Gamma(s,\theta)\,\left[1-\frac{\chi}{\hat{\chi}(q)}\right]=K(\chi)\,\rho(\theta)\,\left(\frac{\chi}{\theta}-1\right). \tag{2.34}$$

In an athermal STZ formulation there is no mechanism for relaxation of the effective temperature to the thermal temperature T, so that the effective temperature everywhere tends towards $\hat{\chi}$. In addition, at low strain rates Ono *et al.* show that $\hat{\chi}$ approaches a constant steady state value, χ_0 [38]. Then the equation of motion for χ is much simplified:

$$\begin{aligned} C_{eff}\dot{\chi} &= Q_c\left(1-\frac{\chi}{\hat{\chi}}\right)+D\frac{\partial^2\chi}{\partial y^2}; \\ C_{eff}\dot{\chi} &= \frac{Q_c}{\chi_0}\,(\chi_0-\chi)+D\frac{\partial^2\chi}{\partial y^2}. \end{aligned} \tag{2.35}$$

In Chapter 5 we use a slightly modified version of Eq. 2.35, where the right-hand side is multiplied by a factor χ_0/χ. This corresponds to adding a term χ to the right hand side of the entropy defined by Eq. 2.22. Since χ remains close to χ_0, the two equations are similar and we can not distinguish between them in our numerical simulations.

Chapter 3

Steady-state effective temperature dynamics

This chapter represents work performed by James S. Langer and M. Lisa Manning, originally published in Physical Review E in 2007 [59]. Although these studies were completed after the work described in Chapter 5, they utilize a more general version of the STZ theory and therefore this work is presented first. In addition, some of the information contained in the background section is also contained in Chapter 2; we reprint it here so that this chapter remains a self-contained unit.

In this chapter, Langer and I use STZ theory to fit steady state simulation data by T. Haxton and A. Liu (HL) [53]. The large data set, which spans a wide range of temperatures and strain rates, indicates that the steady state effective temperature is rate dependent. We show that in steady state the strain rate can be viewed as a process that is activated by the effective temperature, much like viscosity is determined by a process that is activated by the thermal temperature. We also identify an effective temperature glass transition temperature and discuss its relation to the thermal glass transition temperature. The STZ model is strongly constrained by the HL data, and the rate-dependence seen in these simulations has interesting implications for failure and friction, as we discuss further in Chapter 6.

3.1 Background: Basic Hypotheses

In a remarkable recent report, T. Haxton and A. Liu (HL) [53] have described molecular-dynamics simulations of a simple, sheared, two-dimensional, glass-forming material over three decades of steady-state strain rates $\dot{\gamma}$, and for

bath temperatures T ranging from about one tenth of the glass transition temperature T_0 to about twice T_0. Most importantly, by measuring pressure fluctuations, HL have determined values of the effective disorder temperature $T_{\rm eff}$ for each value of $\dot\gamma$, T, and the shear stress s. This extensive data set tests the applicability of any theory of amorphous plasticity such as the shear-transformation-zone (STZ) theory discussed here, and also probes the limits of validity of the effective-temperature concept. [38, 37, 60, 61, 62, 63, 64, 65] We find that the main features of the STZ theory presented in earlier papers [47, 52, 66, 50] nicely survive these tests. Moreover, several of the theory's specific ingredients, which had not been tightly constrained by earlier experiments or simulations, can be refined and extended in light of the HL data. Our most surprising conclusion is that, for $T < T_0$, the relation between $\dot\gamma$ and $T_{\rm eff}$ is a direct analog of the relation between the α relaxation rate and the bath temperature T near a conventional glass transition.

It is well known (e.g. see [31]) that, for unstressed glass forming materials in a range of temperatures above some T_A, the viscosity η is – at least to a first approximation – a simple activated process with a temperature independent energy barrier. Below T_A, η depends super-Arrheniusly on T, diverging as T decreases toward the glass transition temperature (or Kauzmann temperature) T_0. Figure 3.1(a) shows that the HL data for the viscosity in the limit of vanishing strain rate can be fit by a function of the form

$$\eta = \eta_0(\theta) \exp\left[\frac{1}{\theta} + \alpha(\theta)\right], \tag{3.1}$$

where $\theta = T/T_Z$ and $k_B T_Z$ is an Arrhenius activation energy that we interpret as the energy of formation for an STZ. $\alpha(\theta)$ is a model-dependent function, to be specified later, that diverges as $\theta \to \theta_0 = T_0/T_Z$ and vanishes for $\theta > \theta_A = T_A/T_Z$. The prefactor $\eta_0(\theta)$ is a relatively slowly varying function of θ that appears prominently in our data analysis in Section 3.3.

Our key hypothesis is that, below the glass transition temperature θ_0, there is a relationship analogous to Eq.(3.1) between the steady-state effective temperature and the strain rate $\dot\gamma$. In analogy to the definition of θ, and consistent with earlier notation [52, 66, 50], we write $\chi \equiv T_{\rm eff}/T_Z$. We also define $q \equiv \tau_0\,\dot\gamma$, where τ_0 is the fundamental time scale that appears in the dynamical STZ equations of motion. Thus, q is a dimensionless rate of molecular rearrangements or, equivalently, a stirring rate. The HL results are expressed in terms of a molecular time scale, t_0, which is derived from their molecular interactions and is not necessarily the same as τ_0 – although the two times should have about the same order of magnitude. We find it convenient to set $\tau_0 = t_0 = 1$, and to incorporate any difference between

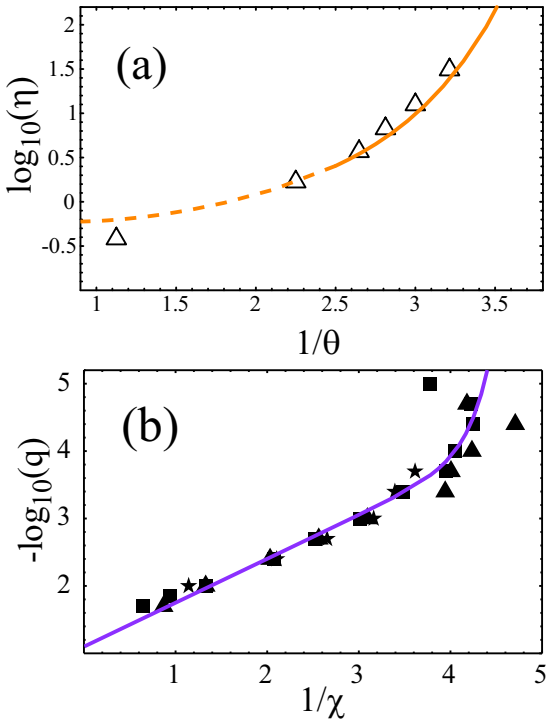

Figure 3.1: (a) Logarithm of the HL viscosity (open triangles) as a function of the inverse temperature $1/\theta = T_Z/T$. The solid line is the STZ-theory fit to these data points. The dashed extension of this line indicates a region where the temperatures are so high that the theory becomes incorrect. (b) Logarithm of the HL strain rate as a function of the inverse effective temperature $1/\chi$ at temperatures below the glass transition temperature $\theta_0 = 0.20$. The data points correspond to temperatures $\theta = 0.022$ (stars),0.044 (squares) and 0.11 (triangles). The solid line is the theoretical fit. See Section 3.3 for details of the theoretical analysis and an evaluation of T_Z.

these time scales into the parameter ϵ_0 defined below in Eq. (3.7). For clarity, however, we occasionally retain explicit factors τ_0.

We propose that the rate q be interpreted as a purely kinetic quantity, independent of the specific mechanism by which the rearrangements occur. We then define $\hat{\chi}(q)$ to be the dimensionless, steady-state, effective temperature at stirring rate q. To a first approximation, we assume that $\hat{\chi}(q)$ is independent of θ for $\theta \leq \theta_0$. As we shall see later, the temperature dependence of $\hat{\chi}(q)$ becomes more interesting for larger θ.

In the limit $q \ll 1$, the number of rearrangements depends only on the extent

of the deformation and not its duration; thus the condition for steady-state equilibrium is that, with high probability, each molecule has changed its neighbors at least a few times. It follows that $\hat{\chi}(q \to 0) = \chi_0$ is a nonzero constant, also independent of the rearrangement mechanism. We then postulate that the inverse function $q(\hat{\chi})$ is the rate at which rearrangements occur when the system is driven so that its steady-state effective temperature is $\hat{\chi}$. Then, in analogy with Eq.(3.1), we write

$$\frac{1}{q(\hat{\chi})} = \frac{1}{q_0} \exp\left[\frac{A}{\hat{\chi}} + \alpha_{\text{eff}}(\hat{\chi})\right], \tag{3.2}$$

where q_0 and A are constants to be determined, and $\alpha_{\text{eff}}(\hat{\chi})$ is a super-Arrhenius function that diverges at the effective Kauzmann temperature χ_0 and vanishes above some χ_A.

This hypothesis is supported by the HL data. Fig. 3.1(b) is an Arrhenius plot of the HL results for the strain rate versus the effective temperature for three values of θ, all almost certainly below θ_0, and the solid curve is a fit to those points using Eq. (3.2). There are large uncertainties in the data at small strain rates (large $1/\chi$), but the existence of Arrhenius and super-Arrhenius regions is apparent. Note that the Arrhenius region, i.e. the section of the curve that is linear in $1/\chi$, seems to extend all the way to infinite χ. Ordinarily we do not think of Arrhenius formulas remaining valid out to high temperatures. The difference here may be that the effective temperature pertains only to a fraction of the degrees of freedom in this system; so, perhaps in analogy to magnetic spin temperatures, the maximally disordered state at infinite χ is realistic.

One of the most interesting features of Eq.(3.2) is that χ diverges at a finite strain rate, $q_0 \cong 0.08$ as seen from the extrapolation shown in Fig. 3.1(b). For molecular systems where τ_0 is of order femtoseconds, $\dot{\gamma} = 0.08/\tau_0$ is an impossibly large rate; but it is accessible in numerical simulations and perhaps also in granular or colloidal systems. The system must liquefy in some sense when driven faster than q_0; and the STZ theory must break down near that point.

3.2 STZ Theory

3.2.1 General STZ Equations

In order to use Eq.(3.2) to compute stresses, strain rates and effective temperatures for θ both below and above θ_0, we need a complete set of dynamical equations of the kind provided by the STZ theory. In this Section, we summarize the version of that theory that was presented in [52], specializing to steady-state

motion but otherwise retaining the generality needed to describe plasticity over the wide range of driving conditions studied by HL. We need one structural modification of this theory, which we explain following Eq.(3.10) below; and our analysis requires model dependent rate factors that differ from those used in earlier papers. We start by writing the STZ equations in a form determined by the basic structure of the theory. Then, in the following subsection, we specify our choice of the model dependent ingredients of these equations.

In keeping with the emphasis of HL and the results of recent STZ analyses such as [66, 50], we write this theory in a form in which the effective temperature χ is the single, dynamically relevant, internal state variable. Accordingly, we need just one equation for the dimensionless strain rate q as a function of the shear stress s and the effective temperature χ, supplemented by the steady-state version of an equation of motion for χ.

The equation for the strain rate has the form

$$q \equiv \dot{\gamma}\,\tau_0 = 2\,e^{-1/\chi}\,f(s,\theta), \tag{3.3}$$

where $f(s,\theta)$ is a model-dependent function (to be specified shortly), and $\exp(-1/\chi)$ is proportional to the STZ density. This clean separation between the stress-dependent and χ-dependent parts of the plastic strain rate is an important characteristic feature of the STZ theory that has been emphasized recently by Shi *et al.*[40].

The equation for χ is

$$e^{-1/\chi}\,\Gamma(s,\theta)\,\left[1-\frac{\chi}{\hat{\chi}(q)}\right] = K(\chi)\,\rho(\theta)\,\left(\frac{\chi}{\theta}-1\right). \tag{3.4}$$

This is essentially the steady-state version of Eq.(3.5) in [52]; but here we have written it in a form that is more appropriate for situations in which $\hat{\chi}(q)$ can become large.

According to Eq.(3.4), χ finds its steady-state value when the rate at which it is being driven mechanically toward its kinetically optimal value $\hat{\chi}(q)$, on the left-hand side, is balanced by the rate at which χ relaxes toward the bath temperature on the right. $\Gamma(s,\theta)$, another model-dependent function, is proportional to the rate at which the work done by the driving force is dissipated as configurational entropy; thus $\Gamma(s,\theta)$ vanishes at $s=0$. The function

$$\rho(\theta) \equiv \begin{cases} \exp\left[-\alpha(\theta)\right] & \text{for } \theta > \theta_0 \\ 0 & \text{for } \theta < \theta_0 \end{cases} \tag{3.5}$$

is the super-Arrhenius part of the α relaxation rate. Because $\rho(\theta)$ vanishes for $\theta < \theta_0$, Eq.(3.4) implies that the low-temperature, steady-state value of χ is $\hat{\chi}(q)$ as anticipated in Eq.(3.2). The function $K(\chi)$ appearing in Eq.(3.4) is proportional to the density of sites at which thermal equilibration events – as opposed to shear-transformations – take place. We assume here, as in [52], that

$$K(\chi) = \kappa\, e^{-\beta/\chi}, \tag{3.6}$$

with $\beta = 1$, which means that both kinds of sites are comparably populated. The parameter κ remains to be determined from the data.

In the general STZ equations as developed in [52, 50], the function $f(s,\theta)$ in Eq.(3.3) has the form

$$f(s,\theta) = \epsilon_0\, \mathcal{C}(s) \Big[\mathcal{T}(s) - m(s)\Big], \tag{3.7}$$

where ϵ_0 is a dimensionless constant,

$$\mathcal{C}(s) = \frac{1}{2}\Big[R(s) + R(-s)\Big], \tag{3.8}$$

$$\mathcal{T}(s) = \frac{R(s) - R(-s)}{R(s) + R(-s)}, \tag{3.9}$$

and $R(s)/\tau_0$ is the rate at which individual STZ's undergo forward shear transitions driven by the stress s.

The function $m(s)$ is the orientational variable that emerges in the role of a back stress in the STZ theory. It satisfies the steady-state relation:

$$2\,\mathcal{C}(s) \Big[\mathcal{T}(s) - m(s)\Big]\Big[1 - m(s)\, s/s_0\Big] = m(s)\, \rho(\theta). \tag{3.10}$$

Here, and in the equation for $\Gamma(s,\theta)$ that follows, we depart slightly from the equations derived in [52]. In that paper, the yield stress s_y was assumed to be approximately equal to a temperature-independent constant $\bar{\mu}$, and the stress was everywhere written in units of that constant. Here, on the other hand, it is obvious – most visibly in the HL graphs of stress versus strain rate at low-temperatures – that s_y must be a function of θ. Examination of the derivation of the STZ equations in [52] indicates that the factor of proportionality between $\Gamma(s,\theta)$ and the energy dissipation rate per STZ, which was set equal to $\bar{\mu}$ there primarily for dimensional reasons, should have been a possibly temperature-dependent stress that we now call s_0. The result of this change is that a factor s, which multiplies the strain rate in the expression for the rate at which plastic work is done on

the system, is replaced by s/s_0, and the explicit s that appears in Eq.(3.10) now becomes s/s_0. This change in the analysis removes an ambiguity in the older STZ theories; e.g. see [49]. Details will be published elsewhere [57].

The significance of the quantity s_0 is that below the glass transition temperature it is closely related to the dynamical yield stress s_y. For $\theta < \theta_0$ and $\rho(\theta) = 0$, s_y is the value of s for which the two factors on the left-hand side of Eq.(3.10) vanish simultaneously; therefore it is the solution of the equation

$$s_y \, \mathcal{T}(s_y) = s_0. \tag{3.11}$$

Because $\mathcal{T}(s) \leq 1$ in all cases and is approximately equal to unity at low temperatures, $s_y \cong s_0$. If s_0 is a function of θ in Eq.(3.11), then s_y also is temperature dependent. Although there is no yield stress for $\theta > \theta_0$, $f(s, \theta)$ still changes abruptly at $s \cong s_0$ for θ not too much larger than θ_0. This implies that at stresses close to s_0, the stress vs. strain rate curve exhibits an abrupt change in slope.

The STZ formula for the dissipation rate $\Gamma(s, \theta)$ appearing in Eq. (3.4) is

$$\Gamma(s, \theta) = \frac{2\,\mathcal{C}(s)\Big[\mathcal{T}(s) - m\Big]\Big[s/s_0 - \xi(m)\Big] + m\,\xi(m)\,\rho(\theta)}{1 - m\,\xi(m)}, \tag{3.12}$$

where $m = m(s)$ as given by Eq.(3.10), and

$$s_0\,\xi(m) = \mathcal{T}^{-1}(m) \tag{3.13}$$

is the inverse of the function $\mathcal{T}(s)$; that is, $\mathcal{T}[s_0\,\xi(m)] = m$. It is not difficult to show that $\epsilon_0\,\Gamma(s, \theta) = 2\,s\,f(s, \theta)$ for $\theta < \theta_0$, confirming that the energy dissipated is equal to the work done on the system when configurational relaxation cannot occur via thermal fluctuations alone. Above the glass transition, on the other hand, the external work is not the same as the dissipation, and the use of Eq.(3.12) is necessary for accurate calculations.

3.2.2 Model-Dependent Ingredients

As discussed in Chapter 2, we choose a more realistic model for the STZ forward transition rate $R(s)$. We depart from the choices made in earlier papers [52, 50], where we were concerned with experiments and simulations performed only at relatively small driving forces, and which therefore did not sharply constrain our choice of $R(s)$. HL have provided a data set that goes up to stresses more than ten times the yield stress, at temperatures both well above and well

below the glass transition, and thus have made it necessary for us to consider this rate factor in a broader context than before.

We need a function $R(s)$ that interpolates between Eyring-like behavior at very small stresses and power-law growth at very large ones. In choosing such an $R(s)$, we find that we must depart from our earlier, purely phenomenological procedure of choosing simple functions with very few adjustable parameters, in the expectation that whatever data we had available would not justify additional theoretical complications. Here we are facing a very different situation. In order to interpret the HL data, we find it better to start with a physically motivated model containing an uncomfortably large number of parameters. Determining the values of these parameters is made easier in places by the fact that we can fit some parts of the data independently of other parts, and then see how these initially separate pieces of the puzzle fit together, for example, in connecting our predictions of behaviors at very small strain rates to those at very large ones. Another advantage of this more nearly first-principles procedure is that we can guess the magnitudes of many parameters on physical grounds, and also know the limits of validity of physics-based approximations. For example, we know that the Eyring-like formula that we use for the STZ transition rate breaks down at the highest temperatures simulated by HL; and thus we know to assign less weight to our theory at those temperatures in fitting the HL viscosity curve.

Our proposed $R(s)$ is

$$R(s) = \exp\left[-\frac{\theta_E}{\theta}\, e^{-s/\tilde{\mu}}\right]\left[1 + \left(\frac{s}{s_1}\right)^2\right]^{n/2} . \tag{3.14}$$

The first factor on the right-hand side of Eq.(3.14) is the Eyring rate in a form similar to that used in [47], where the exponential function of $s/\tilde{\mu}$ causes the rate to saturate at large s. Here, θ_E is the height of the Eyring activation barrier in units of T_Z. We expect $\theta_E < 1$, because the barrier opposing STZ transitions from one state to the other should be less than the barrier opposing creation of new STZ's. The parameter $\tilde{\mu}$ is related to the curvature of this barrier at its peak. It appears here ostensibly in the same place where $\bar{\mu}$ appeared in [52], but now it has no direct connection to the yield stress. In the limit of small stress, we recover an Eyring rate factor in the form

$$R(s) \approx \exp\left[-\frac{\theta_E}{\theta}\,(1 - s/\tilde{\mu})\right]; \tag{3.15}$$

therefore

$$\mathcal{C}(s) \approx e^{-\theta_E/\theta} \cosh\left(\frac{\theta_E\, s}{\theta\, \tilde{\mu}}\right); \tag{3.16}$$

and

$$\mathcal{T}(s) \approx \tanh\left(\frac{\theta_E\, s}{\theta\, \tilde{\mu}}\right). \tag{3.17}$$

The second factor on the right-hand side of Eq.(3.14) converts the saturated Eyring function at large s to a power law:

$$\mathcal{C}(s) \approx \left(\frac{s}{s_1}\right)^n; \quad \mathcal{T}(s) \approx 1. \tag{3.18}$$

Here, s_1 is a temperature independent stress scale. Without loss of generality, we normalize the nominal yield stress $s_0(\theta)$ so that $s_0(0) = 1$ and measure stresses s in units of this zero-temperature yield stress. The crossover stress s_1 determines when the system departs from Eyring stress-activated behavior.

The exponent n in Eq.(3.14) is especially interesting. In strongly dissipative systems, we expect $n = 1$, indicating that the STZ transition rate is controlled at large stresses by some linear dissipative mechanism such as friction or viscosity. In the opposite limit, where rates are controlled by collisions between primarily hard-core objects and the detailed molecular interactions are relatively unimportant, we expect to find Bagnold scaling[58]. That is, if there is no natural energy or stress scale in the problem, then dimensional analysis requires that the stress be proportional to the square of a rate. Since $R(s)/\tau_0$ is the only available quantity with dimensions of inverse time, we must have $R(s) \sim s^{1/2}$ and $n = 1/2$. It appears that the latter case is more consistent with the HL viscosity data.

Other model-dependent ingredients that we must specify are the super-Arrhenius function $\alpha(\theta)$ and its analog $\alpha_{\rm eff}(\hat{\chi})$. Here we adopt formulas motivated by the excitation-chain theory of the glass transition [67, 68] proposed recently by Langer. For present purposes, these formulas need not be interpreted as anything more than phenomenological fits to experimental data. We write

$$\alpha(\theta) = \left(\frac{\theta_1}{\theta - \theta_0}\right)^p \exp\left[-b\,\frac{\theta - \theta_0}{\theta_A - \theta_0}\right], \tag{3.19}$$

where $b \cong 3$ produces a reasonably accurate description of the transition from an inverse power-law divergence near θ_0 to simple Arrhenius behavior above θ_A in analyses of experimental data.[57] The excitation-chain theory predicts $p = 1$ (Vogel-Fulcher) in three dimensions and $p = 2$ in two, but the HL data is not accurate enough to distinguish between these possibilities. Since HL fit their two dimensional viscosity data with a Vogel-Fulcher function, we have chosen to be conservative and use $p = 1$ in our analyses. However, we point out in Section 3.3 that $p = 2$ remains an interesting possibility.

The effective-temperature analog of Eq.(3.19) is

$$\alpha_{\rm eff}(\hat{\chi}) = \left(\frac{\chi_1}{\hat{\chi}-\chi_0}\right)^p \exp\left[-b\,\frac{\hat{\chi}-\chi_0}{\chi_A-\chi_0}\right]. \tag{3.20}$$

3.3 Comparisons between STZ theory and the HL simulations

3.3.1 Evaluating the Parameters

We turn now to a detailed numerical comparison between these theoretical predictions and the HL data. We start by deducing values of the parameters T_Z and A in Eq.(3.2) and the exponent n in Eqs.(3.14) and (3.18), using primarily the data in the extreme Arrhenius region at low temperatures θ and large values of χ.

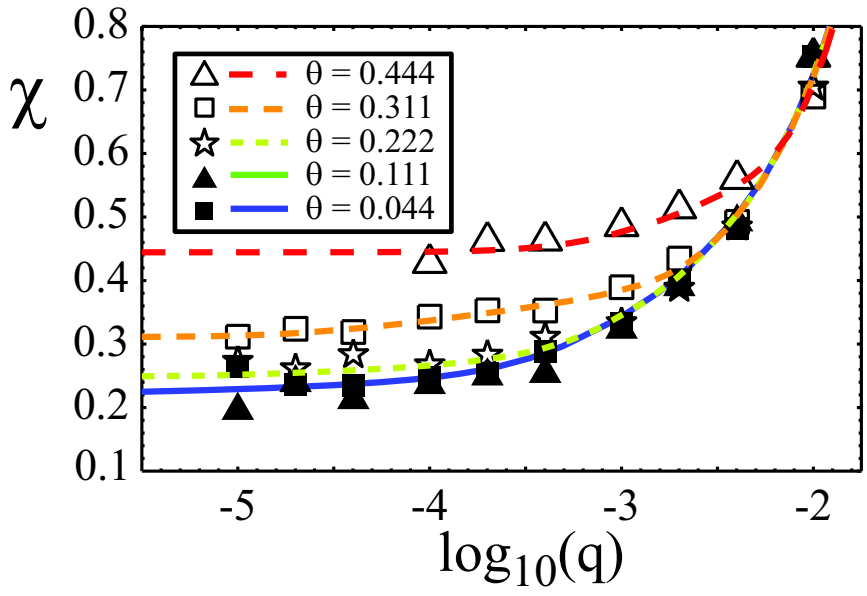

Figure 3.2: Effective temperature χ as a function of $\log_{10}(q)$ for HL results both above (open symbols) and below (solid symbols) the glass transition. The smooth curves are the predictions of the STZ theory at the same temperatures θ.

Figure 3.1(b) shows the HL data for $-\log_{10}(q)$ as a function of $1/\chi$, for the three lowest HL temperatures, $\theta = 0.022$, 0.044, and 0.11, all of which are comfortably below the glass transition temperature $\theta_0 \cong 0.20$. Therefore, $\rho(\theta) = 0$

and $\chi = \hat{\chi}$. From Eq.(3.2) and the observed slope of this graph in the Arrhenius region, i.e. from the data shown in HL Fig. 1b, we find that $A\,T_Z \cong .0068$ (in HL units).

A second piece of information is obtained by looking at the HL results for stress as a function of $1/\chi$, shown here in Fig. 3.5. Again, we look only in the large-χ, small θ limit. Equations (3.2) and (3.3), plus our large-s estimate for the rate factor, combine to give

$$q \approx q_0\, e^{-A/\chi} \approx 2\,\epsilon_0\, e^{-1/\chi} \left(\frac{s}{s_1}\right)^n \tag{3.21}$$

from which we find

$$\ln(s/s_1) \approx \frac{1}{n}\,\ln\left(\frac{q_0}{2\,\epsilon_0}\right) - \frac{A-1}{n\,\chi}. \tag{3.22}$$

The observed slope in Fig. 3.5, i.e. in the original HL figure in which $\ln(s)$ is plotted as a function of $1/T_{\rm eff}$, tells us that $(A-1)\,T_Z/n \cong .004$.

A third relation, equivalent to the first two but useful for data analysis, is

$$\ln(s/s_1) \approx \frac{1}{n}\,\ln\left(\frac{q_0^{1/A}}{\epsilon_0}\right) + \frac{1}{n}\left(\frac{A-1}{A}\right)\ln(q). \tag{3.23}$$

The observed asymptotic slope of the graph of $\ln(s)$ versus $\ln(q)$ shown in Fig. 3.6 is $(A-1)/n\,A \cong 2/3$. If we assumed $n = 1$, we would find $A \cong 3$ and $T_Z \cong 0.00225$, a value of T_Z that is too small to be consistent with the HL viscosity data. However, $n = 1/2$ (the Bagnold prediction) implies that $A \cong 1.5$ and $T_Z \cong 0.0045$, which fits the viscosity quite well.

We then use the last two graphs to evaluate the q-independent terms on the right-hand sides of Eqs.(3.22) and (3.23), with $q_0 \cong .08$. In this way we check for consistency of the estimates we have obtained from a noisy data set, and find a relation between s_1 and ϵ_0:

$$s_1 \cong 2.3 \times 10^3\ \epsilon_0^2. \tag{3.24}$$

Several other parameters can be determined by direct examination of the HL data. HL measure their stresses σ in units related to their interatomic forces. Because our values of s are expressed in units of the zero-temperature yield stress, the ratio of σ to s is approximately the value of σ at the lowest strain rate and the lowest temperature shown in HL Fig.1a, i.e. approximately 0.001 in HL stress units. Thus, the stress-conversion relation is

$$\sigma \cong \sigma_{HL}\, s; \qquad \sigma_{HL} \cong 0.001. \tag{3.25}$$

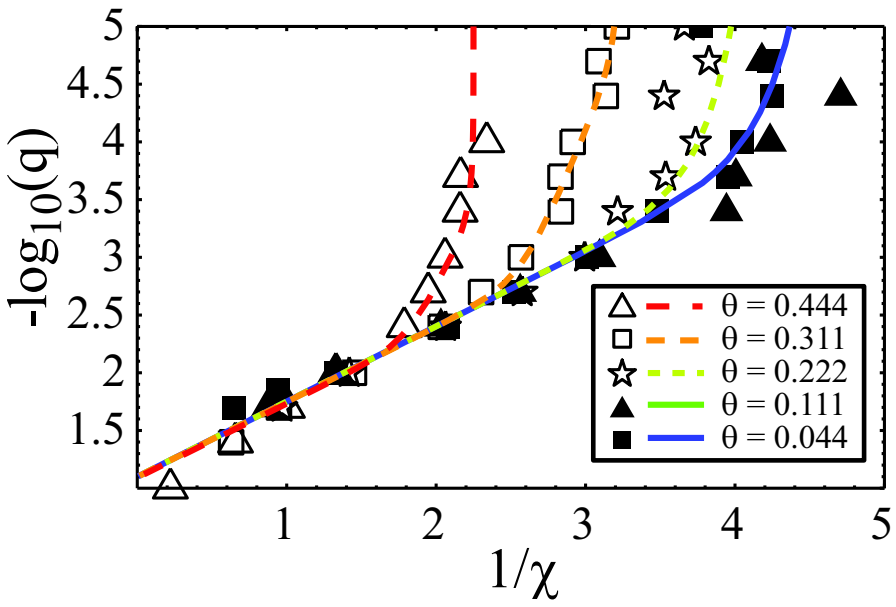

Figure 3.3: The same data as shown in Fig.3.2 but in the form of an Arrhenius plot of $\log_{10}(q)$ as a function of $1/\chi$, for HL results both above (open symbols) and below (solid symbols) the glass transition. The smooth curves are the predictions of the STZ theory at the same temperatures θ.

Similarly, we deduce from the small-q limits of the stress in HL Fig.1a (shown here in Fig. 3.6) that, for $\theta < \theta_0$, $s_y \cong s_0$ is roughly a linearly decreasing function of θ. There is no comparably systematic way to evaluate $s_0(\theta)$ for $\theta > \theta_0$; but we see no structure in these curves that might indicate a further decrease of the stress scale $s_0(\theta)$ at temperatures above θ_0. Accordingly, we choose

$$s_0(\theta) \cong \begin{cases} 1 - c\,\theta/\theta_0 & \text{for } \theta < \theta_0 \\ 1 - c & \text{for } \theta > \theta_0, \end{cases} \tag{3.26}$$

where $c \cong 0.6$.

The parameter ϵ_0, in our notation, is proportional to the number density of STZ's in the limit of infinite χ, modified by a time-scale conversion factor of order unity. We have found no independent estimate of ϵ_0 comparable to the preceding estimates of T_Z, A, n, etc.; but we expect it to be small if the STZ theory is to remain valid at large values of χ. Eq. (3.24) provides an additional constraint. As discussed in the next section, the stress crossover behavior for the full set of HL data provides an estimate of $s_1 \cong 0.08$, and this implies that $\epsilon_0 \cong .006$.

Our next step is to use the parameters determined so far to compare the HL viscosity shown in Fig. 3.1a with the STZ predictions and thereby evaluate the parameters that occur in Eqs. (3.16), (3.17), and (3.19). Figure 3.4 shows the HL data for $\log(s/q)$ as a function of $\log(q)$ at temperatures above and below the glass transition. By definition, the HL viscosity is $\eta = \sigma_{HL}\, s/\dot{\gamma}$ in the limit $s \to 0$, and the HL viscosity data in Fig. 3.1a are based on extrapolation of the data in Fig. 3.4 to $s = 0$ using the Cross equation, a phenomenological law describing the rheology of colloids [69].

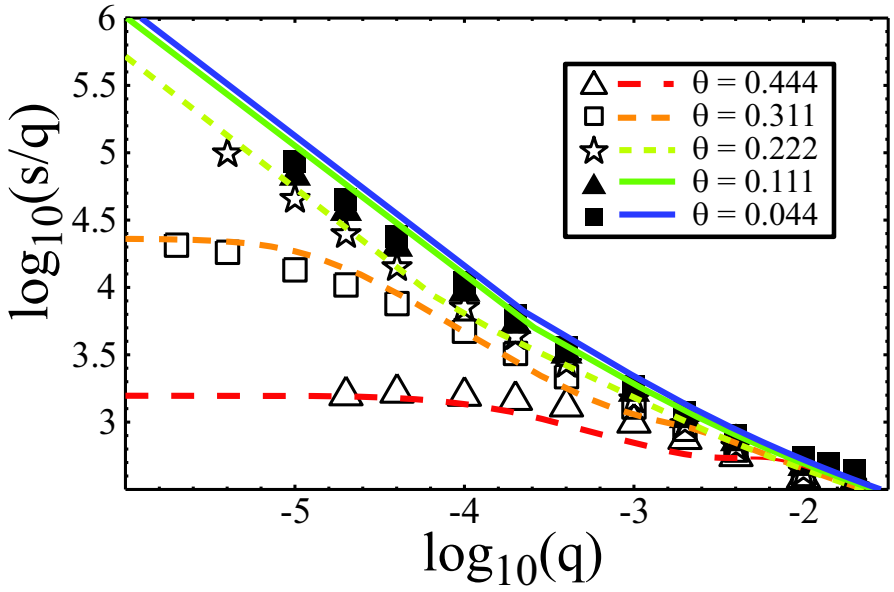

Figure 3.4: Logarithm of the stress s divided by q as a function of $\log(q)$ for HL results at temperatures both above (open symbols) and below (solid symbols) the glass transition. The curves are the predictions of the STZ theory at the same temperatures. For temperatures below the glass transition, the limit as $s \to 0$ of s/q is the Newtonian viscosity, η.

To evaluate η, we use Eqs.(3.3), (3.7), and (3.10) with $\chi = \theta$, and, after some algebra, find that

$$\begin{aligned} \eta_0(\theta) &= \frac{\sigma_{HL}}{\epsilon_0\, \mathcal{T}'(0)} \left[1 + \frac{\rho(\theta)}{2\,\mathcal{C}(0)}\right] \\ &= \frac{\sigma_{HL}\, \tilde{\mu}\, \theta}{\epsilon_0\, \theta_E} \left[1 + \frac{1}{2}\rho(\theta)\, e^{\theta_E/\theta}\right]. \end{aligned} \tag{3.27}$$

The second version of this equation makes explicit use of Eqs.(3.16) and (3.17). Obviously there are too many parameters here for us to obtain more than a very rough estimate of their range of values. None of the six HL data points for η are close enough to the transition temperature θ_0 to provide an accurate picture of the super-Arrhenius singularity. To make matters worse, the highest reported temperature is approximately equal to T_Z, well above any reasonable value for θ_E and thus far too high for the Eyring formula to be valid. Nevertheless, we find some interesting information by exploring the ways in which we can fit the theory to the data.

Our procedure has been simply to use Eq.(3.27) in conjunction with Eq.(3.1) to plot the logarithm of $\eta(\theta)$ and compare the results with the HL data points. To start, we accept the values $T_Z \cong 0.0045$ (in HL units), obtained from the large-stress behavior, and $\theta_0 \cong 0.20$ estimated by HL. We also fix $p = 1$ and $b = 3$ in Eq.(3.19). Then our best-fit parameters are $\theta_A \cong 0.69$, $\theta_1 \cong 0.69$, $\tilde{\mu} \cong 0.3$, and $\theta_E \cong 0.4$. Our fit to the HL viscosity measurements is shown in Fig. 3.1(a). The dashed part of that curve indicates the region where, given the above value of θ_E, we know that the Eyring formula in Eq.(3.14) cannot be valid.

In contrast to the uncertainties that complicate the theoretical fit to the HL viscosity data, the analogous relation between the strain rate and the effective temperature shown in Fig. 3.1(b) seems relatively easy to understand. Whereas the viscosity is an intrinsically dynamic quantity, involving material-specific relations between stress and plastic response, the function $q(\chi)$ appears to be, as we have postulated, a purely kinetic relationship. The solid curve shown in Fig. 3.1(b) is a fit to Eq.(3.2) with the following parameters defined in Eq. (3.20); $\chi_0 = 0.20$, $\chi_A = 0.30$, $\chi_1 = 0.26$, $p = 1$, and $b = 3$. We emphasize that there are still substantial uncertainties in these numbers. Within these uncertainties, it appears that $\chi_0 \cong \theta_0$.

At the outset, it might seem plausible to set $\theta_0 = \chi_0$ and thereby assume that there is only one energy scale that determines both the thermal and effective glass temperatures. This simplification cannot always be correct, however, because we know from the ubiquitous appearance of transient stress peaks in stress-strain curves measured at high strain rates that slow thermal quenches can bring glasses into states where $\theta_0 < \chi < \chi_0$.

The conventional interpretation of these stress peaks is that the as-quenched state of the system has a low fictive temperature χ with a correspondingly small population of STZ's, and that plastic flow cannot begin until enough deformation has occurred to increase χ to a value of order χ_0. The fictive temperature is the thermal temperature at which the system falls out of equilibrium and enters the glass transition region, and therefore it cannot be below θ_0. (A particularly clear

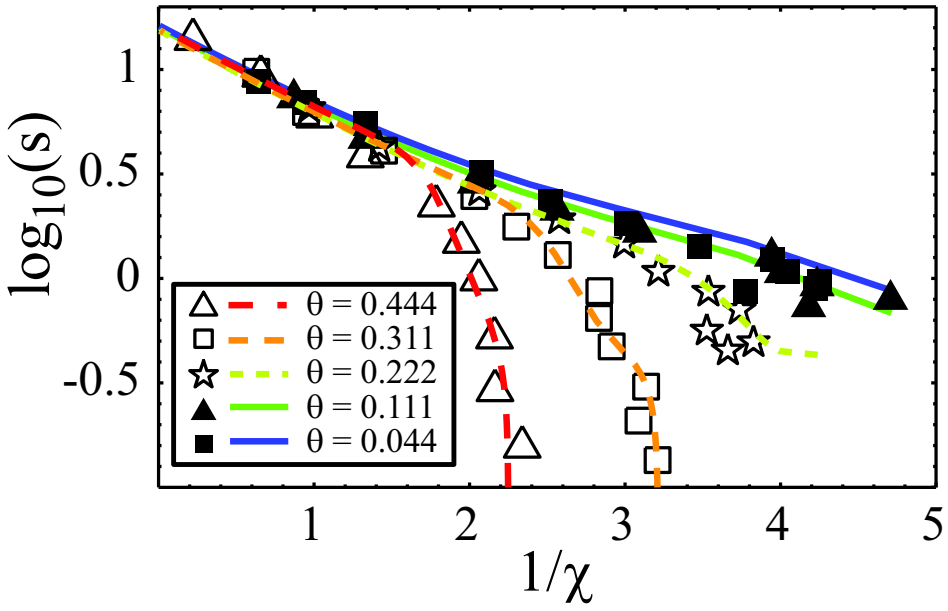

Figure 3.5: Logarithm of the stress s as a function of $1/\chi$ for HL results at temperatures both above (open symbols) and below (solid symbols) the glass transition. The curves are the predictions of the STZ theory at the same temperatures.

discussion of the difference between effective and fictive temperatures is given in Section Vi of Ref. [37].) Therefore, stress peaks could not be produced by this process if $\theta_0 = \chi_0$. In this situation, we expect that the HL model would not exhibit stress peaks except, possibly, at very high strain rates where $\hat{\chi}(q)$ is substantially larger than χ_0.

In exploring fits to the viscosity data, however, we find one intriguingly different possibility. We can fit the HL viscosity data with $p = 2$ in Eq.(3.19) – the prediction of the excitation-chain theory – but this fit looks best if we reduce θ_0 to about 0.1, i.e. half the previous estimate. This lowered transition temperature would mean, for example, that the HL curves of stress versus strain rate shown in Fig.3.6 for values of θ down to 0.1, would bend over and exhibit viscous behavior at strain rates much smaller than those measured by HL. If that were the case, then χ_0 would be substantially higher than θ_0, and the transient behavior of the HL model might be more interesting than predicted at the end of the last paragraph.

3.3.2 Comparisons over the Full Range of the HL Data

In order to extend our analysis to temperatures above the glass transition (Kauzmann) temperature θ_0 and to arbitrary strain rates, we must reexamine our assumption that the effective Kauzmann temperature χ_0 is independent of the bath temperature θ. To see what is happening here, we take advantage of our simplifying assumption that $\beta = 1$ in Eq.(3.6) and solve this equation for χ:

$$\frac{1}{\chi} = \frac{\Gamma(s,\theta)/\hat{\chi}(q) + \kappa\,\rho(\theta)/\theta}{\Gamma(s,\theta) + \kappa\,\rho(\theta)}. \tag{3.28}$$

Note that, for $\theta > \theta_0$, we can take the limits $q \to 0$ and $\theta \to \theta_0$ in different orders and get different answers. If we take the limit of vanishing q first, so that $\Gamma(s,\theta)$ vanishes, then $\chi \to \theta$. However, if we let θ go to θ_0 first, so that $\rho(\theta)$ vanishes, then $\chi \to \hat{\chi}(q) \to \chi_0$ for sufficiently small q. We see no *a priori* reason why the crossover between these limiting behaviors described by Eq.(3.28) cannot be physically correct for a temperature independent χ_0; but that assumption is qualitatively inconsistent with the HL data. Equation (3.28) implies that χ always must lie between θ and $\hat{\chi}(q)$; but we have found (in a calculation not shown here) that, if we choose $\chi_0 = \theta_0$ to be a θ-independent constant, then the HL data in Fig.3.2 for $\theta = 0.31$ and 0.44 lie above the allowed range in the transition region between the small-q and large-q limits.

A physically plausible alternative is to assume first that $\chi_0 \geq \theta_0$ (the inequality being consistent with the existence of transient stress peaks), and then that $\hat{\chi}(q \to 0) = \theta$ whenever θ exceeds χ_0. That is,

$$\lim_{q\to 0} \hat{\chi}(q) = \begin{cases} \chi_0 & \text{if } \theta < \chi_0 \\ \theta & \text{if } \theta > \chi_0. \end{cases} \tag{3.29}$$

With this assumption, $\hat{\chi}(q \to 0)$ is a continuous function of θ across the glass transition and, for $\theta > \chi_0$, there are no small-q steady-state solutions other than $\chi = \theta$. Nothing in this hypothesis precludes χ_0 itself from being a function of temperature. In fact, we think we see a hint in the HL data that χ_0 may be a decreasing function of θ up to the point where $\theta = \chi_0$, beyond which $\hat{\chi}(q \to 0) = \theta$.

The assumption in Eq.(3.29) accurately fits the HL data. In implementing Eq.(3.29), we have simply rescaled the parameters χ_A and χ_1 in Eq.(3.20) so that the ratios χ_A/χ_0 and χ_1/χ_0 remain the same in both low and high temperature regions. We also have chosen $\kappa = 5$ in Eq.(3.6) and $\tilde{\mu} = 0.3$ in Eq.(3.14). Our results are shown in Figs. 3.2, 3.3, 3.5, and 3.6.

Figure 3.2 shows χ as a function of strain rate q for a set of temperatures θ both above and below θ_0. As expected, the HL data and STZ curves collapse

to roughly a single curve for temperatures below θ_0. Above θ_0, as predicted by Eq.(3.28), $\chi \to \theta$ in the limit of small q; and the crossover to large-q behavior is correctly predicted by the theory. Figure 3.3 shows the same data as in Fig. 3.2 but here as the Arrhenius plot, Fig. 3.1b, with the high-temperature data included. We show this different view of the data to emphasize that even the high-temperature values of χ collapse to a single Arrhenius line, extrapolating to a single "melting" strain rate q_0, in the limit of infinite χ.

Similarly, the graphs of stress s as functions of $1/\chi$ in Fig. 3.5, and those for s as functions of strain rate in Figs. 3.6(a) and (b), show good agreement between theory and simulations at all temperatures and stresses. As in the preceding figures, these curves and the corresponding HL data points are shown at a selection of temperatures above and below θ_0. Note, in Fig. 3.6, that the curves for $\theta > \theta_0$ make smooth transitions to linear viscous behavior at small strain rates. As expected, the curves for $\theta < \theta_0$ level off at temperature-dependent yield stresses. The short-dashed lines in Fig. 3.6(a) illustrate the bifurcation at θ_0. At temperatures just above θ_0, the material appears to exhibit a yield stress down to very small strain rates, but eventually flows even in the limit of arbitrarily small stress, thus showing how hard it is to make an accurate estimate of θ_0 by going to smaller and smaller strain rates.

Two material-specific parameters, $\tilde{\mu}$ and s_1, are best constrained using the HL data for $\log(s/q)$ vs. $\log(q)$, shown in Fig. 3.4. The small strain-rate asymptote of these curves for temperatures above the glass transition is $\log(\eta(\theta))$, and the way in which the stress crosses over from its power-law dependence at large q to the yield stress or Newtonian viscosity at small q is strongly sensitive to STZ transition rate parameters $\tilde{\mu}$ and s_1. We find that $\tilde{\mu} \cong 0.3$ and $s_1 \cong 0.08$ fit the crossover behavior quite well.

The curves in Fig. 3.4 show the STZ solutions for $\log(s/q)$ vs. $\log(q)$ at temperatures above and below the glass transition. For temperatures above the glass transition, $\hat{\eta}(q) = s/q$ is very similar to the Cross form used by HL to extrapolate their data. However, the STZ solutions for $\hat{\eta}(q)$ asymptote to a slightly smaller value of η as $q \to 0$ than the one specified by HL. It is unclear how to best extrapolate this stress/strain rate data to $s = 0$, and this uncertainty explains why the HL viscosity values in Fig. 3.1a are slightly larger than the STZ fit.

3.4 Concluding Remarks for Chapter 3

The natural way in which the STZ theory accounts for the wealth of data provided by the Haxton-Liu simulations lends credibility to major elements of

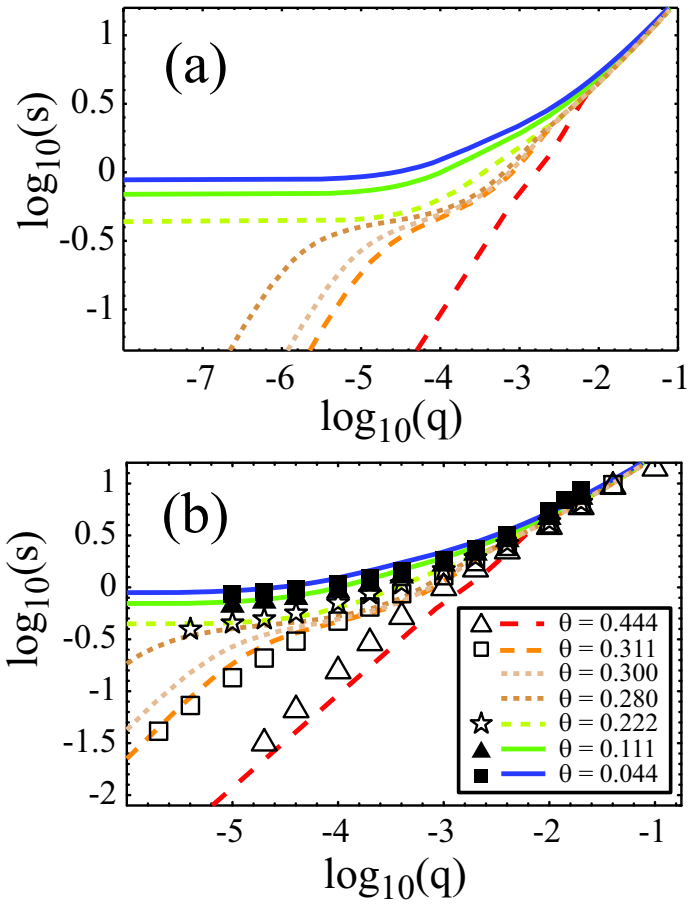

Figure 3.6: (a) Theoretical log-log plots of stress s as a function of strain rate q for a range of temperatures above and below the glass transition. The short-dashed curves are for $\theta = 0.28$ and $\theta = 0.30$, both just above the glass transition temperature $\theta_0 = 0.2$. (b) The same as (a) but for a smaller range of strain rates and including HL data at the selected temperatures

the theory, especially the form of the expression for the plastic strain rate in Eq.(3.3) and the central role played by the effective disorder temperature. The self-consistent evaluation of parameters in Section 3.3 depends directly on the first of these elements; and the remarkable appearance of an effective glass transition in the nonequilibrium glassy state seems to confirm the second. Nevertheless, unanswered questions abound. We conclude by listing some of them.

How close is the analogy between the thermal and effective-thermal glass transitions? The analogy does seem surprisingly close, but there are interesting and

potentially very important differences. We think that the near equality of the transition temperatures θ_0 and χ_0, if correct at all, must be an artifact of the HL simulation model. We have argued here that θ_0 must be substantially smaller than χ_0 in many realistic circumstances; and we suspect that this inequality might even turn out to be true in the HL simulations if measurements could be made at appreciably smaller strain rates. It already is apparent that the effective Arrhenius activation energy $A\,k_B\,T_Z$ in Eq.(3.2) is larger than the thermal activation energy $k_B\,T_Z$ by a factor of about 1.5; thus there is no universality in the energy scales. Why not?

We see an even deeper question in this regard. As discussed in the paragraph preceding Eq.(3.2), the fact that $\hat{\chi}(q)$ goes to a nonzero value χ_0 in the limit of small q seems to have a robust explanation in purely kinetic terms. Is a similar argument relevant to the thermal glass transition? Would it imply that the viscosity – the analog of q^{-1} – rigorously does diverge at θ_0?

What should the STZ transition rate $R(s)$ really look like? Which features of it are model dependent? Which have some degree of universality? In Eq.(3.14), we have tried to go part of the way toward deducing $R(s)$ from first-principles, many-body physics. Doing this correctly would be analogous to using statistical mechanics to compute the viscosity in the Navier Stokes equations. The problem here is harder, of course, because we do not yet have a precise definition of an STZ. Nevertheless, this problem needs to be given more thought in view of the new information we have obtained from the HL results.

One especially intriguing aspect of this question emerges from our observation that $R(s)$ exhibits Bagnold scaling at large s. Under what circumstances may we expect this to happen? Is it special to the HL model? Ordinarily, we think of Bagnold scaling as being relevant to the large-stress behavior of the strain rate as a whole, i.e. to $q(s)$ in present notation; whereas our $q(s)$ behaves quite differently. The special feature here is that the Bagnold behavior is modified by the STZ density, i.e. the factor $\exp(-1/\chi)$ in Eq.(3.3), which is strongly q dependent. We suspect that the full Bagnold behavior would occur at strain rates larger than q_0, where the STZ density is not a meaningful quantity, but where the HL model might look like a rapidly flowing granular material. A better understanding of this large-q situation might provide insight regarding the applicability of STZ theory to granular systems.

Will the present version of the STZ theory accurately predict the time-dependent transient behavior of the HL model? One of the principal successes of earlier applications of the STZ theory has been that it correctly accounts for response times observed, for example, in transient stress-strain experiments. The key idea here is that there is a separation of time scales between slow processes, i.e. relax-

ation of plastic flow or disorder temperature, as opposed to fast processes like the response to perturbations of the STZ orientation variable m that appears in Eq.(3.10). That separation seems problematic at the upper end of the scale of strain rates used by HL. We have no problem with it here because we consider only steady-state behavior.

It will be interesting to look at transient behavior in the HL model to see where the fully dynamic version of the STZ theory may break down. Before doing that, however, it will be important to look at less esoteric behavior, e.g. transient responses to changes in driving forces of systems initially quenched at different rates to temperatures near the glass transition. Do such systems exhibit stress peaks? The model that we have used for interpreting the HL data, in which $\chi_0 = \theta_0$, implies that they should not occur here. Might transient experiments reveal that, as we suspect, $\chi_0 > \theta_0$?

What are the implications for strain localization? The effective temperature provides a mechanism for strain localization in amorphous materials – regions with a higher effective temperature are more likely to undergo plastic deformation, which generates heat that increases the local effective temperature. Although previous studies assumed a constant value for $\hat{\chi}$ [70], Eq. (3.2) shows that this assumption is only valid near the effective glass transition. The fact that $\hat{\chi}$ increases with increasing strain rate is likely to enhance localization and may permit steady state localized solutions.

What role do thermal fluctuations play in determining the properties of the effective glass transition? We already have concluded that $\hat{\chi}(q \to 0)$ must be equal to θ at high temperatures, $\theta > \chi_0$; but we have little knowledge about what happens to the corresponding χ_0 when $\theta < \chi_0$, and have simply assumed that it is a constant. More detailed information about this quantity might help us understand the molecular mechanisms that are at work here.

Chapter 4

Free volume vs. effective temperature

As discussed in the introduction, there have been several different formulations of STZ theory. In earlier versions, the rate at which STZ flip was defined to be a function activated by free volume [47, 51, 54]. In these descriptions, the free volume (FV) does not affect the structural properties of the packings, but instead activates the dynamics. This is an intuitively attractive idea which has been used recently as a model for aging in polymer glasses [71]. However, it is difficult to derive an equation for the free volume dynamics from first principles, although phenomenological models are possible [51].

An alternative idea is that the free volume is simply a proxy for a more general effective temperature(ET) variable which describes the configurational disorder of the amorphous packings [52]. In this formulation, the effective temperature does not activate STZ flips – instead it specifies the probability of various configurational packings. Regions with more disorder contain a higher density of STZs. This approach is attractive because the effective temperature can be measured using the fluctuation-dissipation theorem (FDT), and an equation for heat flow in the system specifies the effective temperature dynamics.

In fact, the association of free volume with activated rates and the effective temperature with activated structures is largely historical, and not necessary. As we discuss below, the effective temperature is a more general parameterization of configurational disorder than the free volume, but the effective temperature reduces to the free volume in many situations. We will use the acronym AR to indicate a formulation with activated rates (like the original free volume law) and AS to indicate activated structures (as in the original effective temperature law). However, it is possible to construct theories using either the free volume or the

effective temperature as the internal state variable in both cases.

An open question is which formulation is more appropriate for a particular amorphous material. In this chapter, we show that although conceptually the AR and AS descriptions are very different, in the athermal limit they actually generate very similar final sets of continuum partial differential equations. This suggests that macroscopic measurements can not distinguish between these formulations, and that some data sets which have been described by the AR theory are also likely amenable to an AS description. Conversely, much of the analysis of transient instabilities and shear banding in an effective temperature description carries over to free volume formulations.

4.1 Equations of motion

The equation of motion for the STZ number densities, Eq. 2.7, can be rewritten in the following form:

$$\dot{n}_{\pm} = R_{\mp} n_{\mp} - R_{\pm} n_{\pm} - \Gamma \left(A_a n_{\pm} - A_c \right), \tag{4.1}$$

and the plastic strain rate is

$$\dot{\gamma} = R_0 A_0 \left(R_+ n_+ - R_- n_- \right). \tag{4.2}$$

The AR and AS formulations of STZ theory determine the parameters in this equation differently.

4.1.1 Activated Rate model

The details in this section are taken from work by Anael Lemaitre [51, 54]. Define $\widetilde{\chi} \equiv v_f / v_c$, where v_f is the free volume and v_c is an "activation volume" necessary for rearrangement events. Then assume that the rates have an Arrhenius dependence on the free volume:

$$R_{\pm} = r(s) e^{-1/\widetilde{\chi}}, \tag{4.3}$$

where $r(s)$ is a function of the applied stress only. This assumption means that the rate of switching is an activated process. In other words, the system requires a volume fluctuation of size v_c for an STZ to switch orientation and the probability of such a volume fluctuation is proportional to $\exp[v_c/v_f]$.

Lemaitre postulates that the free volume has the following governing equation:

$$\dot{\widetilde{\chi}} = \widetilde{\Gamma} - A_r e^{-v_a/\widetilde{\chi}}, \tag{4.4}$$

where v_a is an activation volume required for a local collapse or annihilation event, and $\widetilde{\Gamma}$ is the work done on the system $|s\dot{\gamma}|$. We note that this is different from Langer's definition [52, 57] that Γ is the energy dissipated *per STZ*.

This results in equations of motion for $\widetilde{m}$ and $\widetilde{\Lambda}$:

$$\dot{\widetilde{\Lambda}} = \frac{\widetilde{R}_0\kappa}{\widetilde{\epsilon}_0}\widetilde{\Gamma}(1-\widetilde{\Lambda}), \tag{4.5}$$

$$\dot{\widetilde{m}} = \frac{\widetilde{R}_0}{\widetilde{\epsilon}_0}\left(\frac{\dot{\gamma}}{\widetilde{\Lambda}} - \kappa\widetilde{\Gamma}\widetilde{m}\right), \tag{4.6}$$

where κ and $\widetilde{\epsilon}_0$ are constants involving A_0, A_a, and A_c. The term $\widetilde{R}_0$ is a intrinsic rate factor. We can rewrite Eq. 4.2 for the strain rate $\dot{\widetilde{\gamma}}$:

$$\dot{\widetilde{\gamma}} = 2\widetilde{\epsilon}_0\widetilde{R}_0\widetilde{C}(s,\chi)\Lambda\left(\widetilde{T}(s,\chi) - \widetilde{m}\right), \tag{4.7}$$

where $\widetilde{C}(s,\chi) = 1/2(R_+ + R_-)$ and $\widetilde{T}(s,\chi) = (R_+ - R_-)/(2\widetilde{C}(s,\chi))$.

4.1.2 Activated Structure model

As discussed in Chap. 2, the effective temperature formulation assumes that the density of STZs must be governed by the configurational disorder, which corresponds to a configurational temperature T_{eff}. In simple shear, and in the athermal limit when thermal fluctuations are nonexistent, the creation rate A_c in Eq. 4.1, is given by:

$$A_c = \frac{n_\infty e^{-1/\chi}}{2A_a}, \tag{4.8}$$

where $\chi = T_{eff}/T_z$, and T_z is the energy required to form an STZ. The rates are simply functions of the stress, $R(s) = r(s)$. Combining Eq. 4.1, 4.2 and 4.8 results in the following equations:

$$\dot{m} = R_0\left(\frac{\dot{\gamma}}{\epsilon_0\Lambda} - m\Gamma\frac{e^{-1/\chi}}{\Lambda}\right), \tag{4.9}$$

$$\dot{\Lambda} = R_0\,\Gamma\left(e^{-1/\chi} - \Lambda\right), \tag{4.10}$$

$$\dot{\gamma} = 2R_0\epsilon_0\Lambda\mathcal{C}(s)\left(\mathcal{T}(s) - m\right), \tag{4.11}$$

where $\mathcal{C}(s,\chi) = 1/2(r_+ + r_-)$ and $\mathcal{T}(s,\chi) = (r_+ - r_-)/(2\mathcal{C}(s,\chi))$, and the rate $R_0 = 1/\tau_0$.

The equation for the effective temperature in the athermal limit, Eq. 2.35, can be written as

$$\dot{\chi} = \frac{Q_c}{c_0 \chi_0} (\chi_0 - \chi) + D \frac{\partial^2 \chi}{\partial y^2}, \tag{4.12}$$

where Q_c is the configurational component of the energy dissipation rate.

As in Eq. 2.13, the configurational energy dissipated per unit volume is proportional to Γ: $Q_c = (\phi s_0 \epsilon_0 R_0)\, \Gamma\Lambda$, where ϕ is the fraction of the dissipated energy that goes into the configurational degrees of freedom. In simple shear, Eq. 2.2 can be used to determine the total energy dissipation rate: $\tau_0 \dot{\gamma}\, s = 2s\, f(s) \exp[-1/\chi]$. Then Eq. 2.20 can be used to relate the macroscopic dissipation rate to Q_c:

$$s_0 \epsilon_0 R_0\, \Gamma\, e^{-1/\chi} = s\, \dot{\gamma}; \tag{4.13}$$

$$Q_c = \phi\, s\, \dot{\gamma}. \tag{4.14}$$

Because the system is in simple, uniform shear, s and $\dot{\gamma}$ are always positive and Q_c is positive.

4.2 Reconciling the m and Λ dynamics

Note that $\widetilde{C}(s,\chi) = e^{-1/\widetilde{\chi}} \mathcal{C}(s)$, $\widetilde{T}(s,\chi) = \mathcal{T}(s)$, and $\widetilde{\Gamma} = s\dot{\gamma} = (s_0 \epsilon_0)\, \Gamma\Lambda$. Also, we assert that in both models the STZ density Λ rapidly attains its steady state value so that $\widetilde{\Lambda} = 1$ and $\Lambda = e^{-1/\chi}$. Then the AR law states

$$\dot{\widetilde{m}} = \frac{1}{\widetilde{\epsilon}_0} \left(\dot{\gamma} - \kappa \widetilde{\Gamma} \widetilde{m} \right), \tag{4.15}$$

$$\dot{\widetilde{\gamma}} = 2\widetilde{\epsilon}_0 \widetilde{R}_0 e^{-1/\widetilde{\chi}} C(s)(T(s) - \widetilde{m}), \tag{4.16}$$

and the AS law states

$$\dot{m} = \frac{R_0}{\epsilon_0 e^{-1/\chi}} \left(\dot{\gamma} - \frac{m\widetilde{\Gamma}}{s_0} \right), \tag{4.17}$$

$$\dot{\gamma} = 2\epsilon_0 R_0 e^{-1/\chi}\, \mathcal{C}(s)(\mathcal{T}(s) - m). \tag{4.18}$$

These equations are dynamically the same, with $\kappa = 1/s_0$, $\widetilde{R}_0 = R_0^2/\Lambda$ and $\widetilde{\epsilon}_0 = \epsilon_0 \Lambda / R_0$, although they are interpreted differently. In the AR law, the density of STZs is unity, while in the AS law the density of STZs is governed by statistical distributions of the packing and is therefore proportional to $e^{-1/\chi}$. The AR law assumes that the *rates* are activated by the effective temperature, while the AS law assumes that the rates are functions of the stress only.

This corresponds to two different interpretations on how the disorder affects the material. In the AS case, the configurational packing (and corresponding number of STZs) *is* a statistical distribution, and the probability of a given density fluctuation is $e^{-E_z/k_B T_{eff}}$, where E_z is the energy of that fluctuation. In contrast, the AR law arises naturally from an energy landscape perspective – the system begins in a metastable state and volume fluctuations of size v_c must occur to drive the system to another metastable state.

The question is whether the **structure** or the **dynamics** evolve according to χ: In the former case, the configurational packing/inherent states/density fluctuations evolve according to the effective temperature and determine the number of STZs, which flip at a constant rate. In the latter, the configurational packing/ number of STZs is constant and density fluctuations enable the STZs to flip at a rate which is activated by χ.

4.3 Reconciling the χ dynamics

The AR and AS equations for $\widetilde{\chi}$ and χ in simple, uniform shear are:

$$\dot{\widetilde{\chi}} = \widetilde{R}_0 \left(s\,\dot{\gamma} - A_r e^{-v_a/\widetilde{\chi}} \right), \tag{4.19}$$

$$\dot{\chi} = \frac{\phi\, s\,\dot{\gamma}}{c_0} \left(\hat{\chi} - \chi \right). \tag{4.20}$$

The first equation indicates that $\widetilde{\chi}$ increases as energy is dissipated and decreases according to a process that is activated by the free volume. The steady state dimensionless free volume ($\hat{\chi}_{AR}$) is determined *dynamically* by the first equation. In contrast, the equation of motion for the effective temperature states that χ approaches its steady state value $\hat{\chi}$ as energy is dissipated, and we must specify $\hat{\chi}$ using a separate equation.

To see how Eq. 4.19 and 4.20 are related, we first note that the steady state solution of Eq. 4.19 is given by:

$$s_{ss}\dot{\gamma}_{ss} = A_r e^{-1/\hat{\chi}_{AR}}. \tag{4.21}$$

When $\widetilde{\chi}$ is close to its steady state value, $\hat{\chi}_{AR}$, we expand the LHS of equation 4.19 as a series in $\delta\chi = \hat{\chi}_{AR} - \widetilde{\chi}$.

$$\dot{\widetilde{\chi}} = -\delta\chi \, \frac{R_0 A_r v_a}{\hat{\chi}_{AR}^2} \exp\left[\frac{-v_a}{\hat{\chi}_{AR}} \right]. \tag{4.22}$$

Substituting Eq. 4.21 into Eq. 4.22, we find the following expression:

$$\dot{\widetilde{\chi}} = \frac{R_0 v_a \, s_{ss} \, \dot{\gamma}_{ss}}{\hat{\chi}_{AR}^2} \left(\hat{\chi}_{AR} - \widetilde{\chi} \right). \tag{4.23}$$

Comparing Eqs. 4.23 and 4.20, we find that they exhibit similar behavior.

Eq. 4.19 is conceptually simple because the steady state χ results from a balance between creation and annihilation of free volume. Although the microscopic mechanisms that give rise to the annihilation term are not well understood, the phenomenological AR model permits a dynamic balance of the two processes. In contrast, Eq. 4.20 suggests that $q(\hat{\chi})$ is a fundamental rate processes requiring heterogeneous particle motion activated by the effective temperature, which can not be described by a simple balance equation. Instead, this process is best described using a theory similar to that used for heterogeneous dynamics near the glass transition, such as excitation chains [68].

In Chapter 3, we saw that $\hat{\chi}$, the steady state value of the effective temperature, begins to increase at high strain rates. This rate-dependence fits into either a AR or AS framework. Haxton and Liu [72] and Bouchbinder [73] have suggested that the term A_r is proportional to the strain rate. In other words, the rate at which free volume relaxes is proportional to the rate at which the particles are rearranging, rather than the inherent timescale $\tau_0 = 1/R_0$. Under this assumption, Eq. 4.19 results in a steady state value for $\hat{\chi}$ that matches the HL data in the Arrhenius regime, but not in the super-Arrhenius regime.

Contrast this with the effective temperature framework, which assumes as in Chapter 3 that the strain rate $q = \dot{\gamma}\tau_0$ is an activated process of the steady state effective temperature:

$$q(\chi_{ss}) = q_0 \exp\left(-A/\chi_{ss} + \alpha_{eff}(\chi_{ss})\right). \tag{4.24}$$

Eq. 4.24 only applies to steady state, when an ergodic hypothesis is valid. It is a statistical definition for the rate of plastic deformation that is independent of the magnitude of the stress or details of the rearrangements. Although it requires additional parameters to define the diverging function α_{eff}, this formulation is nice because it explicitly captures Arrhenius and super-Arrhenius behavior.

4.4 Discussion

Although historically the free volume has been described by an AR model, and the effective temperature has been described by an AS model, is there any reason to think that the FV and ET are different from one another? Simulations of a

Lennard-Jones glass by Shi *et al.*, detailed in Chapter 5, show that the potential energy per atom (PE) is significantly higher in regions where shear banding occurs. In a Lennard-Jones glass, higher PE generally indicates more configurational disorder, but not necessarily more free volume [74]. This supports the effective temperature formulation, since that formulation predicts higher effective temperature but not higher free volume in the band. However, in other glass formers shear bands do contain more free volume [74]. This suggests that the effective temperature formulation is more general, though in many materials the effective temperature and free volume are roughly equivalent.

We have seen that the AR and AS STZ formulations are remarkably similar in their predictions. Is one of them more useful? Is one of them better at describing experimental results? Simulation results indicate that glassy materials are *structurally* different under different shearing conditions and preparations. For example, glassy materials which have been quenched quickly (and are therefore more disordered) generally have a lower elastic modulus [75]. Additionally, Shi and Falk's simulations show that the PE is elevated and short range order is lowered inside shear bands, which indicates that structural changes are taking place [74]. This results support the AS formulation.

As mentioned in Section 4.3, AR formulations are attractive for several reasons. For example, it is intuitively plausible that the free volume/effective temperature activates a rate process, which is one reason the AR theory has been applied to polymer glasses [71]. While the STZ AR theory postulates that the *flipping rates* $\hat{R}(s)$ are activated, the AS formulation suggests that the steady state *plastic deformation* is itself an activated process: $\dot{\gamma} = f(s)e^{-1/\hat{\chi}}$. In this sense, both formulations capture activated dynamics.

The AR formulation is also attractive because it dynamically predicts the steady state effective temperature, instead using a separate theory such as excitation chains to put it in "by hand". It is possible to write an equation for the effective temperature that also dynamically predicts the steady state effective temperature [73], but that equation contains an athermal relaxation term of uncertain physical origin. In addition, no one has yet developed a theory that incorporates a dynamic steady state and recovers the super-Arrhenius portion of the $\hat{\chi}$ curve. Understanding the physical processes that give rise to the function $\hat{\chi}(q)$ is an interesting open problem that deserves more study.

Although the AR and AS STZ descriptions were formulated separately, it possible that deformation is actually modeled by a combination of activated structures **and** activated rates. In other words, it should be possible to construct a theory where $R(s)$ and Λ are both activated by the effective temperature, with different activation energies. Because these formulations already lead to similar continuum

descriptions, this should be straightforward and might lead to additional insights into the deformation process. This would be an interesting avenue for future research.

Chapter 5

Strain localization at low strain rates

In this chapter, we investigate the transient dynamics of the STZ equations at low temperatures (below the thermal glass transition) and at low strain rates. This greatly simplifies the equation of motion for the effective temperature because there are no thermally activated rearrangements below the glass transition and at low strain rates the steady state effective temperature, $\hat{\chi}$, can be approximated as a constant, χ_0. We find that the STZ equations predict strain localization and match simulation data. The work in this chapter was performed in collaboration with Jim Langer and Jean Carlson and was originally published in Physical Review E [70]. It is presented here with a revised introduction and minor corrections.

5.1 Background

We model sheared material interfaces using the theory of Shear Transformation Zones (STZs). Building on work by Spaepen [44], Argon and Bulatov [45, 46], Falk and Langer [47] introduced a mean-field theory which postulates that shear transformation zones, which correspond to particle configurations that are more susceptible to plastic rearrangements than the surrounding particles, reversibly switch between two orientational states in response to stress. Additionally, these zones are created and annihilated as energy is dissipated in the system. This theory captures many of the features seen in experiments, such as work-hardening and yield stress [48, 49, 50].

As detailed in Chapter 1, the density of STZs is governed by an effective temperature [52]. In these slowly sheared systems, thermal temperature is not

sufficient to cause configurational rearrangements, but the particles ergodically explore configuration space under shear.

The effective temperature is an important macroscopic state variable in this STZ description. It governs the properties of statistical distributions for configurational degrees of freedom in the material, such as density fluctuations. Langer hypothesized that shear transformation zones are unlikely, high-energy density fluctuations, and therefore the number of such zones in a system should be proportional to a Boltzmann factor which here is a function of the effective temperature instead of the usual thermal temperature [52]. In this manner, the density of shear transformation zones is related to the effective temperature and therefore the plastic flow is coupled to the local disorder. This is a mechanism for strain localization because a region with higher disorder is more susceptible to flow under stress and flowing regions become more disordered.

The effective temperature mechanism for strain localization is different from other proposed mechanisms governed by thermal temperature or free volume. Griggs and Baker [19] proposed that the strong temperature dependence of viscosity near the glass transition leads to thermal softening and strain localization. In that formulation the heat generated by plastic work raises the thermal/kinetic temperature, instead of the configurational/effective temperature. Lewandowski and Greer [20] have shown that in a bulk metallic glass the thermal temperature diffuses too quickly to control shear localization in an adiabatic description, though Braeck and Podladchikov [76] have shown that a non-adiabatic thermal theory can explain the data.

Alternatively, several authors have suggested that the free volume governs strain localization [51, 27]. In these descriptions, plastic deformation in the solid is accompanied by a larger free volume, which in turn softens the material. These ideas are discussed in detail in Chapter 4. In this chapter we focus instead on an alternative description: the heat generated by plastic deformation is dissipated in the configurational degrees of freedom, according to the first law of thermodynamics. The local free volume is *related* to the effective temperature (for example, in a Lennard-Jones glass the particles can become more disordered by moving away from their equilibrium separations), but the effective temperature is the relevant macroscopic state variable governing particle dynamics.

The STZ formulation in this chapter is *athermal* – the thermal temperature T does not cause any configurational rearrangements. This is an approximation which is clearly appropriate for bubble rafts and granular materials and may be relevant for metallic glasses well below the glass transition temperature. The athermal approximation significantly simplifies the STZ equations and clarifies the nature of the instability that leads to localization, but the resulting description

does not capture features such as thermally activated creep or relaxation. As we discuss in Section 5.4.4, some behaviors of real materials and simulations are likely due to thermal activation or relaxation and will not be accurately represented in this athermal STZ formulation.

In this chapter we show how athermal STZ theory with effective temperature generates solutions with strain localization. This chapter is divided into sections as follows: Section 5.2 develops the constitutive equations for athermal STZ theory with effective temperature in a simple shear geometry. Section 5.3 compares numerical results from the continuum STZ theory to simulations of Lennard-Jones glasses by Shi, *et al.* We compare macroscopic stress-strain curves for different initial conditions and compare the strain rate and potential energy (PE) as a function of position and time inside the sheared material. Section 5.4 investigates the stability properties of the STZ equations, and presents a description of how shear bands form and remain intact for long times. We show that an instability in the transient dynamics amplifies perturbations to the effective temperature, and that this process interacts with energy dissipation processes to determine the long-time behavior of the local strain rate. Section 5.5 concludes the chapter with a discussion of our results and future directions.

5.2 STZ equations: low temperature, small strain rate, specified boundary velocity

We use the STZ equations defined in Chapter 2 to model a slowly sheared amorphous material at a temperature far below the glass transition temperature.

As noted in Chapter 2, the functional form of Γ is considerably simplified in an athermal description because an STZ can never flip in a direction opposite to the direction of applied stress. Therefore no energy can be stored in the plastic degrees of freedom. The rate at which energy is dissipated per STZ is the rate at which plastic work is done on the system, Q, divided by the volume (area in 2D) density of STZs, $\epsilon_0\Lambda$, where $\epsilon_0 = \lambda n_\infty$. In terms of these new variables, the rate of deformation tensor can be written as:

$$D_{ij}^{pl} = \frac{\epsilon_0}{\tau_0}\mathcal{C}(\overline{s})(\frac{s_{ij}}{\overline{s}} - m_{ij})\Lambda, \tag{5.1}$$

and the energy dissipated per STZ is

$$\begin{aligned} \Gamma &= \frac{Q}{\epsilon_0 \Lambda} \\ &= \frac{s_{ij} D_{ij}^{pl}}{\epsilon_0 \Lambda}, \end{aligned} \tag{5.2}$$

We use the following equation to describe the χ dynamics:

$$\dot{\chi} = \frac{1}{c_0} \Gamma \epsilon_0 \Lambda \left(\chi_0 - \chi \right) + D_\chi \frac{\partial^2 \chi}{\partial y^2}. \tag{5.3}$$

The equation of motion for χ used here is similar to Eq. 2.35, but the term $(1 - \chi/\chi_0)$ is replaced by a term $(\chi_0 - \chi)$. The expression $(1 - \chi/\chi_0)$ is more recent and general because it remains well behaved at high strain rates, in the limit $\chi \to \infty$. In the low strain rate limit, however, both versions are nearly indistinguishable: they generate the same steady state behavior, and differ only by a factor $\chi/\hat{\chi}$, which is close to unity in the low strain rate regime.

We will now derive the STZ equations of motion in the geometry of a two-dimensional infinite strip driven by the boundaries in simple shear. This is the geometry illustrated in Fig. 1.2.Let x be the direction of the velocity at the boundaries, and y be normal to these boundaries. The speed at the boundaries is V_0 and the width is L. Therefore the average strain rate inside the material is $\overline{\dot{\gamma}} \equiv V_0/L$, while the local strain rate is denoted $\dot{\gamma} \equiv \partial v_x/\partial y \equiv 2D_{xy}^{total}$. Assuming that there are no pressure gradients, Eq. (2.5) requires that the pressure field remain constant in time.

The stress s and STZ bias m are traceless tensors. Let the off-diagonal elements of the tensors be denoted by $s = s_{xy} = s_{yx}$ and $m = m_{xy} = m_{yx}$ and the diagonal elements by $s_0 = s_{xx} = -s_{yy}$ and $m_0 = m_{xx} = -m_{yy}$. By symmetry, all fields are constant in x, and Eq. (2.4) shows the stress tensor is constant in the y direction as well. Substituting this into Eq. (5.1) we find that the plastic rate of deformation tensor then has two independent components:

$$D^{pl} = \frac{\epsilon_0}{\tau_0} \mathcal{C}(\overline{s}) \left(\frac{s}{\overline{s}} - m \right) \Lambda; \tag{5.4}$$

$$D_0^{pl} = \frac{\epsilon_0}{\tau_0} \mathcal{C}(\overline{s}) \left(\frac{s_0}{\overline{s}} - m_0 \right) \Lambda, \tag{5.5}$$

and the energy dissipation per STZ, Γ, is given by:

$$\begin{aligned}\Gamma &= 2\frac{D_0^{pl}s_0 + D^{pl}s}{\epsilon_0\Lambda} \\ &= \frac{2}{\tau_0}\mathcal{C}(\overline{s})(\overline{s} - s_0 m_0 - sm). \end{aligned} \tag{5.6}$$

Because s_{ij} is independent of position, the tensor equation of motion for the stress (Eq. (2.5)) can be integrated in y over the interval $[y = -L,\ y = +L]$. This results in simplified equations for s and s_0:

$$\dot{s} = \frac{\mu}{s_y}\left(\frac{V_0}{L} - \frac{2\epsilon_0}{\tau_0}\mathcal{C}(\overline{s})(\frac{s}{\overline{s}} - m)\overline{\Lambda}\right) - s_0\frac{V_0}{L}, \tag{5.7}$$

$$\dot{s_0} = -2\frac{\mu}{s_y}\left(\frac{2\epsilon_0}{\tau_0}\mathcal{C}(\overline{s})(\frac{s_0}{\overline{s}} - m_0)\overline{\Lambda}\right) + s\frac{V_0}{L}, \tag{5.8}$$

where $\overline{(\cdot)}$ denotes an average over a field in the y-direction. For example, $\overline{\Lambda}$ is:

$$\overline{\Lambda} = \frac{1}{2L}\int_{-L}^{L}\Lambda(y)dy. \tag{5.9}$$

and $\overline{D_{xy}^{total}} = V_0/(2L)$. Eq. (2.10) can be simplified to equations for m and m_0 as follows:

$$\dot{m} + m_0\dot{\gamma} = -\Gamma m\frac{e^{-1/\chi}}{\Lambda} + \frac{2}{\tau_0}\mathcal{C}(\overline{s})(\frac{s}{\overline{s}} - m); \tag{5.10}$$

$$\dot{m_0} - m\dot{\gamma} = -\Gamma m_0\frac{e^{-1/\chi}}{\Lambda} + \frac{2}{\tau_0}\mathcal{C}(\overline{s})(\frac{s_0}{\overline{s}} - m_0). \tag{5.11}$$

In slowly sheared experiments and simulations, the strain rate $\dot{\gamma}$ is always much smaller than the inherent attempt frequency $1/\tau_0$. Therefore the complicated rotation terms, $m_0\dot{\gamma}$ and $m\dot{\gamma}$, are very small and can be neglected. We rewrite the equations of motion so that times are in units of the inverse average strain rate, $1/\overline{\dot{\gamma}} = L/V_0$, and lengths are in units of L. Note that stresses are already in units of the yield stress s_y.

The resulting system of equations is given by:

$$\dot{s} = \mu^* \left(1 - \frac{2\epsilon_0}{q_0}\mathcal{C}(\overline{s}) \left(\frac{s}{\overline{s}} - m\right) \overline{\Lambda}\right) - s_0; \tag{5.12}$$

$$\dot{s_0} = -\mu^* \left(\frac{2\epsilon_0}{q_0}\mathcal{C}(\overline{s}) \left(\frac{s_0}{\overline{s}} - m_0\right) \overline{\Lambda}\right) + s; \tag{5.13}$$

$$\dot{m} = \left(-\Gamma m \frac{e^{-1/\chi}}{\Lambda} + \frac{2}{q_0}\mathcal{C}(\overline{s})(\frac{s}{\overline{s}} - m)\right); \tag{5.14}$$

$$\dot{m_0} = \left(-\Gamma m_0 \frac{e^{-1/\chi}}{\Lambda} + \frac{2}{q_0}\mathcal{C}(\overline{s})(\frac{s_0}{\overline{s}} - m_0)\right); \tag{5.15}$$

$$\dot{\Lambda} = \Gamma \left(e^{-1/\chi} - \Lambda\right); \tag{5.16}$$

$$\dot{\chi} = \frac{1}{c_0}\Gamma\epsilon_0\Lambda \left(\chi_0 - \chi\right) + D_\chi \frac{\partial^2 \chi}{\partial y^2}, \tag{5.17}$$

where

$$\Gamma = \frac{2}{q_0}\mathcal{C}(\overline{s})(\overline{s} - s_0 m_0 - sm). \tag{5.18}$$

As noted in [50] the density of STZs, $\epsilon_0\Lambda$, is necessarily small. Eqs. (5.12), (5.13) and (5.17) each contain this factor in their numerators and they equilibrate very slowly compared to m, m_0 and Λ, which are governed by Eqs. (5.14), (5.15) and (5.16), respectively. Therefore we replace Λ, m and m_0 by their steady state values:

$$\Lambda = \Lambda_{ss}(\chi) = e^{-1/\chi}; \tag{5.19}$$

$$m = m(s, s_0) = \begin{cases} s/\overline{s}, & \overline{s} \leq 1, \\ s/\overline{s}^2, & \overline{s} > 1, \end{cases} \tag{5.20}$$

$$m_0 = m_0(s, s_0) = \begin{cases} s_0/\overline{s}, & \overline{s} \leq 1, \\ s_0/\overline{s}^2, & \overline{s} > 1. \end{cases} \tag{5.21}$$

Below the yield stress the solid deforms only elastically because all the existing STZs are already flipped in the direction of stress. Three simple partial differential equations remain:

$$\dot{s} = \mu^* \left(1 - \frac{2\epsilon_0}{q_0}\mathcal{C}(s) \left(\frac{s}{\overline{s}} - m\right) \overline{\Lambda}\right) - s_0, \tag{5.22}$$

$$\dot{s_0} = -\mu^* \frac{2\epsilon_0}{q_0}\mathcal{C}(s) \left(\frac{s_0}{\overline{s}} - m_0\right) \overline{\Lambda} + s, \tag{5.23}$$

$$\dot{\chi} = \frac{2\epsilon_0 \mathcal{C}(s)}{c_0 q_0} \left(\overline{s} - s_0 m_0 - sm\right) e^{-1/\chi}(\chi_0 - \chi) + D_\chi^* \frac{\partial^2 \chi}{\partial y^2}. \tag{5.24}$$

This set of equations has several dimensionless parameters. The volume (area in 2D) fraction of the strip covered by STZs or the probability of finding an STZ at a given point in the strip is $\epsilon_0\Lambda$. Λ is the probability that a particle participates in an STZ. Assuming that STZs have a characteristic size of a few particle diameters, $\epsilon_0 = \lambda n_\infty$ is the characteristic number of particles in an STZ. The parameter $\mu^* = \mu/s_y$ is the ratio of average material stiffness to STZ stiffness, and corresponds to the slope of the linear elastic portion of a stress-strain curve. The specific heat in units of the STZ formation energy, c_0, determines how fast the effective temperature changes compared to plastic rearrangements. The parameter $q_0 = \tau_0 V_0/L$ is the ratio of the two physical timescales in the system, the inverse STZ attempt frequency and the average inverse strain rate. Finally, χ_0 is the steady state effective temperature in units of the STZ formation energy divided by the Boltzmann constant.

The effective temperature diffusivity is the remaining parameter and requires some discussion. The dimensionless parameter D^*_χ in Eq. (3.4) can be written as follows:

$$D^*_\chi = (D_\chi/c_0)(L/V_0)(1/L^2), \tag{5.25}$$

where $D_\chi = a^2/\tau_D$. As discussed in the introduction, the diffusivity time scale should be the inverse strain rate, $\tau_D = 1/\dot{\gamma}$. We have investigated solutions (not shown here) to the STZ equations with an effective temperature diffusivity D^*_χ (a) independent of strain rate and (b) proportional to the local strain rate, which varies as a function of position. While there are subtle differences between the solutions in each case, broad features of the effective temperature solutions such as the maximum value and the functional shape are the same in both cases. A constant effective temperature diffusivity results in simpler dynamic equations, and we will use this convention for the remainder of the chapter.

5.3 Numerical integration of the STZ equations

In this section we show that numerical integration of the simple, macroscopic STZ equations (Eqs. (5.22-5.24)) qualitatively and quantitatively match molecular dynamics simulations of a Lennard-Jones glass by Shi, Katz, Li and Falk [40]. The simulations were performed in a simple shear geometry with periodic Lees-Edwards boundary conditions. The parameter range for the simulations was chosen to ensure that the glass exhibits strain localization, and stress-strain curves were computed for a variety of quenches and strain rates.

The investigators calculated the potential energy per atom and strain rate as a function of position for several different strains. They used the data to investigate

the hypothesis (found in the STZ model and other models) that the local plastic strain rate is related to an effective temperature or free volume. In [40], they show that a value for the steady state effective temperature,χ_0, can be rigorously extracted from a thorough analysis of the simulation data. In this chapter we numerically integrate the STZ equations in the same infinite strip geometry, and compare the results to simulation data. Building on the work of Shi, *et al.*, we choose parameters for the STZ theory to match the conditions found in the simulations.

In experiments and simulations, boundary conditions on the particles at the top and bottom of the strip impact the dynamics and may influence strain localization. Shi, *et al.* chose periodic boundary conditions for their simulations, while other investigators [41] have chosen rigid rough walls. While both sets of simulations exhibit strain localization, features of the localization process are different in each case and it is unclear whether the differences are due to the dissimilar boundary conditions or other features of the simulations.

Similarly, the STZ equations require boundary conditions for the effective temperature field at the top and bottom of the strip. We have studied the STZ equations with both periodic and no conduction ($\partial\chi/\partial y = 0$) boundary conditions and found qualitatively and quantitatively similar results. For the remainder of this chapter we will describe solutions to the STZ equations with periodic boundary conditions for comparison to the results of Shi, *et al.*

5.3.1 Matching parameter values to simulations

The first task is to choose values for the parameters in STZ theory consistent with those in the simulations by Shi, *et al.* The simulation data for the stress-strain curves at a particular strain rate can be fit by a range of values for χ_0, q_0, and the specific heat c_0. However, a much narrower range of parameters fit both the stress-strain data and the data for the strain-rate as a function of position.

We estimate an order of magnitude for each parameter motivated by physical considerations. Table 5.1 lists the specific parameter values used in the numerical integration. The steady state effective temperature χ_0 determines the steady state density of STZs: $\Lambda_\infty = \exp[-1/\chi_0]$. To ensure that STZs are rare, χ_0 should be around 0.1. Shi, *et al.*, extracted $\chi_0 = 0.15$ from the data using the hypothesis that the strain rate is proportional to $e^{-1/\chi}$, and we will use this value here. The parameter ϵ_0 is the characteristic number of particles in a shear transformation zone. Studies of non-affine particle motion in a 2D Lennard-Jones glass [47] and a 2D system of hard spheres [77] suggest that an STZ has a radius of a few particle diameters. This implies that the number of particles in an STZ is of order 10

Parameter	Value
χ_0	0.15
ϵ_0	10
c_0	1
D^*_χ	0.01
μ^*	70
q_0	1×10^{-6}
χ_{ini}	$0.068, 0.069, 0.074$

Table 5.1: List of parameter values used in the numerical integration of the STZ model, Eqs. (5.26,5.27).

for 2D simulations. Because c_0 is a dimensionless constant and does not depend on other scales in the problem, c_0 should be of order unity. The parameter μ^* is the slope of the linear elastic part of the stress-strain curve plotted in units of the yield stress. It corresponds to the ratio of the elastic material stiffness to the STZ stiffness, and should be much greater than one. In the MD simulations, μ^* is about 70.

Eqs. (5.22-5.24) can be further simplified because μ^* is large. For $\overline{s} \leq 1$, the rate of plastic deformation is zero and and Eq. (5.22) indicates that the stress increases proportionally to μ^*. During this same time, Eq. (5.23) requires that s_0 increases proportionally to s, which is less than unity. During the linear elastic response, the off-diagonal component of the stress is order μ^* larger than the on-diagonal stress, which matches our physical intuition for simple shear. Numerical integration of Eqs. (5.22-5.24) confirms that s_0 remains about two orders of magnitude smaller than s. We therefore use the approximation $\overline{s} = s$ and $s_0 = 0$. This results in two simple equations for the STZ dynamics:

$$\dot{s} = \mu^* \left(1 - \frac{2\epsilon_0}{q_0} \mathcal{C}(s) \left(1 - m(s)\right) \overline{\Lambda}\right), \tag{5.26}$$

$$\dot{\chi} = \frac{2\epsilon_0 \mathcal{C}(s)\, s}{c_0 q_0} \left(1 - m(s)\right) e^{-1/\chi} (\chi_0 - \chi) + D^*_\chi \frac{\partial^2 \chi}{\partial y^2}. \tag{5.27}$$

The remaining parameters are D^*_χ and q_0. As mentioned in the previous section, we postulate that the effective temperature diffusion D^*_χ is a constant independent of strain rate which we determine from the long-time diffusion of the shear band in the simulations. We find that $D^*_\chi \simeq 0.01$ matches the simulation data.

The Lennard-Jones glass has a natural time scale $t_0 = \sigma_{SL}\sqrt{M/\epsilon_{SL}}$, where

σ_{SL} is the equilibrium distance between small and large particles, ϵ_{SL} is the depth of the potential energy well between the two species and M is the mass. The average strain rate in the simulations varies from $2 \times 10^{-5} t_0^{-1}$ to $5 \times 10^{-4} t_0^{-1}$.

If we assume that the STZ attempt frequency τ_0 is approximately t_0, then $q_0 \simeq 2 \times 10^{-5}$ and the resulting numerical solutions to the STZ equations never exhibit localization. This is inconsistent with simulation data. In order to match the localization seen in the simulations, we are required to choose a value for τ_0 that is an order of magnitude smaller than t_0. We find that $q_0 \simeq 1 \times 10^{-6}$ results in STZ solutions where strain rate matches results from the MD simulations. We will discuss the implications of this in Section 5.4.4.

Initial conditions for s and χ must also be determined. Because the stress is constant as a function of position and the simulations begin in an unstressed state, $s(t = 0) = 0$. The initial effective temperature $\chi(y, t = 0)$ is a *function* of position with many more degrees of freedom. In the MD simulations, the initial potential energy is nearly constant as a function of position with fluctuations about the mean. Therefore, the initial effective temperature is also nearly constant with small amplitude perturbations about its mean. We expect fluctuations in the effective temperature to occur on the scale of a few particle radii in dimensionless units. The simulation box of Shi, *et al.* has a width of about 300 particle radii, so perturbations which span five particle radii have a nondimensionalized wavelength $w = 1/60$.

The amplitude of the initial perturbations, $\delta\chi_{ini}$, can be approximated empirically from the initial potential energy per atom as a function of position, shown in Figure 5.2(b). The potential energy at 0% strain exhibits small perturbations with standard deviation $\sim 0.02\,\epsilon_{SL}$ about a mean value of $-2.51\,\epsilon_{SL}$, while the system reaches a maximum of $-2.42\,\epsilon_{SL}$ in the shear band at larger strains. Assuming the maximum potential energy in the band corresponds to χ_0 and the initial mean potential energy per atom corresponds to χ_{ini}, the amplitude of initial perturbations is about $\delta\chi = 0.02$. This is consistent with a thermodynamic calculation [78] for the magnitude of fluctuations about the effective temperature, $< (\delta\chi)^2 >= \chi^2/(c_0) \simeq 0.01$.

We use two different methods for generating an initial effective temperature distribution for the STZ equations. The first is to use a deterministic function with a single peak that serves as a nucleation point for shear bands: $\chi(y, t = 0) = \chi_{ini} + \delta\chi_{ini}\,\mathrm{sech}(y/w)$. The second method generates a random number from a uniform distribution, and smooths those values using a simple moving average of width w. The resulting function is normalized so that its standard deviation from the mean value is $\delta\chi_{ini}$, and the mean is χ_{ini}.

The first type of initial condition is less physically realistic but more tractable

because it generates at most a single shear band. The second type of initial condition can generate solutions with varying numbers of shear bands, depending on the system parameters. We find that for the parameter range which best fits the simulation data, the STZ equations with random initial conditions generate a solution with a single shear band, which agrees with observations from the simulations and further validates our choice of STZ parameters.

5.3.2 Comparison of macroscopic stress-strain behavior

We numerically integrate Eqs. (5.26, 5.27) with parameters values discussed above, for many different values of χ_{ini}. Figure 5.1(a) is a plot of stress vs. strain for three different initial preparations of a material starting from rest and driven in simple shear. Dashed lines correspond to MD simulation data from samples permitted to relax for three different amounts of time before being sheared. Solid lines are numerical solutions to the simplified STZ model (Eqs. (5.26) and (5.27)) for three different average initial effective temperatures.

All of the samples (for both the MD simulations and the STZ solutions) exhibit strain localization, which influences the stress-strain curves shown in Figure 5.1. We will discuss how localization affects the macroscopic stress-strain curves later in this section, and analyze the localization process in Section 5.4.

The STZ solutions shown differ only in the initial mean value for the effective temperature, χ_{ini}, and are the best least-squares fit as a function of χ_{ini} for each quench. Note that general features of the stress-strain curves match: there is a linear elastic segment, followed by a decrease in the stress slope as the material begins to deform plastically, a peak at about 2 % strain, and stress relaxation as the material softens and stored elastic energy is released.

The glass in the MD simulations behaves differently depending on how long the system was quenched before shearing, and the STZ model captures this behavior. A longer quench results in a more ordered solid and corresponds to a lower initial effective temperature. Numerical integration of the STZ equations indicate that lower initial effective temperatures generically result in higher peak stresses. This matches both the MD simulations and physical intuition: a more ordered solid takes more time and stress to plastically deform because more STZs must be created to permit the deformation.

In Figure 5.1(b) the slope (μ^*) of the linear elastic segment of the most disordered glass (Quench III) is smaller than in the samples that were quenched for longer times before shearing. A linear fit to these data shows that $\mu^* \simeq 70$ for Quenches I and II, while $\mu^* \simeq 60$ for Quench III.

We model the material surrounding the STZs as an elastic medium, and the

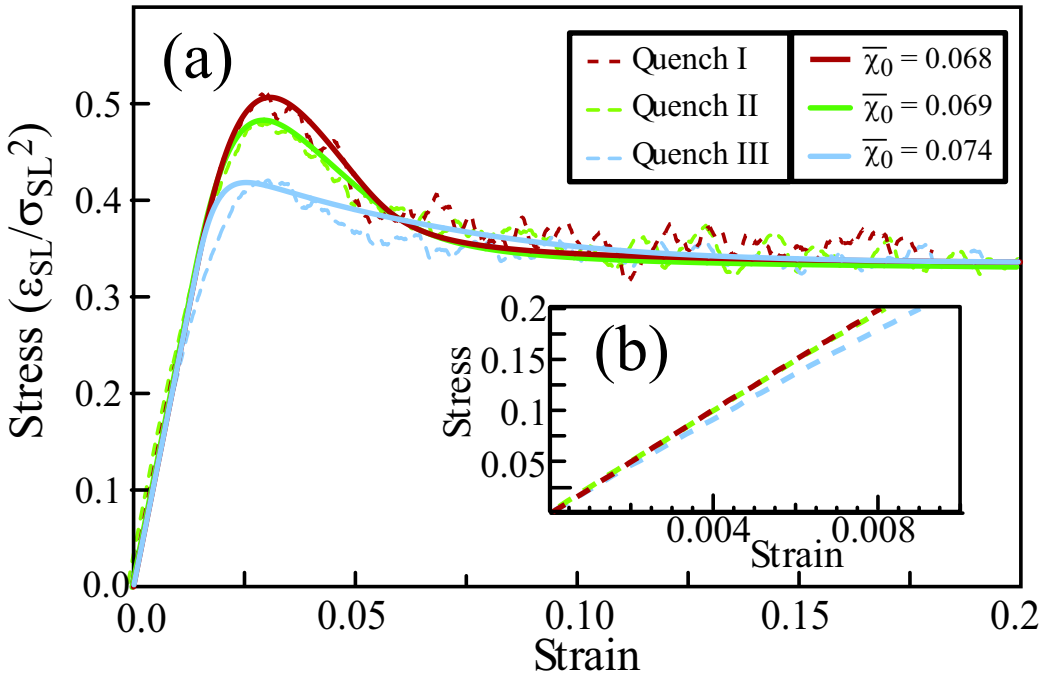

Figure 5.1: (a) Simulation data and STZ theory for stress vs. strain from Ref. [40]. Dashed lines are simulation data for three different initial preparations. The uppermost (red) curve corresponds to a sample quenched for the longest time (100,000 t_0) before the sample was sheared and has an initial average potential energy per atom of -2.507. The middle (green) and lowermost (light blue) curves were quenched for 50,000 t_0 and 10,000 t_0 respectively, and have initial potential energy/atom of -2.497 and -2.477. The solid lines correspond to STZ solutions with values for the initial effective temperature (χ_{ini}) that best fit the simulation data: 0.062, 0.063 and 0.067, respectively. (b) Linear elastic regime of the simulation data for the three different quenches.

parameter μ^* is the ratio of the elastic material stiffness to the STZ stiffness. We assume that the STZ stiffness is constant for different sample preparations. Therefore a variation in μ^* between samples indicates that the surrounding elastic medium is less stiff in the more disordered material. This is consistent with the work of Maloney and Lemaître, who have shown that the elastic shear modulus is smaller in more disordered materials due to non-affine particle motion [75].

Although we could better fit the MD simulation data by allowing μ^* to vary between samples, in order to limit the adjustable parameters in the theory we fix $\mu^* = 70$ for all samples. As expected, Figure 5.1(a) shows that the numerical STZ

results closely match the simulation data for Quenches I and II, while the best STZ fit systematically deviates from the simulation data for Quench III.

5.3.3 Comparison of strain localization inside the material

One feature of the infinite strip geometry is that it permits the system to achieve very large strains without fracturing, so that both theory and simulation can track system evolution over very large strains. The STZ solutions not only match the short-time macroscopic stress-strain behavior, but also match the long-time dynamics of strain localization within the strip.

Figure 5.2 shows the strain rate as a function of position for various values of the strain (corresponding to different times) for (a) the MD simulations and (b) STZ theory. This figure also shows (c) the simulation potential energy per atom and (d) theoretical effective temperature as functions of position. The simulation data is averaged over increments of 100 % strain, while the STZ model is evaluated for specific values of the strain corresponding to the midpoint of each binning range.

Localization is evident in both the simulation data and numerical STZ solutions. The strain rate as a function of position inside the material exhibits very slow relaxation over 800 % strain. This is in contrast to the much faster stress dynamics that attain steady state in less than 10% strain, as seen in Fig. 5.1. In the numerical STZ solutions, the effective temperature attains a maximum in the same physical location within the strip as the strain rate. This is remarkably similar to the dynamics of the potential energy per atom in the simulations, and completely consistent with the assumption that χ is proportional to the potential energy. Shi, *et al.* were the first to systematically check this hypothesis and they used it to extract various STZ parameters, such as χ_0 [40].

5.3.4 Implications for constitutive laws

Strain localization has a large effect on the short-time macroscopic stress-strain behavior of the system. For example, Fig. 5.3 (a) shows two possible initial conditions for the initial effective temperature field. The average initial effective temperature is the same in both cases. One initial condition for the effective temperature varies with position while the other is constant as a function of position. Figure 5.3 (b) shows the resulting stress-strain curves for each case. When χ_{ini} varies as a function of position, the system localizes and the resulting stress-strain curve does not reach as high a peak value, because the material releases elastic energy more quickly. The steady state stress is the same in each

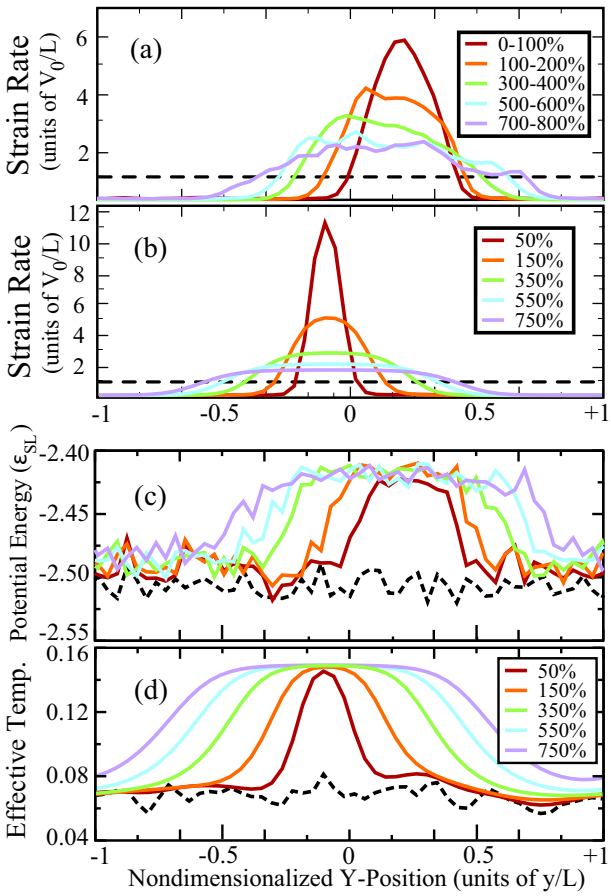

Figure 5.2: (a) Simulation data for strain rate vs. position at various strains from Ref. [40]. Strain rates are averaged over bins of 100 % strain. The dashed line corresponds to the imposed average strain rate. (b) Theoretical STZ solutions for strain rate vs. position at various strains. Strain rate is evaluated for specific values of the strain corresponding to the midpoint of each binning range for simulation data. The dashed line is the average strain rate. (c) Simulation data for potential energy as a function of position [40] and (d) Theoretical solution for the effective temperature as a function of position. The dashed lines correspond to the initial values of the potential energy per atom and effective temperature.

case. This is just one example of the general sensitivity of macroscopic state variables to microscopic details.

The fact that localization influences the macroscopic stress-strain curves has important implications for constitutive laws. Constitutive laws provide a relation-

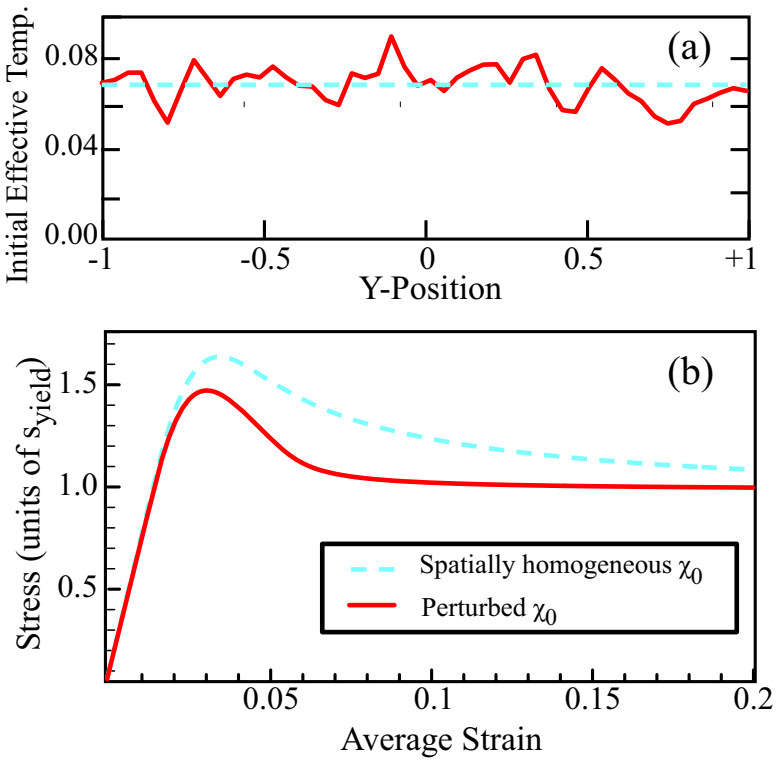

Figure 5.3: Macroscopic stress-strain curves are sensitive to localization. **(a)** The initial effective temperature distribution is either homogeneous, illustrated by a dashed (blue) line or slightly perturbed, illustrated by a solid (red) line, though the average value χ_{ini} is the same in both cases. **(b)** The stress vs. strain predictions are significantly different for these two different initial conditions. The perturbed system localizes, as shown in Figure 5.2(d), and this changes the resulting macroscopic behavior.

ship between the strain rate, stress, and a set of state variables that characterize the internal structure of a material interface. They describe how features of microscopic particle dynamics determine macroscopic frictional properties, and are used extensively in models of earthquakes [1, 2], granular flows [79], and machine control [80]. Several investigators have adapted STZ theory to describe the macroscopic behavior of lubricated surfaces [54], dense granular flows [77], and earthquake faults [9], but all of these formulations assume that the STZ variables do not vary as a function of position across the sheared interface. Deriving new constitutive laws based on localized dynamics is beyond the scope of this chapter. However, our analysis shows that localization is possible in STZ models and

that the corresponding constitutive behavior is altered. Therefore it is important for localization to be included in modeling efforts, and this will be a direction of future research.

5.4 Stability analysis

Continuum models for amorphous solids create a framework for understanding the instability that leads to localization in amorphous materials. In the previous section we showed that STZ theory with effective temperature exhibits strain localization. In the following subsections we investigate the stability properties of the dynamical system given by Eqs. (5.26) and (5.27).

5.4.1 Steady state linear stability

The first step in understanding how the simplified STZ model given by Eqs. (5.26) and (5.27) responds to perturbations is to perform a linear stability analysis around the steady state solution. Setting $\dot{s} = 0$ in Eq. (5.26), results in the following equation for the steady state flow stress s_f:

$$1 = \frac{2\epsilon_0}{q_0}\mathcal{C}(s_f)(1 - 1/s_f)\exp[-1/\chi_0]. \tag{5.28}$$

For the values of q_0 and χ_0 in Table 5.1, $s_f = 1.005$ — the yield stress is nearly equal to the steady state stress. The steady state solution for χ is spatially homogeneous: $\chi(y) = \chi_0$.

We now show that the perturbed system, $s = s_f + \widetilde{s}, \chi = \chi_0 + \delta\chi(y)$, is linearly stable. To simplify notation, we define the functions f and g:

$$\begin{aligned} f(s,\chi) &\equiv \frac{\partial s}{\partial t} \\ &= \mu^*\left(1 - 2\frac{\epsilon_0\mathcal{C}(s)}{q_0}(1-m)\int_{-L}^{L}\frac{e^{-1/\chi}}{2L}dy\right); \qquad (5.29) \\ g(s,\chi) &= \frac{\partial \chi}{\partial t} \\ &= \frac{2s\epsilon_0\mathcal{C}(s)}{q_0 c_0}(1-m)e^{-1/\chi}\left(\chi_0 - \chi\right) + \mathcal{D}_\chi\frac{\partial^2\chi}{\partial y^2}. \qquad (5.30) \end{aligned}$$

The perturbation to χ can be written as a sum of normal modes that satisfy the

boundary conditions:

$$\delta\chi(y) = \sum_{k=-\infty}^{\infty} \delta\chi_k e^{iky}, \qquad k = \frac{n\pi}{L}. \tag{5.31}$$

The operator $\partial^2/\partial y^2$ is diagonalized in the basis of normal modes and therefore the dynamics of each normal mode are decoupled. In the limit of infinitesimal perturbations, terms of order $\delta\chi^2$ and $\widetilde{s}^2$ can be neglected. This results in the following linear equations for each mode:

$$\dot{\widetilde{s}} = \frac{\partial f}{\partial s}(s_f, \chi_0)\widetilde{s} + \frac{\partial f}{\partial s}(s_f, \chi_0)\delta\chi_k, \tag{5.32}$$

$$\dot{\delta\chi_k} = \frac{\partial g}{\partial s}(s_f, \chi_0)\widetilde{s} + \frac{\partial g}{\partial \chi}(s_f, \chi_0)\delta\chi_k. \tag{5.33}$$

The second term in Eq. (5.32) requires some additional explanation, because the operator $\partial f/\partial s$ includes an integral. The action of this operator on a normal mode $\delta\chi_k e^{iky}$ is given by:

$$\frac{\partial f}{\partial \chi}\delta\chi_k e^{iky} = \mathcal{W}(s_f, \chi_0)\,\frac{1}{2L}\int_{-L}^{+L} \delta\chi_k e^{in\pi y/L} dy \tag{5.34}$$

$$= \begin{cases} 0, & k \neq 0, \\ \mathcal{W}(s_f, \chi_0), & k = 0, \end{cases} \tag{5.35}$$

where

$$\mathcal{W}(s_f, \chi_0) = -\frac{2e^{-1/\chi_0}\epsilon_0\mu^*\left(1 - \frac{1}{s_f}\right)\mathcal{C}(s_f)}{q_0\chi_0^2}\delta\chi_k. \tag{5.36}$$

This analysis reveals a particularly interesting and important feature of the STZ model dynamics which we will return to in the next section. There is a fundamental difference between the dynamics of spatially homogeneous perturbations to χ and perturbations with zero mean. Because the stress is always spatially homogeneous, to linear order the stress dynamics depend *only on the average value of* χ and are completely unaffected by zero mean perturbations to χ.

In order to determine the linear stability of each mode, we calculate the two eigenvalues (as a function of k) for the steady state Jacobian $J^{ss}(k)$, which is the two-by-two matrix given by:

$$\begin{bmatrix} \dot{\widetilde{s}} \\ \dot{\delta\chi_k} \end{bmatrix} \equiv J^{ss}(k) \begin{bmatrix} \widetilde{s} \\ \delta\chi_k \end{bmatrix} \tag{5.37}$$

$$\equiv \begin{bmatrix} J_{11}(k) & J_{12}(k) \\ J_{21}(k) & J_{22}(k) \end{bmatrix} \begin{bmatrix} \widetilde{s} \\ \delta\chi_k \end{bmatrix}. \tag{5.38}$$

The two diagonal terms can be written:

$$J_{11} = \frac{2e^{-1/\chi_0}\epsilon_0\mu^*}{q_0}\left(\left(\frac{1}{s_f}-1\right)\mathcal{C}'(s_f) - \frac{\mathcal{C}(s_f)}{s^2}\right)\Theta(s_f-1), \tag{5.39}$$

$$J_{22} = \frac{2\epsilon_0 s_f e^{-1/\chi_0}}{c_0 q_0}\left(-\mathcal{C}(s_f)(1-\frac{1}{s_f})\right)\Theta(s_f-1) - D^*_\chi k^2, \tag{5.40}$$

where Θ is the unit step function.

If either of the two eigenvalues of J^{ss} has a positive real part for a particular value of k, then that mode grows exponentially and the system is unstable with respect to perturbations with that wavenumber k.

For $k \neq 0$, $J_{12}(k)$ is zero and the matrix is lower triangular, so the eigenvalues are simply J_{11} and J_{22}. Because $\mathcal{C}(s)$ is monotonically increasing and positive for $s > 0$, both eigenvalues are negative for all values of $k \neq 0$. The eigenvalues calculated for $k = 0$ are negative also. Therefore, the STZ model is stable with respect to perturbations in steady state. An analysis by Foglia of the operator J_{22} for an STZ model that included thermal effects resulted in the same conclusion [81].

5.4.2 Time-varying stability analysis

In simulations and numerical integration of the STZ equations, localization of strain first occurs before the stress reaches a steady state. Transient localization is also seen in numerical simulations of Spaepen's free volume model by Huang et al. [82], and in the Johnson-Segalman model for complex fluids [83]. This motivates us to study the stability of transient STZ dynamics.

The field χ in the STZ model given by Eqs. (5.26, 5.27) can be rewritten as the sum of normal modes. As discussed in Section 5.4.1, for small perturbations with wavenumber k, the governing equations for the $k = 0$ mode are fundamentally different from all other modes. This motivates us to write the field χ at each point in time as the sum of a spatially homogeneous field $\overline{\chi}(t)$ and zero-mean perturbations:

$$\chi(y,t) = \overline{\chi}(t) + \sum_{k\neq 0}\delta\chi_k(t)e^{iky}, \quad k = \frac{n\pi}{L}. \tag{5.41}$$

To analyze the transient stability of this system, we permit the $k = 0$ mode, $\overline{\chi}(t)$, to be arbitrarily large but constrain the zero mean perturbations, $\delta\chi_k$, to be small. This is slightly different from the normal mode analysis in Section 5.4.1 where both $k = 0$ and $k \neq 0$ modes were small. Substituting Eq. (5.41) into Eq. (5.29) and neglecting the second order terms in $\delta\chi_k$ results in the following

equation:

$$\begin{aligned}
\dot{s} &= f(s, \overline{\chi} + \sum_{k\neq 0} \delta\chi_k(t) e^{iky}) \\
&= \mu^* \left(1 - 2\frac{\epsilon_0}{q_0}\mathcal{C}(s)(1-m_0)e^{-1/\overline{\chi}} \times \left(1 + \frac{1}{\overline{\chi}^2}\sum_{k\neq 0}\frac{1}{2L}\int_{-L}^{L}\delta\chi_k(t)e^{iky}dy\right)\right) \\
&= \mu^* \left(1 - 2\frac{\epsilon_0}{q_0}\mathcal{C}(s)(1-m_0)e^{-1/\overline{\chi}}\right) \\
&= f(s, \overline{\chi}).
\end{aligned} \tag{5.42}$$

This indicates that to linear order, zero-mean perturbations to χ do not affect the stress. Substituting Eq. (5.41) into Eq. (5.30) results in the following linearized equation for each perturbation mode:

$$\dot{\delta\chi_k}(t) = \frac{\partial g}{\partial \chi}(s(t), \overline{\chi}(t), k)\ \ \delta\chi_k. \tag{5.43}$$

This is a linearized equation for the dynamics of small perturbations about a spatially homogeneous, time varying solution. Called a "frozen-time" analysis, it is valid whenever the perturbations grow slowly compared to the underlying trajectory, even if the magnitude of $\overline{\chi}(t)$ is large.

Physically, this corresponds to the following experiment: the system is started from a spatially homogeneous initial condition and the system remains spatially homogeneous until a small, zero-mean perturbation in introduced at time τ. The time-varying linear operator $\frac{\partial g}{\partial \chi}(s(\tau), \overline{\chi}(\tau))$ describes the growth or decay of these small perturbations. The functions $s(t), \overline{\chi}(t)$ are the solutions to the STZ equations with spatially homogeneous initial conditions $s(t=0) = s_0$, $\chi(y, t=0) = \chi_{ini}$. If the initial conditions are homogeneous, the STZ equations are simply ordinary differential equations, which are much easier to solve than the inhomogeneous equations.

This description for the linearized start-up dynamics is relevant to many experiments and simulations. For example, the simulations by Shi, *et al.* begin from a state where the initial potential energy, which corresponds to the initial effective temperature, is roughly constant as a function of position. This corresponds to a spatially homogeneous initial condition for the effective temperature, $\chi(t=0, y) \equiv \chi_{ini} = c$. Additionally, the MD samples are started from an unstressed state, which corresponds to $s_0 = 0$. The potential energy does vary slightly as a function of position, which corresponds to small, zero-mean perturbations to χ introduced at time $t = 0$.

We define the stability exponent $\omega_c(k,t)$ in the following manner. Let $s_c(t), \overline{\chi}_c(t)$ be the unique spatially homogeneous solution to the STZ equations starting from the initial condition $s_0 = 0, \chi_{ini} = c$. Then the exponent at time τ is defined as:

$$\begin{aligned}\omega_c(k,\tau) &= \frac{\partial g}{\partial \chi}(s_c(\tau), \overline{\chi}_c(\tau), k) \\ &= \frac{2e^{-1/\overline{\chi}_c}\epsilon_0 s_c}{c_0 q_0}\left(\left(\frac{\chi_0 - \overline{\chi}_c}{\overline{\chi}_c^2} - 1\right)\mathcal{C}(s_c)(1 - \frac{1}{s_c})\right) \\ &\quad \times \Theta(s_c - 1) - D_\chi^* k^2, \end{aligned} \tag{5.44}$$

where the functions $s_c(t)$ and $\overline{\chi}_c(t)$ are understood to be evaluated at $t = \tau$ and $\Theta(s)$ is the unit step function.

This exponent describes the rate of growth or decay of a small perturbation with wavenumber k introduced at time τ to the solution $s_c(t), \overline{\chi}_c(t)$. If the real part of $\omega_c(k,t)$ is greater than zero then the perturbations grow exponentially and the system is unstable, and otherwise the system is stable with respect to perturbations.

Note that $\omega_c(k,t)$ contains a single term that depends on the wavenumber k — this term is proportional to $-k^2$ and corresponds to the diffusion of effective temperature. Because diffusion can only act to stabilize perturbations to χ, the most dangerous mode corresponds to $k = \pm\pi/L$.

A plot of $\omega_c(k,t)$ for $c = \chi_{ini} = 0.6$ and $k = \pi/L$ is shown in Fig. 5.4. The system is marginally stable with respect to perturbations during the linear elastic response of the system, highly unstable at intermediate times, and becomes stable with respect to perturbations as $\overline{\chi}(t)$ approaches χ_0. A lower bound for stable χ is determined from Eq. (5.44) as follows. Because the diffusion term is always negative, an upper bound on the stability exponent for all values of k is given by:

$$\omega_c(k,t) < H(s)e^{-1/\overline{\chi}_c(t)}\left(\frac{\chi_0 - \overline{\chi}_c(t)}{\overline{\chi}_c^2(t) - 1}\right) \tag{5.45}$$

where $H(s)$ is zero for $s \leq 1$ and positive for $s > 1$. Therefore the stability exponent is less than zero when $\overline{\chi}(t)$ satisfies the following inequality:

$$0 > \frac{\chi_0 - \overline{\chi}(t)}{\overline{\chi}(t)^2} - 1, \tag{5.46}$$

which defines (5.47)

$$\overline{\chi}(t) > \frac{1}{2}\left(-1 + \sqrt{1 + 4\chi_0}\right) \equiv \chi_{\text{crit}}. \tag{5.48}$$

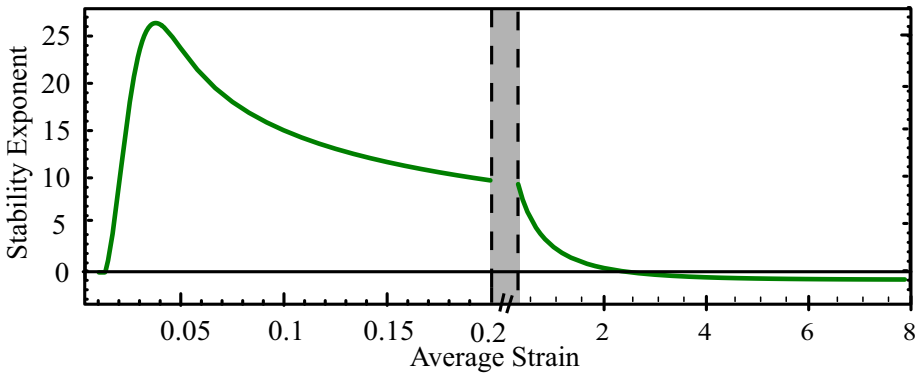

Figure 5.4: The stability exponent $\omega_c(k,t)$ with $c = 0.06$ and $k = \pi/L$ as a function of total strain for spatial perturbations to the effective temperature in the limit $k \to 0$. The system is linearly unstable with respect to spatial perturbations to χ when $\omega_c(k,t)$ is greater than zero, and stable otherwise. The figure contains two scales for the average strain in order to simultaneously illustrate both the short- and long-time behavior.

This analysis indicates if the initial effective temperature is above a critical value, $\chi_{ini} > \chi_{\text{crit}}$, then small amplitude perturbations are stable and the system will not localize. However, if the initial effective temperature is less than this value (plus a diffusive term that depends on the wavenumber), there exists a period of time where small perturbations to the effective temperature will grow. A time-varying stability analysis of thermal STZ equations by Foglia shows that the effective temperature is transiently unstable to perturbations in that context as well [81].

This description of perturbations to a spatially homogeneous, time-varying, "start-up" trajectory is remarkably similar that given by Fielding and Olmsted [83] in a study of shear banding in the Johnson-Segalman model for complex fluids. The stability of the solution to perturbations is simpler to analyze in the STZ formulation than in the complex fluid model because the linearized evolution of perturbations to χ are decoupled from the stress, as shown in Eq. (5.42). This suggests that the mechanism for shear band nucleation in "start-up" flows may be similar in a variety of materials.

5.4.3 Finite amplitude effects and a criterion for localization

While linear stability analysis determines when perturbations grow, by itself it does not provide enough information to determine whether or not the integrated STZ equations exhibit strain localization. Many of the numerical STZ solutions for an unstable initial effective temperature do not localize if the initial perturbations are "too small". For example, numerical integration of the STZ equations with an unstable initial value for the effective temperature $\chi_{ini} = 0.09 < \chi_{\text{crit}} \simeq 0.13$ and a small initial perturbation $\delta\chi_0 = 0.001$, result in a solution that is virtually indistinguishable from a homogeneous system. The purpose of this section is to derive a criterion based only on initial conditions (the mean value of the initial effective temperature χ_{ini} and the amplitude of initial perturbations $\delta\chi_0$) that determines which materials will exhibit long-time strain localization.

At first glance, the fact that a finite perturbation is required to generate localized solutions seems to contradict our assertion that the system is linearly unstable. However, frozen-time linear stability equations are only valid when the underlying trajectory grows slowly compared to the growth of perturbations. In addition, the linear stability analysis gives no information about the long-time behavior of the unstable perturbed/inhomogeneous states. Nonlinear system dynamics can enhance or inhibit localization in the inhomogeneous states. Upon further examination, we recognize that the "finite-amplitude effect" is due to nonlinear dynamics involving the interaction of two dynamical processes: perturbation growth and energy dissipation. Based on this understanding we derive a criterion for which initial conditions result in shear banding.

We first show that rate of energy dissipation as a function of position determines whether perturbed states remain inhomogeneous or become uniform. Our guiding intuition is that perturbations that grow quickly permit most of the energy to be dissipated in the incipient shear band, which enhances localization. Otherwise the energy is dissipated throughout the material, which inhibits localization.

Eq. (5.27) can be rewritten in terms of the rate of plastic work dissipated by the system, Q:

$$\dot{s} = 1 - \frac{\overline{Q}}{s}, \tag{5.49}$$

where $\overline{Q}$ is spatial average of the rate of plastic work $Q(y)$. Q can be resolved into a product of two terms – the rate of plastic work per STZ, $\Gamma(s)$, that depends only on the stress and is spatially invariant, and the density of STZs, $\Lambda(\chi)$, which

depends only on the effective temperature and is a function of position:

$$Q = \frac{2\epsilon_0}{q_0} s\mathcal{C}(s)(1-m)e^{-1/\chi} \equiv \Gamma(s)\Lambda(\chi). \tag{5.50}$$

In steady state the average $\overline{Q} = \Gamma(s)\overline{\Lambda}$ is constrained to be a constant, but the value $Q(y) = \Gamma(s)\exp[-1/\chi(y)]$ is not similarly constrained. This admits the possibility that the plastic work dissipated is very small at some positions and large at others, and this *must* occur for the system to remain localized.

To see this, first note that if the effective temperature is below χ_0, Eq. (3.4) requires that the effective temperature must always increase proportional to $Q(\chi_0 - \chi)$ or diffuse — there is no relaxation towards thermal temperature in this approximation. Therefore, a spatially heterogeneous effective temperature distribution will be *nearly stationary* only if Q is very close to zero whereever $\chi \neq \chi_0$. In other words, strain localization will only persist if the rate of plastic work dissipated outside the shear band is very small.

The rate at which plastic work is dissipated is proportional to $\exp[-1/\chi(y)]$. A rough assumption about the nonlinear, inhomogeneous effective temperature dynamics is that the largest initial perturbation of amplitude $\delta\chi_0$ continues to grow at the rate we derived using linear stability analysis: $\omega(t)\delta\chi(t)$, while the effective temperature in regions outside the incipient shear band grows at the rate of a homogeneous system, $\dot{\overline{\chi}} = g(\overline{\chi}(t), s(t))$. This assumption is consistent with behavior seen in numerical solutions to the STZ equations.

Figure 5.5 shows the behavior of the effective temperature as a function of time for (a) a system that localizes and (b) a system that does not localize, illustrating the two different initial stages. In both plots the upper solid line is the maximum value of $\chi(y)$ inside the shear band, the lower solid line is the minimum value of $\chi(y)$ outside the shear band, and the dashed line is a homogeneous solution with the same mean value, $\overline{\chi}$. In plot (a), the perturbation grows quickly compared to the homogeneous solution for χ, while in (b) the perturbation grows slowly.

We are interested in whether the system dynamics focus energy dissipation inside the shear band or spread energy dissipation evenly throughout the material. Ideally, we would like to compare energy dissipation inside the band (Q_{in}) to energy dissipation outside of the band (Q_{out}) at various times t. However, we only have information about the initial conditions, χ_{ini} and $\delta\chi_0$. Therefore we compare

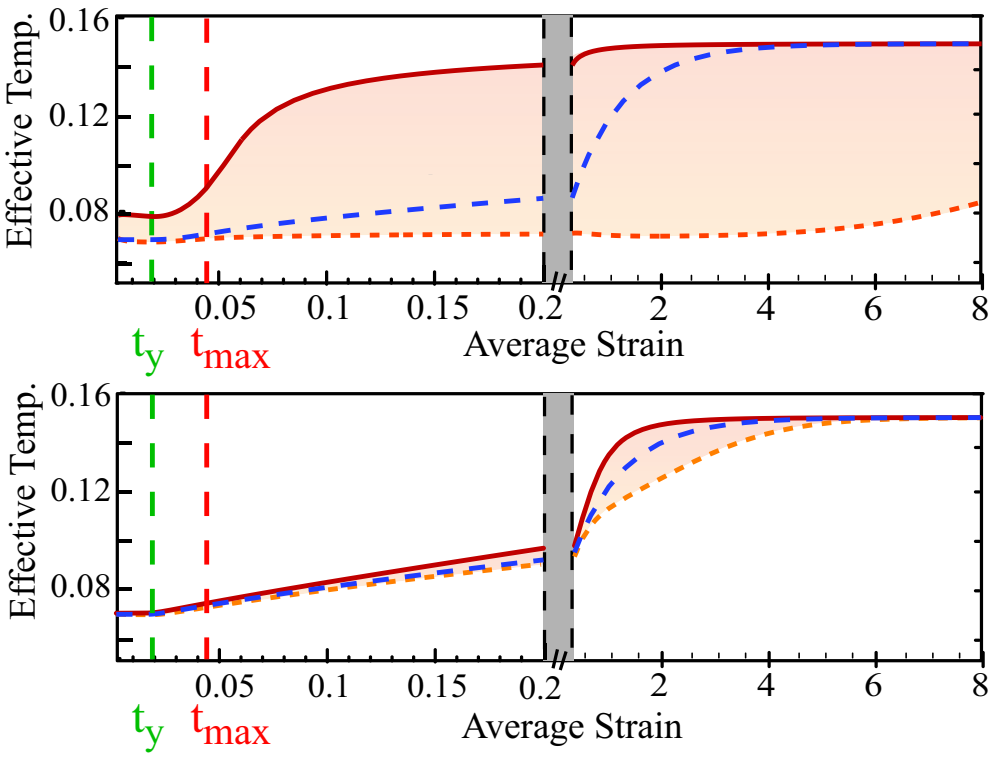

Figure 5.5: Plot of effective temperature χ as a function of time for (a) an STZ solution for $\delta\chi_0 = 0.01$ that localizes and (b) an STZ solution for $\delta\chi_0 = 0.001$ that does not localize. The middle dashed (dark blue) line indicates the homogeneous solution for χ as a function of time. The uppermost solid (red) and lowermost dashed (orange) lines correspond to the function $\chi(y)$ evaluated at a point located within the shear band and outside of the shear band, respectively. The shaded region indicates the range of values spanned by $\chi(y)$ at a specific time, so that a wide shaded region indicates a localized state. Dashed vertical lines correspond to calculated values for the time the material first reaches the yield stress, t_y, and the time the material reaches its maximum stress t_{max}.

the time derivatives of Q inside and outside the band:

$$\begin{aligned}
\frac{\partial Q_{in}}{\partial t} &= \Gamma(s)\frac{e^{-1/\chi_{in}}}{(\chi_{in})^2}\frac{\partial \chi_{in}}{\partial t} \\
&\simeq \Gamma(s)\frac{e^{-1/\chi_0}}{(\chi_0)^2}\,\omega_{\chi_{ini}}(t)\,\delta\chi(t); \qquad (5.51)\\
\frac{\partial Q_{out}}{\partial t} &= \Gamma(s)\frac{e^{-1/\chi_{out}}}{(\chi_{out})^2}\frac{\partial \chi_{out}}{\partial t} \\
&\simeq \Gamma(s)\frac{e^{-1/\chi_0}}{(\chi_0)^2}\,g(\overline{\chi}(t), s(t)). \qquad (5.52)
\end{aligned}$$

We approximate χ_{in} and χ_{out} as the initial condition, χ_{ini}. This approximation is valid only for short times when χ has not changed appreciably from χ_{ini} inside or outside the band. The ratio of the derivatives is given by:

$$\frac{\dot{Q}_{in}}{\dot{Q}_{out}}(\delta\chi, \chi_{ini}, t) = \frac{\omega_{\chi_{ini}}(k,t)\delta\chi(t)}{g(\overline{\chi}(t), s(t))}. \tag{5.53}$$

Equation (5.53) indicates that for short times when χ has not changed appreciably, the energy dissipation is determined by comparing the growth rate of perturbations to the growth rate of the mean effective temperature. Fortuitously, this is also exactly the criterion for when the frozen-time linearization is valid. In other words, the linearization is valid when more energy is dissipated inside the band and we expect continued localization, and the linearization fails exactly when the nonlinear terms lead us to expect homogeneous deformation.

Equation (5.53) must be evaluated at a particular time and wavenumber. We evaluate $\omega_{\chi_{ini}}(k,t)$ for the most unstable mode, which corresponds to $k = \pi/L$. For notational simplicity this value of k is assumed in the following derivation. In writing Eqs. (5.51) and (5.52), we required that the time t is small enough that χ remains close to χ_{ini}. Numerical solutions confirm that $\overline{\chi}$ changes very little as s increases from zero to its maximum shear stress. This stress, s_m, can be approximated as the solution to Eq. (5.30) with $\dot{s} = 0$ and $\chi = \chi_{ini}$:

$$0 = 1 - 2\frac{\epsilon_0}{q_0}\mathcal{C}(s_m)(1 - \frac{1}{s_m})e^{-1/\chi_{ini}}. \tag{5.54}$$

We must also approximate the numerator of Eq. 5.53 at the time when the perturbations are growing most rapidly. Naively, one might expect this to be the maximum of $\omega_{\chi_{ini}}(t)$ times the amplitude of the initial perturbation, $\delta\chi_0$. This underestimates the numerator because the amplitude of the perturbation increases with time.

A better approximation can be found by noting that in numerical solutions, $\omega_{\chi_{ini}}(t)$ rises almost linearly from zero at the time the material reaches the yield stress to a maximum at nearly the same time as the material attains its maximum stress, s_m. This behavior is seen in Fig. 5.4. Equation (5.44) shows that $\omega_{\chi_{ini}}(t)$ depends on t only through $s(t)$ and $\overline{\chi}(t)$, so we evaluate the stability exponent at (s_m, χ_{ini}). Therefore we can approximate the linearized equation for the perturbations, Eq. (5.43), as:

$$\dot{\delta\chi}(t) = \frac{\omega_{\chi_{ini}}(s_m, \chi_{ini})}{t_m - t_y}(t - t_y)\delta\chi(t), \qquad t_m > t > t_y, \tag{5.55}$$

where t_y is the time when the material first reaches the yield stress and t_m is the time at the maximum stress. The solution to this differential equation, evaluated at s_m, is

$$\delta\chi(t_m) = \delta\chi_0 \ \exp[\frac{\omega(s_m, \chi_{ini}) \ (t_m - t_y)}{2}]. \tag{5.56}$$

Therefore a lower bound on the numerator is given by:

$$\max_t \left[\omega_{\chi_{ini}}(t)\delta\chi(t)\right] > \omega(s_m, \chi_{ini}) \ \delta\chi_0 \ \exp[\frac{\omega(s_m) \ \Delta t}{2}], \tag{5.57}$$

where $\Delta t = t_m - t_y$ is nearly constant in all the numerical STZ solutions and is about 0.03 in units of strain.

While better than the first guess, this estimate is likely to be low because $\omega_{\chi_{ini}}(t)$ is generally not sharply peaked about t_m, so the maximum growth rate occurs at later times than t_m. To account for this and to match the numerical solutions, we choose $\Delta t = 0.10$.

Substituting these approximations into Eq. 5.53, we define *localization ratio* $\mathcal{R}$ as follows (there was a typo in the version of this equation in Ref. [70], it has been corrected here):

$$\mathcal{R}(\delta\chi, \chi_{ini}) \ = \ \frac{c_0 q_0 \omega(s_m, \chi_{ini}) \ \delta\chi_0 \ e^{\omega(s_m, \chi_{ini})0.05}}{2e^{-1/\overline{\chi}_{ini}}\epsilon_0 s_m \left(\left(\frac{\chi_0 - \overline{\chi}_{ini}}{\overline{\chi}_{ini}^2} - 1\right)\mathcal{C}(s_m)(1 - \frac{1}{s_m})\right)}, \tag{5.58}$$

where $\omega(s_m, \chi_{ini})$ is defined by Eq. (5.44). $\mathcal{R}$ is large if the system tends to focus energy dissipation inside the band and small otherwise.

We now systematically compare the value of the localization ratio to the degree of localization in a numerical STZ solution, and find that the ratio is an excellent criterion for localization.

The Gini coefficient, $\phi(t)$, is a measure of localization and is defined as follows [84, 85]:

$$\begin{aligned} \phi(t) \ &= \ \frac{1}{2n^2\overline{D^{pl}}} \sum_i \sum_j |\mathcal{D}^{pl}(y_i, t) - \mathcal{D}^{pl}(y_j, t)| \\ &= \ \frac{1}{2n^2\overline{\Lambda}} \sum_i \sum_j |e^{-1/\chi(y_i,t)} - e^{-1/\chi(y_j,t)}|, \end{aligned} \tag{5.59}$$

where the function χ is evaluated at n points in space, $\{y_n\}$. A discrete delta function has a Gini coefficient equal to unity, and a constant function has a Gini coefficient equal to zero.For each set of initial conditions, (χ_{ini}, $\delta\chi_{ini}$), we compute

a numerical solution to the STZ equations and then calculate the Gini coefficient for the strain rate as a function of position for each point in time. We define the *Numerical localization number* Φ as the maximum value of $\phi(t)$ over t. If Φ is close to unity the strain rate is highly localized (as in Figure 5.2(b)) and when Φ is close to zero the strain rate remains homogeneous.

Figure 5.6 shows that the numerical localization number Φ (rectangles) and the theoretical ratio $\mathcal{R}$ (contour plot) exhibit the same behavior as a function of χ_{ini} and $\delta\chi_0$. This indicates that the theoretical $\mathcal{R}$ is a good criterion for the numerically computed strain localization Φ.

The shading of the rectangles corresponds to the value of Φ for a given set of initial conditions: red corresponds to highly localized strain rate distributions ($\Phi > 0.8$), yellow to partially localized solutions ($0.8 \geq \Phi \geq 0.3$), and dark blue to homogeneous solutions ($\Phi < 0.3$). The contour plot corresponds to values of $\mathcal{R}$: light pink for $\mathcal{R} > 0.6$, darker shades for $\mathcal{R} \leq 0.6$. The data in figure 5.6 show that to a good approximation, $\mathcal{R} > 0.6$ corresponds to solutions with strain localization, and $\mathcal{R} \leq 0.6$ corresponds to homogeneous solutions.

The localization ratio $\mathcal{R}$ is a function only of the STZ parameters and the initial conditions for the function $\chi(y)$. This is potentially a very useful tool for incorporating effects of localization into constitutive laws. It determines an important material property without requiring computation of the full inhomogeneous system dynamics.

5.4.4 Long-time behavior

The localization ratio compares the energy dissipated inside the shear band to the energy dissipated outside the shear band, and determines whether the nonlinear dynamics enhance or inhibit shear band formation. An interesting and more difficult question is what determines whether the system dynamics result in a single shear band or multiple shear bands. The MD simulations generally have a single shear band except at the highest strain rates (see Figure 2 in [40]). In the parameter range used to match the MD simulations, the STZ solutions also exhibit a single shear band. However, outside this parameter range it is possible for the STZ equations to generate solutions with multiple shear bands.

It appears that the STZ equations generate a single shear band when the system is in a parameter range where perturbations to χ are highly unstable. In this case the largest amplitude perturbation grows rapidly, resulting in a large rate of energy dissipation at that position. Consequently the energy dissipation rates outside the shear band are smaller, which inhibits the growth of smaller amplitude perturbations. A full analysis of these dynamics is beyond the scope of

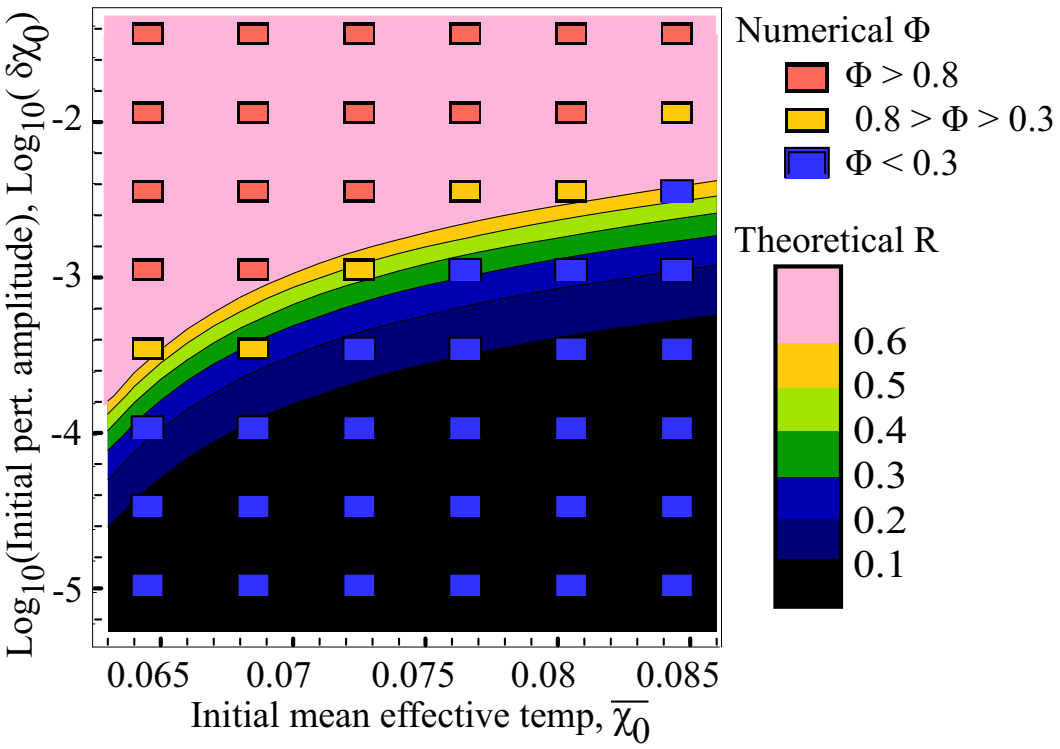

Figure 5.6: Comparison of numerical localization Φ to theoretical $\mathcal{R}$ as a function of χ_{ini} and $\log_{10}(\delta\chi_0)$. Each rectangle in Figure 5.6 corresponds to a solution to the STZ equations for a particular choice of (χ_{ini}, $\delta\chi_0$). The shading of the rectangle corresponds to the value of Φ for a numerical solution with the indicated initial conditions: medium gray (red) corresponds to highly localized strain rate distributions, $1 > \Phi > 0.8$, light gray (yellow) corresponds to partially localized solutions $0.8 > \Phi > 0.3$ and dark gray (dark blue) corresponds to homogeneous solutions $0.3 > \Phi > 0$. The background shading corresponds to a contour plot for $\mathcal{R}$. Light gray (pink) corresponds to values of $\mathcal{R} > 0.6$, black (dark purple) corresponds to values of $\mathcal{R} < 0.1$, and contours are at 0.1 intervals in between. The light gray (yellow) rectangles consistently overlay the second (yellow) contour, showing that the theory and numerics agree on the localization transition.

this work.

However, we use the fact that there is a single shear band to determine the width of that band. As discussed above, most of the strain must be accommodated in the shear band if the strain is to remain localized. χ_0 sets the steady state of disorder in the system, and we assume that χ attains this value in the shear band.

We can estimate the width of the band as a function of time, $w_E(t)$, by postulating that *all* of the shear band strain is accommodated plastically in the shear band:

$$0 = \overline{\dot{\gamma}} - \frac{1}{2L}\int_{-L}^{L} D^{pl}(y)dy; \tag{5.60}$$

$$0 = 1 - \frac{w_E}{2L}\frac{2}{q_0}\mathcal{C}(s(t))\left(1 - \frac{1}{s(t)}\right)e^{-1/\chi_0}; \tag{5.61}$$

$$\frac{w_E(t)}{2L} = \frac{q_0 \exp[1/\chi_0]}{2\mathcal{C}(s(t))(1-\frac{1}{s(t)})}, \tag{5.62}$$

where $s(t)$ is the numerical solution to the STZ equation for the stress as a function of time.

We also evaluate the width of the shear band in the numerical STZ solution for the strain rate. The numerical shear band width ($w_N(t)$) is computed as the width of the strain rate vs. position curve at a value corresponding to the imposed strain rate, $1 = V_0/L$. Figure 5.7 compares the numerical shear band width to the estimated width, as a function of time. The two are in agreement. The numerically computed width is systematically larger than the estimated width because we chose a relatively low cutoff, $1 = V_0/L$, for the strain rate in the band.

The estimated width is not a prediction for the width of the shear band because it depends on the numerical solution for the stress as a function of time. However, it does suggest that because the STZ equations contain no natural length scale for the width of a shear band, the system dynamically sets the width based on the imposed strain rate. In Chapter 6 this is called a "disorder-limited" shear band.

The shear band has a well-defined effective temperature (χ_0) and therefore accommodates a fixed rate of plastic strain per unit width at a given stress. Together, the stress and the imposed strain set the shear band width: the shear band must grow to the width required (at a fixed stress) to accommodate all of the imposed strain. While we cannot compute the shear band width analytically, we have recast the problem in terms of a potentially simpler one to solve: determining the stress relaxation as a function of time.

The value of the steady state stress has a large effect on strain localization. While the spatial dependence of $Q(y)$ is through $\chi(y)$, the magnitude of Q depends on the value of the stress through $\Gamma(s)$. When the system is in the flowing regime, the nondimensionalized stress s is always greater than one. The energy dissipation per STZ, $\Gamma(s) \propto s\mathcal{C}(s)(1-1/s)$, approaches zero as the stress approaches one from above. Therefore, if the steady state stress is very close to unity, the effective temperature dynamics become very slow – they are "frozen in" by the stress dynamics. In this parameter range the rate of plastic work can become very small

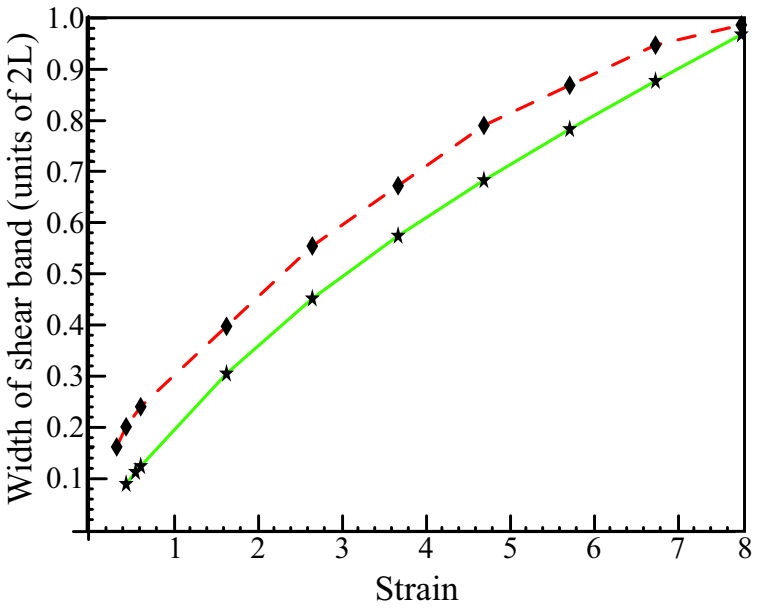

Figure 5.7: Data for shear band width as a function of strain. The red dashed line is the numerical width w_N calculated from the STZ solution for the strain rate. The solid green line is the estimated shear band width w_E calculated from the STZ solution for the stress only.

at some positions as the system approaches steady state and this is exactly what permits a localized strain state to be long-lived. In contrast, when the steady state stress is too large the magnitude of Q is also large (regardless of $\chi(y)$) and the material will not remain localized.

Numerical integration of the STZ equations confirms that localization occurs only when the steady state stress is close to unity. STZ solutions exhibit localization when q_0 is $\mathcal{O}(10^{-6})$ and χ_0 is $\mathcal{O}(1/10)$, which corresponds to a steady state stress that is very close to the yield stress ($s_f = 1.005$). However, they do not exhibit long-lived shear bands if the system is driven more quickly ($q_0 \sim \mathcal{O}(10^{-5})$), which corresponds to a steady state stress of $s_f \simeq 1.1$.

This helps us interpret MD simulation data at higher strain rates. In addition to the data shown in Figure 5.1, Shi, *et al.* have computed stress-strain curves for two higher strain strain rates (five and 25 times greater, respectively, than the strain rate used to generate Fig. 5.1) [86].

The lowest strain rate is denoted *V1* and the higher strain rates are denoted *V2* and *V3*. In this Chapter we defined the timescale ratio q_0 using *V1*. Therefore *V2* corresponds to $5q_0$ and *V3* corresponds to $25q_0$. The highest strain rate

q_0	$s_f(5q_0)/s_f(q_0)$	$s_f(25q_0)/s_f(q_0)$
1.6×10^{-6}	1.005	1.028
1×10^{-5}	1.028	1.144
1×10^{-4}	1.185	1.695

Table 5.2: Comparison of the STZ steady-state flow stress for different values of q_0.

is $5 \times 10^{-}4t_0^{-1}$. Although it is comparing apples to oranges, we note that this corresponds to the strain rate in the HL data where $\hat{\chi}$ just begins to depart from χ_0. (See Figure 3.2.)

We numerically integrate the STZ equations at $5q_0$ and $25q_0$ and find that the resulting stress-strain curves do not match the simulation data. The theoretical STZ steady state flow stress is the same for all three strain rates, while in the MD simulations the flow stress for a system driven at *V3* is significantly ($\sim 15\%$) higher.

One way to eliminate this discrepancy is to assume that we have misidentified the original timescale ratio q_0. For a given value of q_0 (and χ_0), we can calculate the flow stress s_f using Eq. (5.28). To match the simulation data, the flow stress that corresponds to $25q_0$ should be 15% higher than the flow stress that corresponds to q_0. In Table 5.2 we have calculated the flow stress ratios for several values of q_0. This table shows that $q_0 \simeq 1 \times 10^{-5}$ better fits the MD simulation data for different strain rates than $q_0 \simeq 1 \times 10^{-6}$. The higher value for q_0 also makes sense physically because it corresponds to an STZ timescale τ_0 which is simply the natural timescale for the Lennard-Jones glass, t_0.

Our athermal model requires a small value for q_0 to generate solutions with long-lived localized states, but a larger value of q_0 to be consistent with MD simulations data for different strain rates. This disparity is likely an indication that the athermal approximation does not adequately capture long-time behavior of Lennard-Jones glasses, or that a rate-dependent steady state effective temperature is required.

In an athermal description, the effective temperature always tends towards χ_0 because there is no thermal relaxation. Alternatively, if the effective temperature can relax towards a thermal bath temperature in regions where there is little plastic deformation, localized states can persist even when s_f is large. It seems likely that a thermal description would generate localized solutions with higher values for q_0. Although the athermal STZ formulation reproduces many aspects of the MD simulations, a model with thermal relaxation may be required to capture more details of the MD simulations. This will be a direction of future research.

5.5 Concluding Remarks for Chapter 5

We have investigated the athermal STZ model with effective temperature for amorphous materials in a simple shear geometry. In contrast to other studies, the effective temperature field varies as a function of position and by numerically integrating the STZ equations we have shown that the resulting solutions can exhibit strain localization. The numerical STZ solutions match the stress-strain curves for MD simulations of Lennard-Jones glasses by Shi, *et al.* and exhibit strain rate and effective temperature fields that are consistent with those seen in simulations.

The continuum STZ model provides a framework for understanding how shear bands nucleate and persist for long times. We have shown that the model is unstable with respect to small perturbations of the effective temperature during the transient dynamics, though it is stable to perturbations in steady state. Interestingly, shear localization does not always occur when the system is transiently unstable because shear bands can only form if the perturbations grow quickly compared to the homogeneous solution. This is a nonlinear effect which is driven by uneven energy dissipation in the system. Using rough approximations to these nonlinear dynamics we were able to derive a localization criterion that depends only on the initial conditions for the effective temperature.

In the parameter range studied, STZ theory predicts that the sheared material attains a state with a single shear band. The effective temperature field reaches its steady state value χ_0 in the shear band and remains close to its initial value outside the band. To a good approximation, all of the strain imposed at the boundaries is accommodated in the band, and we determine the width of the shear band using the STZ expression for the plastic strain rate when $\chi = \chi_0$. This analysis implies the shear band width is not determined by an inherent length scale in the material, but instead by a dynamical scale set by the imposed strain rate.

Interesting questions remain concerning the interaction between shear bands and material boundaries. We evaluate the STZ equations with simple, periodic boundary conditions on the effective temperature field. In our numerical solutions, the location of the shear band depends on the details of the initial fluctuations in χ and therefore seems arbitrary on macroscopic scales. This is similar to what is seen in Shi, *et al.* for simulations with periodic boundary conditions. However, in other MD simulations and in experiments on bulk metallic glasses the boundary conditions are non-trivial and most likely play an important role in nucleating shear bands. For example, in simulations by Varnik et al. [41] the system is driven at the boundary by a rough, rigid layer and the material consistently develops shear bands at the boundary. Additional simulations by Falk and Shi [87] show

that shear bands are more likely to occur in the presence of surface defects.

Boundary conditions may also influence the long-time behavior of shear bands. The long-lived, localized solutions to the STZ equations are not truly stationary states – at long times the shear band will diffuse to cover the entire strip and the system will become homogeneous. Figure 5.8 is a plot of the steady state stress vs. the natural log of the imposed strain-rate for STZ solutions. This function is not multivalued, indicating that the only steady state solution to the STZ equations with periodic boundary conditions is the spatially homogeneous solution $\chi(y) = \chi_0$, $s = s_f$. Even excluding diffusion, the STZ equations will evolve to a homogeneous solution because the plastic dissipation rate is positive everywhere, which means the effective temperature is everywhere driven towards χ_0, albeit at different rates. However, if the effective temperature field is specified at the boundaries (i.e, the boundary causes ordering and fixes the disorder temperature there) then it is possible for solutions to have inhomogeneous steady states. This is similar to results for simulations with rough, rigid boundaries where the material develops *stationary* localized states [41]. More work is needed to understand the relationship between shear band development and material boundaries, and STZ theory should provide an excellent framework for these investigations.

The athermal STZ description provides a simple starting point for understanding the dynamics of shear band formation. As discussed in the previous section, a thermal description is likely a better model for the MD simulations at different strain rates. Adding thermal relaxation to the STZ equations generates a picture of localization similar to those found in complex fluids, where the stress vs. strain rate curve is multi-valued [88]. As discussed by Langer [52] and Foglia [81], relaxation terms in the equation for the effective temperature generate solutions where the steady state stress is a multi-valued function of the strain-rate. In steady state, two regions with different strain rates can coexist: one region which is nearly jammed except for thermal rearrangements and a second region where STZs are constantly created and flipped, resulting in plastic flow.

This is different from the athermal theory where all of the material deforms due to shear-induced transitions, though the transitions occur at different rates. While athermal analysis provides a simple framework for understanding mechanisms leading to shear band nucleation, an STZ formulation with thermal relaxation may further enhance our understanding of steady-state dynamics and connect mechanisms for localization in amorphous solids to those in complex fluids.

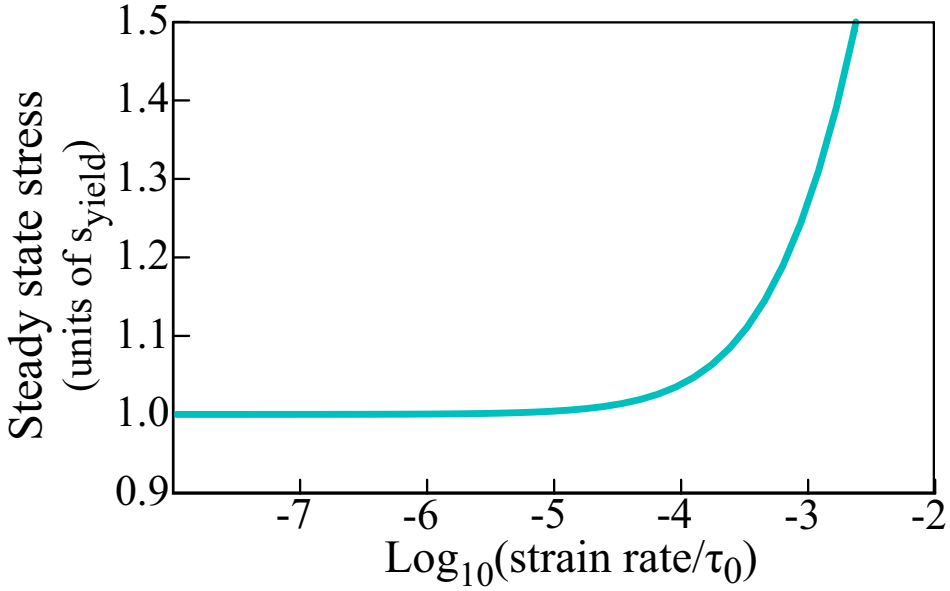

Figure 5.8: STZ solution for the steady state stress vs. Log_{10} of the imposed total strain rate. The curve is single-valued throughout, indicating that the system does not posses steady state coexisting regions with two different phases unless imposed by the boundary conditions.

Chapter 6

Rate-dependent deformation

This chapter uses STZ theory to develop a deformation map for amorphous solids as a function of the imposed strain rate and initial conditions. By combining the insights of Chapter 3 with the techniques developed in Chapter 5, we find that the STZ model describes a broad range of deformation behavior, from homogeneous deformation to extremely thin shear bands and material failure. In particular, we account for the brittle to ductile transition as a function of strain rate in amorphous materials, and provide a new explanation for the width of shear bands in bulk metallic glasses. We also show that the STZ model, which has many internal degrees of freedom corresponding to all the points in the effective temperature field, exhibits macroscopic behavior which is very different from rate-and-state friction models.

Section 6.6 discusses elastodynamic rupture simulations for earthquake faults in a parameter regime where very thin shear bands occur. This section relies heavily on numerical simulations performed by Eric Daub and is a synopsis of work first published by Daub, Manning, and Carlson in Geophysical Research Letters [89].

6.1 Background

Amorphous solids such as foams, dense colloids, bulk metallic glasses, and granular fault gouge are ubiquitous in engineering applications and natural systems. Although these materials exhibit a yield stress on experimental time scales, they flow, deform, and fail in a manner which is different from crystalline solids or Newtonian fluids. Many of these materials undergo strain localization, where a small region deforms much more rapidly than adjacent regions. For example, bulk metallic glasses develop very thin shear bands [18, 27], fault gouge in earth-

quake faults develops a prominent fracture surface that accommodates most of the slip [29], and colloidal systems develop broad shear bands [90].

Strain localization significantly affects macroscopic material properties. In metallic glasses and some earthquake faults the deformation becomes so localized that materials melt and fail. These failure modes may look like cracks, but the dynamics that lead to their formation can be very different from failure modes in crystalline materials [18]. The amount of shear stress that these solids can support also depends on the degree of localization. For example, weakening in fault gouge coincides with the formation of shear bands in the material [4].

Surprisingly, the mechanisms that lead to this strain localization have remained elusive. An early theory of shear banding [19] suggested that a small increase in the thermal temperature lowers the viscosity, resulting in more rapid deformation and a local increase in temperature. However, Lewandowski and Greer showed that shear bands in bulk metallic glasses can not be explained by adiabatic thermal effects [20]. Furthermore, thermal fluctuations are not large enough to activate particle rearrangements in systems with more massive particles, such as colloids or fault gouge. Although thermal heating must play a role at high strain rates, it does not appear to govern the formation of shear bands.

In this chapter we show that a broad range of rate-dependent strain localization effects in a variety of amorphous materials can be explained by a feedback between the local strain rate and the configurational disorder of an amorphous packing. We use a Shear Transformation Zone (STZ) theory to model deformation in amorphous solids, where the density of zones is governed by an effective temperature.

In a sheared, steady-state, non-equilibrium amorphous material, the effective temperature can be calculated by measuring the fluctuations and linear response of an observable such as the pressure and applying the fluctuation-dissipation theorem (FDT) [37, 38, 53]. Ono et. al have shown that in several simulated foams, measurements of different observables yield a single, rate-dependent steady state effective temperature which is distinct from the thermal temperature [38]. In addition, these authors show that the FDT effective temperature is consistent with an entropic definition: the effective temperature is the derivative of the configurational entropy with respect to the (potential) energy. Slow steady shearing causes the material to ergodically explore all possible configurational packings, and therefore the system maximizes a configurational entropy.

The STZ model describes plastic deformation in amorphous material as a series of localized plastic events that occur in susceptible regions, or zones [45, 46, 47]. Following Falk and Langer, we model STZs as bistable regions that are more likely than the surrounding material to deform under stress, and are created and

annihilated as energy is dissipated in the system [47]. This model has successfully been used to describe bulk metallic glasses, thin films, and hard spheres in several different geometries [70, 57, 77, 51, 30].

An important feature of all STZ formulations is that the zones are activated by an effective temperature or free volume, and there is a feedback between packing structure and deformation. In particular, we postulate that an STZ is an unlikely, high energy configuration of an amorphous packing. Because the effective temperature governs the statistics of configurational packings, the steady state density of STZs, $\hat{\Lambda}$, should correspond to a Boltzmann factor,

$$\hat{\Lambda} = \exp\left[\frac{-E_z}{k_B\, T_{eff}}\right] \equiv \exp\left[-\frac{1}{\chi}\right], \tag{6.1}$$

where E_z is an activation energy, k_B is the Boltzmann constant, T_{eff} is the effective temperature, and $\chi \equiv E_z/(k_B T_{eff})$ is a dimensionless effective temperature [57].

Because plastic deformation occurs only at these STZs, the plastic strain rate in pure shear is proportional to this density, and in many situations can be written as follows:

$$\tau_0 \dot{\gamma} = 2\, e^{-1/\chi} f(s), \tag{6.2}$$

where $f(s)$ is a function of the deviatoric stress s and τ_0 is an internal timescale such as the phonon frequency. For the remainder of this chapter we will use a dimensionless strain rate, $q = \dot{\gamma}\tau_0$. In addition, we will focus on deformation in geometries where the equilibrium shear stress is constant across the sample. Although there are many interesting geometries with shear stress gradients (and STZ theory can explain these shear bands [30]), stress effects generally dominate the more subtle internal structural dynamics. In contrast, experiments in simple shear geometries find that strain localization occurs even when the equilibrium stress is constant, indicating that some property of the internal state governs shear band formation.

Shear banding is caused by the coupling in Eq. 6.2 between a configurational or structural parameter and the plastic rate of deformation, although the details are subtle. In the low strain rate limit, shear bands will never form if the STZ model is already in steady state [70]. However, a frozen-time stability analysis shows perturbations to the effective temperature can grow and form shear bands during the transient plastic response when the material is driven from rest. These shear bands evolve and persist for long times, resulting in a very different rheology compared to the homogeneous steady state [40].

In this chapter, we investigate strain localization in the STZ model as a function of the imposed strain and the initial material preparation. By including new

information about the glassy behavior of the effective temperature as a function of the strain rate [53, 59], we find that the STZ model exhibits a broad range of deformation behaviors, including homogeneous deformation, broad shear bands, thin shear bands, and failure. In addition, we suggest that the type of deformation has important implications for the macroscopic material and frictional properties — systems that localize also weaken rapidly. Although the stress equilibrates quickly, the effective temperature dynamics continue to evolve over much longer timescales. We suggest that the frictional response of these localized systems is vastly different from that of a homogeneously deforming system, and that localization may play a role in dynamic weakening seen at high shear speeds in granular materials.

6.2 STZ model details

We model deformation in an amorphous material using athermal, non-steady-state STZ theory, developed in Chapter 2. Neglecting thermal relaxation terms in Eq. 2.33 (assuming that we are below the thermal glass transition temperature), the equation for χ as a function of time is:

$$\dot{\chi} = \frac{1}{\tilde{c_0}\tau_0} e^{-1/\chi} \chi \, \Gamma(s) \left[1 - \frac{\chi}{\hat{\chi}(q)} \right]. \tag{6.3}$$

Inserting Eq. 6.2 into the equation for the rate of deformation tensor (Eq. 2.3) and integrating across the width of the material (in the y-direction) results in a second equation for the stress dynamics:

$$\frac{ds}{d\overline{q}} = \mu^* \left(1 - \frac{2\epsilon_0}{\overline{q}} \mathcal{C}(s) \left(\mathcal{T}(s) - m(s) \right) \overline{\Lambda} \right), \tag{6.4}$$

where $\overline{q}$ is the imposed average strain rate times the STZ time scale, $(V_0/L)\,\tau_0$, and $\overline{\Lambda}$ is the spatial average of the STZ density $\Lambda = \exp(-1/\chi)$. The shear heating factor $\Gamma(s)$ is defined by Eq. 2.19 for thermal temperatures below the glass transition temperature . Substituting this expression into Eq. 6.3, we derive an equation for the χ dynamics:

$$\frac{d\chi}{d\overline{q}} = \frac{2\epsilon_0 \mathcal{C}(s)\, s}{\tilde{c_0} s_0 \overline{q}} \left(T(s) - m(s) \right) e^{-1/\chi} (1 - \frac{\chi}{\hat{\chi}(q)}) + D_\chi^* \frac{\partial^2 \chi}{\partial y^2}. \tag{6.5}$$

We use the rate factor $R(s)$ given by Eq. 2.24 [59]:

$$2\mathcal{C}(s) = R(s) = \exp\left[-\frac{T_E}{T}\, e^{-s/\tilde{\mu}}\right]\left[1 + \left(\frac{s}{s_1}\right)^2\right]^{n/2}. \tag{6.6}$$

The function $\hat{\chi}(q)$ is defined by Eq. 2.32.

6.3 Stability Analysis

We saw in Chapter 5 that at low strain rates the STZ model often does not reach a homogeneous steady state. Instead, the system develops shear bands that persist for extremely long time scales ($> 800\%$ strain). We were able to predict when the system would exhibit shear bands by linearizing the system of equations about a time-varying trajectory [70].

Although $\hat{\chi}(q)$ approaches a constant value χ_0 at low strain rates, simulations by Haxton and Liu [53] and Ono et al [38] show that the steady state effective temperature becomes strongly rate dependent at higher strain rates. This means that the amorphous packing structure in a shear band can be very different from that in a steady state homogeneous solution. We now study the stability of this more complicated system.

First, the evolution equations for χ and s can be written as follows:

$$\dot{s} = F(s,\chi) \;=\; \mu_*\left(1 - 2\, f(s)\int dy\, e^{-1/\chi}\right); \tag{6.7}$$

$$\dot{\chi} = G(s,\chi) \;=\; = 2f(s)e^{-1/\chi}\left(\frac{s\chi}{c_0 s_0}\left(1 - \frac{\chi}{\hat{\chi}}\right) + a^2\frac{\partial^2\chi}{\partial y^2}\right). \tag{6.8}$$

Then the Jacobian $J = \{dF/ds, dF/d\chi\}, \{dG/ds, dG/d\chi\}$ evaluated at $s = \overline{s}, \chi = \overline{\chi}$ is given by:

$$J = \begin{bmatrix} -2\mu_* e^{-1/\overline{\chi}} f'(\overline{s}) & -2\mu_* e^{-1/\overline{\chi}} f(\overline{s}) W(\delta\chi)/\overline{\chi}^2 \\ \frac{-2\overline{\chi}e^{-1/\overline{\chi}}}{s_0 c_0 \hat{\chi}}\left(\overline{\chi} - \hat{\chi}\right)\left(f'(\overline{s}) + f(\overline{s})\right) & \frac{-2e^{-1/\overline{\chi}} f(\overline{s})\overline{s}}{s_0 c_0 \overline{\chi}\hat{\chi}}\left(\overline{\chi} + 2\overline{\chi}^2 - \hat{\chi} - \overline{\chi}\hat{\chi}\right) \end{bmatrix}. \tag{6.9}$$

The term $W(\delta\chi)$ is a spatial integral over one period of the perturbation function; it selects only the zero-wavenumber component of the perturbing function because the other components must satisfy periodic boundary conditions. Details can be found in Chapter 5.

The system is linearly stable with respect to perturbations from a homogeneous steady state, $\overline{\chi} = \hat{\chi}$, because in this case the lower left entry in the Jacobian (J_{21}) is zero, the Jacobian is upper triangular, and the diagonal entries are strictly negative. In other words, a steady-state, homogeneously deforming system will always remain homogeneous.

However, experiments and simulations show that many systems never reach this homogeneous steady state. This leads us to investigate the frozen-time stability of perturbations to a spatially homogeneous trajectory, as first discussed in Chapter 5. Utilizing the same techniques used to derive Eq. 5.42, we find that spatial perturbations to χ with zero mean do not change the equation for $\dot{s}$: $F(s, \overline{\chi} + \delta\chi) = F(s, \overline{\chi})$. In this case the stability is determined solely by the equation for χ and the sign of J_{22}. Above the yield stress, χ and $f(s)$ are strictly greater than zero and therefore J_{22} is negative (and the trajectory is linearly stable) whenever the following criteria is met:

$$\chi > \chi_{crit} = \frac{1}{4}\left((\hat{\chi} - 1) + \sqrt{1 + 6\hat{\chi} + \hat{\chi}^2}\right). \tag{6.10}$$

By inserting values for $\hat{\chi}(q)$ into Eq. 6.10, we derive a linear stability prediction for the boundary between these two regimes as a function of the average initial effective temperature $\overline{\chi}$ and the applied strain rate q. We choose $\hat{\chi}(q)$ to fit the Haxton-Liu data in Fig. 3.1(b).

Figure 6.1 is a deformation map that predicts the type of flow as a function of the initial conditions for the simulated glassy material studied by Haxton and Liu [53]. The thin line marked with open circles is the linear stability criterion defined by Eq. 6.10. Above χ_{crit}, linear stability analysis predicts homogeneous deformation, while localized deformation is expected below this line. The uppermost line marked with crosses represents $\hat{\chi}(q)$ chosen to fit the simulation data by Haxton and Liu [53].

This analysis is a frozen-time stability analysis, which is valid when the perturbations grow rapidly compared to the growth of the underlying trajectory. As discussed in Section 5.4.3, this means that the frozen-time stability criterion is an approximation which breaks down as the perturbation amplitude decreases. To correct for this, we again utilize the localization ratio $\mathcal{R}$, first discussed in Chapter 5, which compares the growth rate of perturbations to the growth of the underlying trajectory. This ratio is defined as:

$$\mathcal{R} = \delta\chi \frac{\exp[J_{22}(s_m, \chi_{ini})\Delta t] J_{22}(s_m, \chi)}{G(s_m, \chi)}, \tag{6.11}$$

where $\delta\chi$ is the magnitude of the perturbation, χ_{ini} is the initial effective tempera-

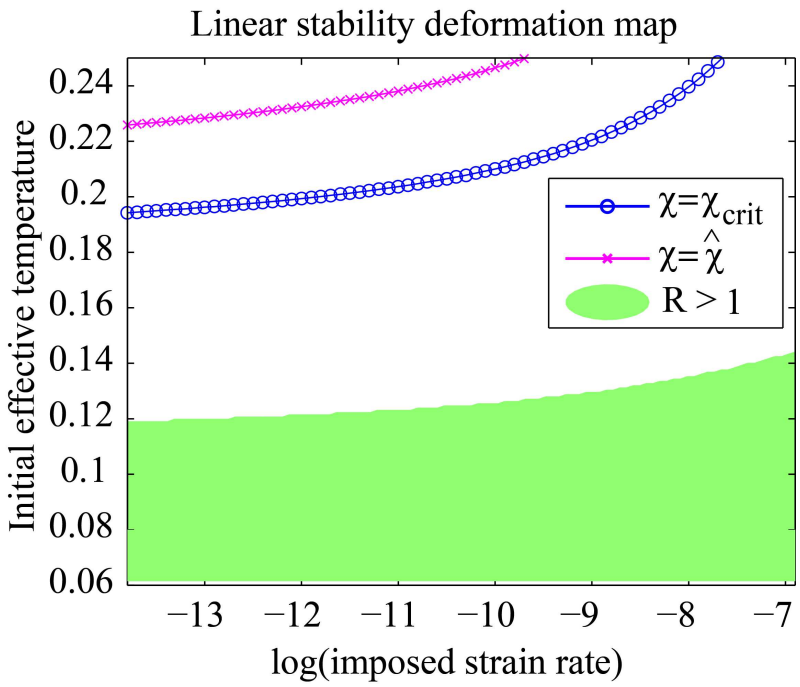

Figure 6.1: Deformation map predicted by a frozen time linear stability analysis. The solid line marked with open circles represents the linear stability criterion predicted by Eq. 6.10. The line marked with crosses indicates the function $\hat{\chi}(q)$ extracted from the Haxton-Liu data [53]. $\mathcal{R}$ is a more accurate generalized stability criterion that takes into account finite amplitude perturbations. For $\mathcal{R} < 1$ (white) homogeneous deformation is predicted and for $\mathcal{R} > 1$ (shaded) strain localization is predicted.

ture and s_m is the approximate maximum shear stress given by $\overline{q} = 2\epsilon_0 f(s_m)\ \exp[1/\chi_{ini}]$. Localization is expected to occur when $\mathcal{R}$ is greater than 1. The shaded region in Fig. 6.1 corresponds to $\mathcal{R} > 1$, calculated for $\delta\chi = 0.05\chi_{ini}$, and $\Delta t = 0.03$.

To check these analytic predictions, we numerically integrate the STZ partial differential equations. To resolve extreme localization, we utilize an irregular mesh and a combination of fixed– and adaptive–step finite difference methods. The degree of localization can be quantified using the Gini coefficient ϕ [85], defined as:

$$\phi(t) = \frac{1}{2n^2 \overline{D^{pl}}} \sum_i \sum_j |\mathcal{D}^{pl}(y_i, t) - \mathcal{D}^{pl}(y_j, t)| \tag{6.12}$$

The Gini coefficient is non-negative and equal to zero if the material deforms

homogeneously. Figure 6.2(a) is an intensity plot of the maximum value of the Gini coefficient as a function of the average initial effective temperature, χ_{ini} and the natural logarithm of the dimensionless imposed strain rate $\log(q)$. The value at each point was obtained by numerically integrating the STZ equations. The initial effective temperature was perturbed by a hyperbolic secant function of height $\delta\chi$ and width $L/10$, and the initial effective temperature function $\chi(y)$ was normalized so that its average was χ_{ini}. This deformation map indicates that material deformation gradually changes from homogeneous flow to shear banding as a function of the initial conditions.

In some simulations, the steady state effective temperature $\hat{\chi}$ approached infinity. Although the STZ model given by Eqns. 6.4 and 6.5 is still well-defined in this limit, the shear heating term becomes considerably amplified. The shear band becomes so thin that the numerical integration routine fails, although the numerical mesh is fine enough to resolve a band ten times smaller than a, which is the smallest length scale in our model. These numerical integration results indicate that there is a one-to-one correspondence between situations where $\hat{\chi}$ approaches infinity and the shear band localizes to a scale smaller than the diffusion length scale. In addition, the STZ model does not hold at length scales smaller than a, which should be about the radius of an STZ. Therefore we suggest that when $\hat{\chi} \to \infty$ and the STZ solid-like description breaks down, the material fails along the band. In figure 6.2(a), dark red boxes indicate that $\hat{\chi}$ approached infinity during a particular numerical integration.

Figure 6.2(b) is an intensity plot of the maximum plastic strain rate achieved inside the material, normalized by the average imposed strain rate. Again, dark red boxes correspond to shear bands where the plastic strain rate reaches the system melting point and the model breaks down.

6.4 Localization dynamics

We have shown that shear bands can develop in the STZ model, but we would also like to understand what types of shear bands persist and what sets the thickness of the bands. In addition, what are the implications of this localization for macroscopic system response?

The internal state of the system at each point in time is completely determined by the deviatoric stress s and effective temperature field, $\chi(y)$. We have seen in the previous section that the transient dynamics can lead to inhomogeneous flows. We now ask a different question: Assuming that transient inhomogeneous flows occur, which types of deformation will persist long enough for experiments and

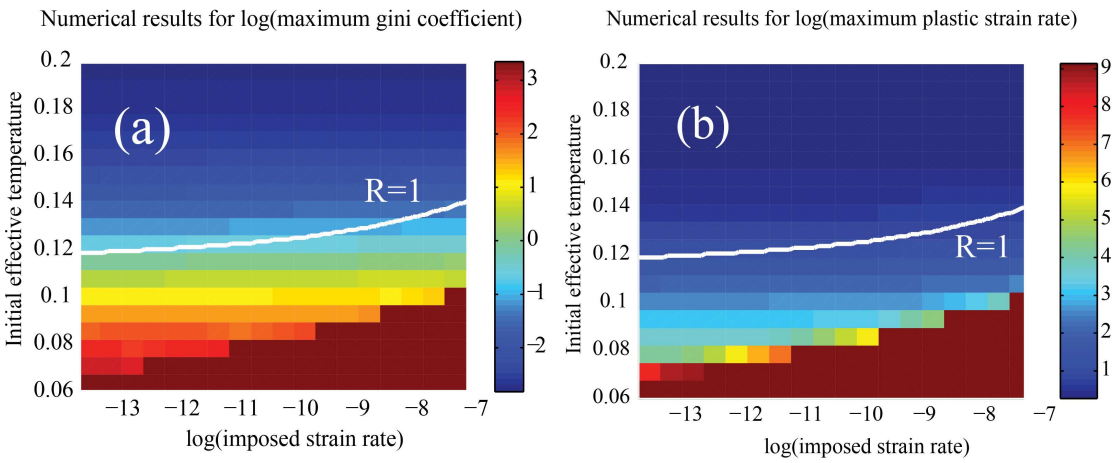

Figure 6.2: A diagram showing the degree of localization found in by numerically integrating the STZ equations. The deviatoric stress is initially zero and the initial effective temperature field is a hyperbolic secant function with a height $\delta\chi$, a width of $L/10$, and an average value of χ_{ini}. (a) The log of the maximum Gini coefficient (Eq. 6.12) as a function of the average initial effective temperature and the externally imposed strain rate. A higher Gini coefficient indicates more localization. (b) The log of the maximum plastic strain rate attained in the band normalized by the externally imposed strain rate. In both figures, dark red boxes correspond to numerical simulations where the magnitude of the strain rate was so large that $\hat{\chi} \to \infty$, as discussed in the text. The solid white line corresponds to the predicted localization ratio $\mathcal{R} = 1$.

simulations to identify them? We now show that there are three three different internal states for which the χ dynamics (Eq. 6.8) slow down drastically, and these are the states that persist for long times.

The first state, called "homogeneous deformation", occurs when the effective temperature field is constant everywhere and equal to $\hat{\chi}(\overline{q})$, where $\overline{q}$ is the externally imposed dimensionless strain rate. Since both the shear heating and diffusion terms are zero in Eq. 6.8, this is a true steady state that persists forever. An example of homogeneous deformation is shown in Figs. 6.4(a) and 6.4(b). An initial perturbation to the effective temperature generates a small perturbation to the strain rate, but the perturbation relaxes towards a homogeneous state and the normalized strain rate is always of order one. The corresponding stress-strain curve is shown in Fig. 6.3.

A second state, called "diffusion-limited localization", occurs when the shear heating and diffusion terms in Eq. 6.8 balance. In this case the effective temper-

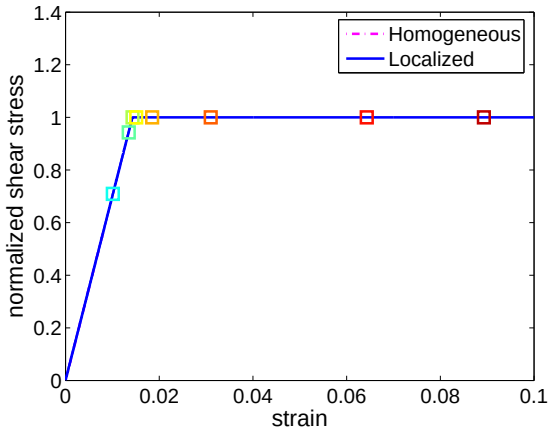

Figure 6.3: Deviatoric stress s vs. strain calculated by numerically integrating the STZ equations of motion with initial conditions $\chi_{ini} = 0.0674$, $\overline{q} = 1.015 \times 10^{-6}$. The blue curve represents the solution to the perturbed system, while the magenta curve represents a homogeneous solution where the effective temperature is constrained to be constant inside the material. In this plot the two curves are indistinguishable. The colored boxes correspond to the plots shown in Fig. 6.4. Because χ_{ini} is large, the system begins with a large number of plasticity carriers and therefore the stress peak is negligible. This system does not localize.

ature field is far from its steady-state value $\hat{\chi}$ at all points in space, so that the factor $(1 - \chi/\hat{\chi})$ is close to unity and the shear heating term $s\chi/(s_0 c_0)$, which is of order one, balances the diffusion term a^2. The system develops a shear band with a width of order a. Although diffusion of potential energy (and presumably effective temperature) has been seen in simulations [40], the length scale a associated with this diffusion constant is relatively unconstrained by simulations or experiments. A reasonable postulate is that a is on the same order as the radius of an STZ, or equivalently, a few particle radii. This suggests that diffusion-limited shear bands are very narrow. An example of a diffusion-limited shear band is shown in Figures 6.6(a) and 6.6(b). A small initial perturbation to the effective temperature is driven by a dynamic instability to a much higher value, which results in a very narrow peak in the strain rate. The inset plots magnify the position axis, illustrating that the numerical precision is sufficient to resolve the narrow peaks. Note that the strain rate in the center of the shear band is nearly 3000 times larger than the externally imposed strain rate.

The corresponding stress-strain curve is shown in Fig. 6.5. The magenta curve corresponds to a system which is constrained by symmetry to remain homoge-

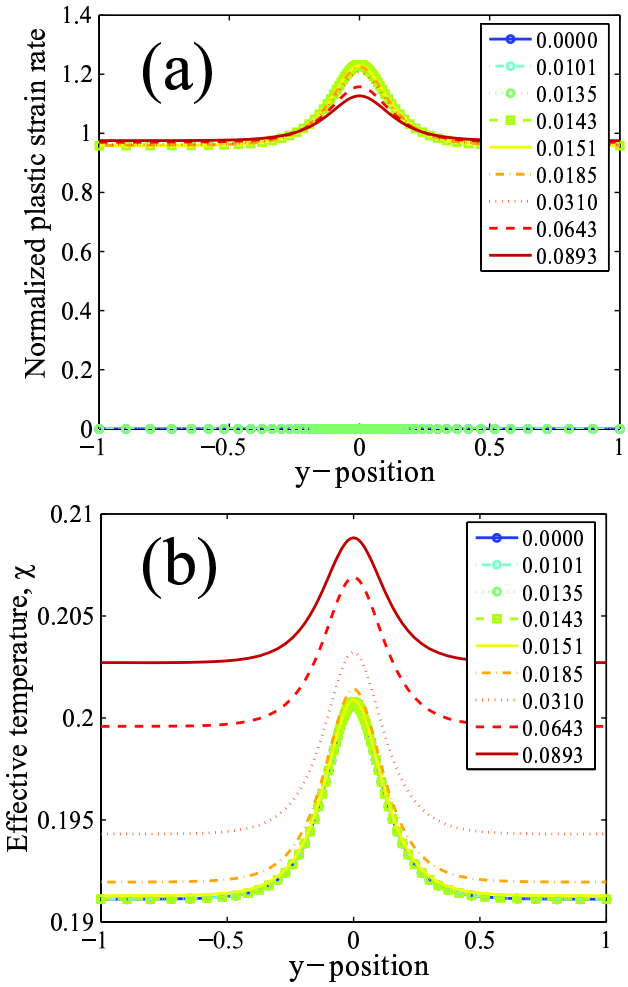

Figure 6.4: Homogeneous flow (a) Normalized plastic strain rate $\dot{\gamma}(y)\tau_0/\overline{q}$ and (b) effective temperature as a function of position, for a material with initial conditions $\int dy\, \chi(y, t = 0) = \chi_{ini} = 0.20$, and imposed strain rate $\overline{q} = 1.015 \times 10^{-6}$. Different colored lines represent different times; cooler colors (blue) correspond to earlier times, while warmer colors (red) correspond to later times. The plastic strain rate $\dot{\gamma}(y)$ is normalized by the imposed strain rate, so that the spatial integral of $\dot{\gamma}(y)\tau_0/\overline{q}$ is unity.

neous, while the blue curve corresponds to a perturbed system with the same average initial conditions. The blue curve weakens much more rapidly during the onset of shear localization, and illustrates that thin shear bands drastically change the macroscopic system response.

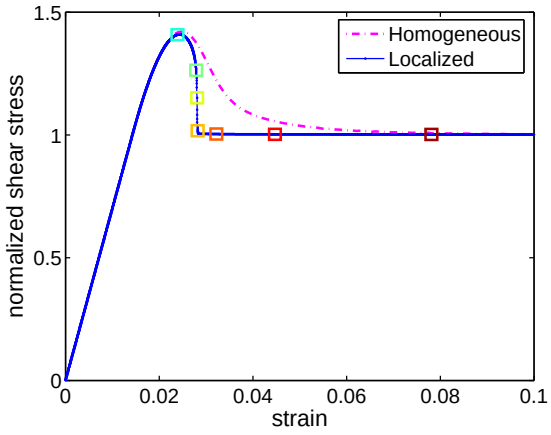

Figure 6.5: Shear stress s vs. strain calculated by numerically integrating the STZ equations of motion with initial conditions $\chi_{ini} = 0.0674$, and imposed strain rate $\overline{q} = 1.015 \times 10^{-6}$. The blue curve represents the solution to the perturbed system, while the magenta curve represents a homogeneous solution where the effective temperature is constrained to be constant inside the material. The colored boxes correspond to the plotsshown in Fig. 6.6. At about 2% strain, the perturbed system begins to localize. At this point the blue curve weakens much more rapidly than the magenta curve.

In addition, the local strain rate in these diffusion-limited shear bands can become so large that the steady state effective temperature $\hat{\chi}$ approaches infinity, indicated by dark red boxes in Fig 6.2. In this case the shear bands become so thin that numerical integration of the STZ model breaks down, indicating that the amorphous packing is becoming more and more disordered inside the band. Although the simple STZ model developed here does not specify the rheology at strain rates above this "melting" point, it does suggest that the solid-like STZ theory must be replaced by a liquid-like theory (such as mode-coupling or Bagnold scaling) inside these extremely narrow bands. We suggest that when the disorder temperature approaches infinity, the material fails: bulk metallic glasses break along a thin shear band and earthquake faults develop a prominent fracture surface.

The third "disorder-limited" localized state is less intuitively obvious. Neglecting the diffusion term, the right hand side of Eq. 6.8 is proportional to the product of two factors, $\exp(-1/\chi)$ and $(1-\chi/\hat{\chi})$. The former is very close to zero whenever χ is significantly less than χ_0, and the latter is zero when $\chi = \hat{\chi}$. The disorder limited state occurs exactly when the small-χ condition is met outside

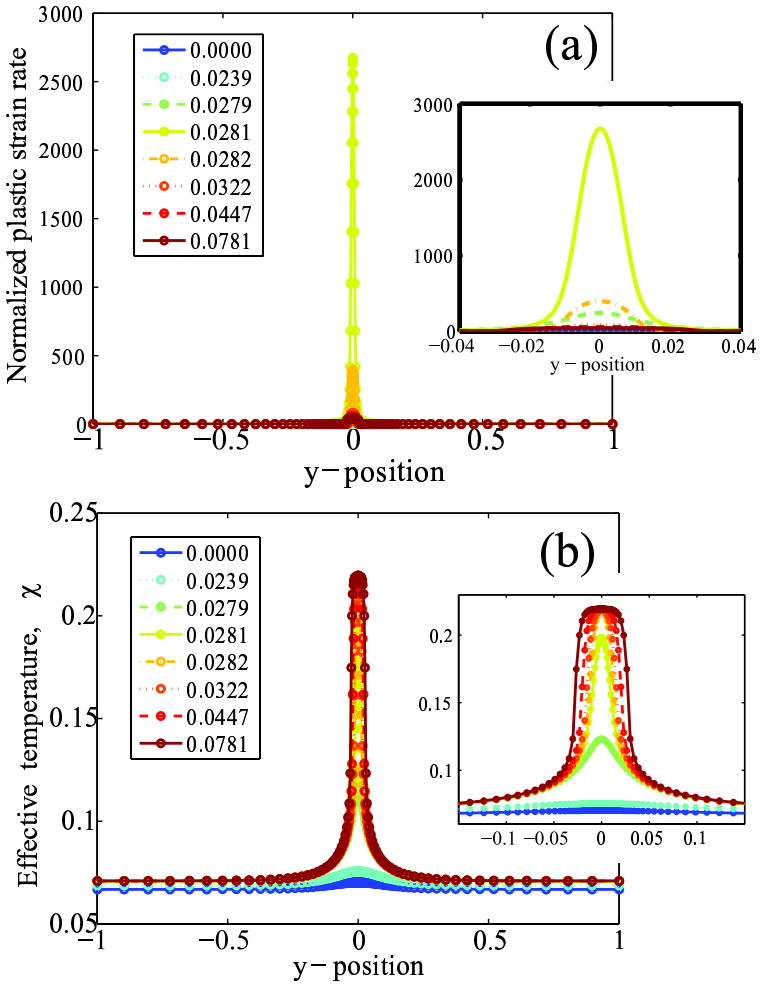

Figure 6.6: **Diffusion-limited shear band** (a) Normalized plastic strain rate $\dot{\gamma}\tau_0/\overline{q}$ and (b) effective temperature as a function of position, for a material with initial conditions $\chi_{ini} = 0.0674$, and imposed strain rate $\overline{q} = 1.01510^{-6}$. Different colored lines represent different times; cooler colors (blue) correspond to earlier times, while warmer colors (red) correspond to later times. The plastic strain rate exhibits an extremely narrow shear band with a width of about 0.015, which is approximately the same as the diffusion length scale a. The insets show the same data on a different scale: the position axis is magnified to give a clearer picture of the dynamics within the narrow band.

the shear band and $\chi = \hat{\chi}$ inside the band, so that $\dot{\chi}$ in Eq. 6.8 is always small. This is the type of shear band described in Chapter 5 and identified in simulations

by Shi et al [40]. For comparison, we show an example of a disorder-limited shear band in Figs. 6.8(a) and 6.8(b).

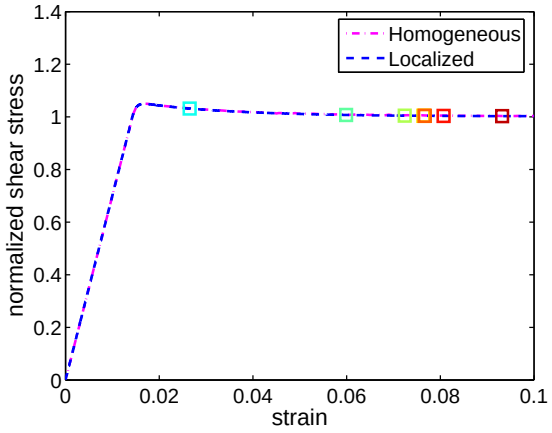

Figure 6.7: Shear stress s vs. strain calculated by numerically integrating the STZ equations of motion with initial conditions $\chi_{ini} = 0.1042$ and $\overline{q} = 8.7 \times 10^{-6}$. The blue curve represents the solution to the perturbed system, while the magenta curve represents a homogeneous solution where the effective temperature is constrained to be constant inside the material. The colored boxes correspond to the plotsshown in Fig. 6.8. Although the localized system weakens slightly faster than the homogeneous system, the effect is small and on this scale the two curves are indistinguishable.

The width of disorder-limited bands is not set by a simple internal length scale such as a. Instead, the width is determined dynamically by the externally imposed strain rate and the initial conditions. Let us assume for the moment that a single shear band forms in the material. This is explicitly enforced for the numerical integration in this chapter because the initial hyperbolic secant perturbation at $y = 0$ leads to a single shear band at that position. In addition, this is what is seen in simulations [40] and numerical integration of random perturbations to the STZ model [70] at low strain rates.

Under this assumption, almost all of the deformation is accommodated in a band of width w:

$$\overline{q} = \tau_0 V_0 / L = (w/L)\, \dot{\gamma}_{band} \tau_0. \tag{6.13}$$

Using Eq. 6.2 and 6.13 we derive the following relationship between the stress s,

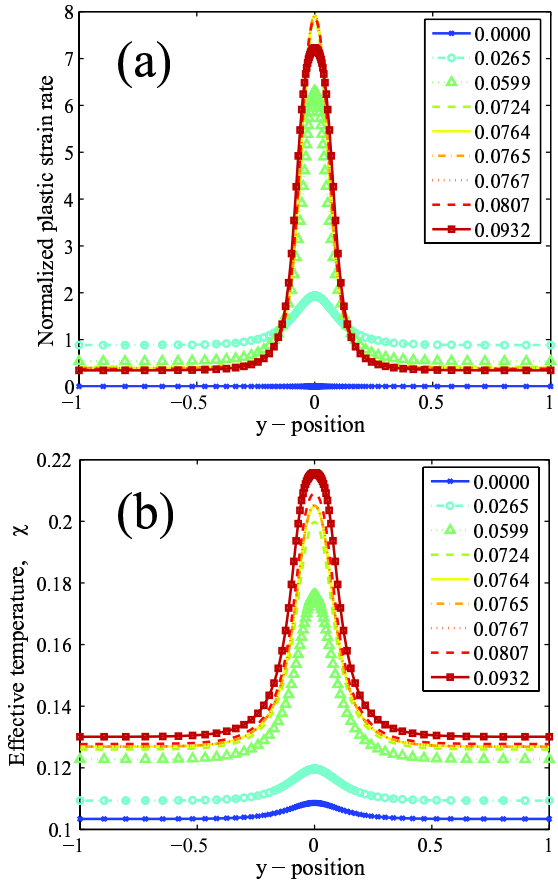

Figure 6.8: **Disorder-limited shear band** (a) Normalized plastic strain rate $\dot{\gamma}(y)\tau_0/\overline{q}$ and (b) effective temperature as a function of position (y), for a material with initial conditions $\chi_{ini} = 0.1042$, and imposed strain rate $\overline{q} = 8.7 \times 10^{-6}$. Different colored lines represent different times; cooler colors (blue) correspond to earlier times, while warmer colors (red) correspond to later times. The plastic strain rate in the band increases significantly (about 800 %), although much less than in the diffusion-limited shear band. The width of this band at its peak is about 0.2, much larger than the width of a diffusion limited shear band.

the width of the shear band w and the externally imposed strain rate $\overline{q}$:

$$\frac{\overline{q}\,L}{w} = 2f(s)\,\exp\left[-\frac{1}{\hat{\chi}(\overline{q}L/w)}\right]. \tag{6.14}$$

This is not a prediction for the width of the shear band, because we have not

specified the final stress, s. Unfortunately, we can not derive an approximate value for s because it depends on the entire history of deformation in the material. In addition, the final value of s is generally close to the yield stress, and $f(s)$ is very sensitive to s in this regime. However, we can check to see if the shear bands in a numerical simulation satisfy the criterion given by Eq. 6.14.

Let $q_{max}(y)$ be the normalized plastic strain rate $\dot{\gamma}(y,t)\tau_0/\overline{q}$ evaluated at the time t_{qmax} when the strain rate achieves its absolute maximum. s_{qmax} is the shear stress at t_{qmax}. The width w_{qmax} of the shear band in a numerical solution is defined to be the fraction of the real line between -1 and 1 where the function $q_{max}(y)$ is sufficiently large:

$$w_{qmax} = \int_s dy, \quad s = \{y \in [-1,\, 1] \mid q_{max}(y) > 1 + h \sup_y q_{max}(y)\}, \tag{6.15}$$

where h is an arbitrary fraction. Although we choose $h = 1/10$, in most cases the calculated width is insensitive to the value of h because the strain rate function is sharply peaked.

Figure 6.9(a) is a plot of the calculated shear band width w_{qmax} as a function of the initial conditions. At high initial effective temperatures when the system deforms homogeneously, the width w_{qmax} is not well-defined. In this case Eq. 6.15 becomes extremely sensitive to the fraction h and is no longer accurate. Data points above the white dashed line in Figure 6.9(a) are in this regime and should not be trusted.

To determine if a shear band width is consistent with disorder-limited deformation, we rearrange Eq. 6.14, and insert w_{qmax} and s_{qmax}:

$$\log\left(\frac{\overline{q}\,L}{2f(s_{qmax})w_{qmax}}\right) + \frac{1}{\hat{\chi}(\overline{q}L/w_{qmax})} = 0. \tag{6.16}$$

A shear band in a numerical solution is said to be "disorder-limited" if Eq. 6.16 is approximately satisfied, (i.e., the left hand side equals 0 ± 0.08.) Similarly, a shear band is "diffusion-limited" if its width is approximately equal to the diffusion length scale a, (i.e. $0 < w_{qmax} < 0.022$). Figure 6.9(b) is a deformation map that indicates where each of these criteria are satisfied.

For the above analysis, we have assumed a single shear band. Experiments and simulations of bulk metallic glasses show that the material develops multiple shear bands at higher strain rates [40, 18]. Developing a model for the number and spacing between shear bands is beyond the scope of this chapter, but the STZ model should provide an excellent starting place for these analyses.

The shear bands that emerge spontaneously in the STZ model capture several important features seen in simulations and experiments. The model predicts a

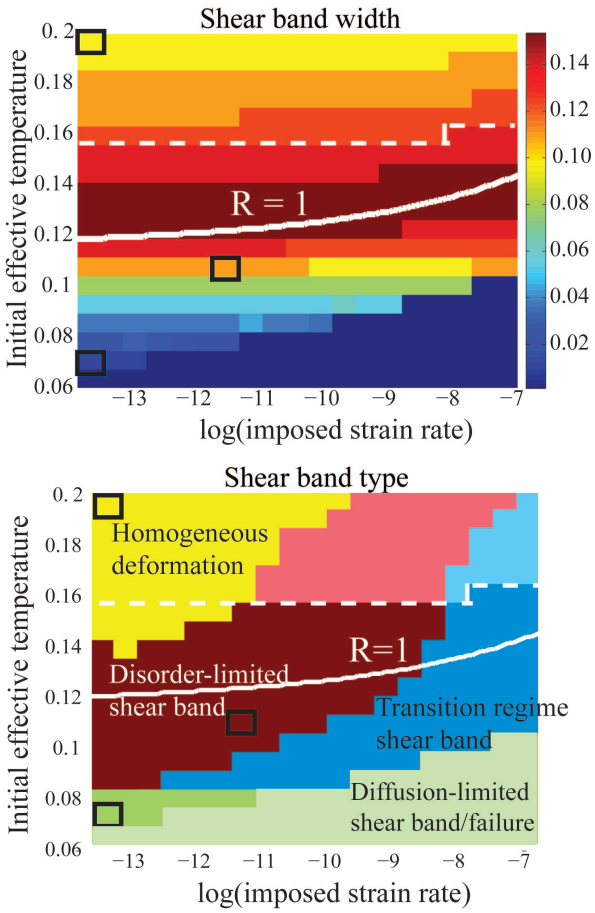

Figure 6.9: (a) Shear band width w_{qmax} (Eq. 6.16) for numerical STZ solutions as a function of the initial conditions χ_{ini} and $\log(\overline{q})$. The shear band width is set to zero when $\chi \to \infty$ during an integration. Black boxes indicate initial conditions detailed in Figs. 6.4, 6.8,and 6.6. Above the white dashed line the system deforms homogeneously and therefore the shear band width is not well-defined. (b) Deformation map that uses the widths shown in (a) to determine if the deformation is diffusion- or disorder-limited localization. Diffusion-limited shear bands (dark green) and failure (light green) occur where $0 \leq w < 0.022$, and disorder limited shear bands (dark red) occur where the left-hand side of Eq. 6.16 < 0.8. The blue region represents a transition regime where the bands are too wide to be diffusion-limited and too small to be disorder limited. The yellow region represents homogeneous flow, and solutions above the dashed line also flow homogeneously.

minimum bound on the shear band width that corresponds to a, the effective temperature diffusion length scale. In bulk metallic glasses this scale should be at most 30 atomic radii, on the order of 10 nm [27], which is much smaller than the thermal diffusion length scale (100-240 nm [20]), and this could explain the shear band width measured in these materials. This also provides an explanation for the scale of the prominent fracture surface, which is orders of magnitude smaller than other length scales in earthquake faults.

For a fixed initial effective temperature, the STZ model predicts that the shear bands become thinner and that their internal structure becomes more disordered as the strain rate increases. This is similar to the "ductile to brittle" transition seen in amorphous materials as a function of the strain rate. At lower strain rates the material deforms nearly homogeneously and appears ductile, but at higher strain rates all the deformation is localized in a thin shear band or mode II crack. At very high strain rates the effective temperature approaches infinity and the system "melts", which is consistent with "brittle" material failure seen at high strain rates in bulk metallic glasses [18].

6.5 Localization and macroscopic rheology

Strain localization has important implications for macroscopic rheology of amorphous materials and friction between interfaces. As discussed in Chapter 1, sliding interfaces are often described using rate-and-state laws, which use a single state variable, θ, to parameterize the internal degrees of freedom of the interface. Similarly, earlier mean-field theory STZ models for amorphous solids use one or two variables (i.e. χ and m) to parameterize the internal system state. Although adding a diffusion term in Eq. 6.8 appears to be a minor change to earlier STZ models, it indicates that the internal state is parameterized by an infinite number of variables: the values of the function $\chi(y)$ at every point.

An important question is whether it is important to model these additional degrees of freedom, and how they impact the macroscopic friction on the fault. Simulations and integration of the STZ model suggest that instabilities drive the system into regimes which are normally inaccessible to homogeneous states. For example, strain rates in very thin shear bands are so high that the solid begins to "melt" and the STZ model fails, which would never happen in homogeneous flow. Moreover, inhomogeneous internal states persist for long times, so that the system requires more than 800% strain to achieve a steady state. These observations emphasize that in at least some cases, an accurate continuum model requires more than just a single internal degree of freedom. Also, because the internal

structural variables evolve very slowly, we must study the transient dynamics in addition to the steady state.

To illustrate this point, we compare a typical steady-state stability analysis for a one-parameter friction model to the localization analysis given in previous sections.

In the literature on earthquake faults, materials are classified as either velocity strengthening or velocity weakening. The velocity dependence parameter, $A - B$, is defined as:

$$A - B \equiv v \left. \frac{ds}{dv} \right|_{v=vss}, \tag{6.17}$$

where v is the velocity, vss is the steady state velocity, and s is the shear stress. This parameter is important because the friction on faults in typically modeled using rate-and-state friction, (i.e. Eq. 1.1). It has been shown that for rate-and-state models, which are ordinary differential equations (ODEs), stick slip events and earthquakes can only initiate in materials which are velocity weakening [91]. If $A - B$ is greater than zero than the material is velocity strengthening and the system is stable with respect to slip, and otherwise it is velocity weakening.

The STZ model also generates a friction law, but because it accounts for the configurational degrees of freedom across the width of the granular material, the friction law is a partial differential equation (PDE) instead of an ODE. An important and nontrivial question is whether the velocity weakening analysis for rate and state models is relevant to the STZ equations.

Recall that the only truly stationary state for the STZ equations is homogeneous flow. In this steady state the governing equations become an ODE, and $A - B$ can be defined using Eq. 6.17. Then the steady state value for χ is simply $\hat{\chi}(\overline{q})$ and Eq. 3.2 can be rewritten as follows:

$$\hat{\chi}(\overline{q}) = -\frac{A_*(\overline{q})}{\ln(\overline{q}/q_*)}, \tag{6.18}$$

where A_* is an activation energy and q_* is a dimensionless constant. Inserting Eq. 6.18 into Eq. 3.3 and taking the derivative with respect to q results in the following equation for $s'(q) \propto ds/dv|_{vss}$:

$$\begin{aligned} s'(q) &= [-1 + A_*(q) + q \ln(q/q_*) A'_*(q))] \\ &\quad \left(\frac{q}{q_*}\right)^{-1/A_*(q)} \frac{1}{A_*(q) f'(s)} \end{aligned} \tag{6.19}$$

The function f increases monotonically with s, because $\mathcal{C}(s)$ is monotonically increasing and $\mathcal{T}(s) - m(s)$ is increasing. Therefore $s'(q)$ is positive and the mate-

rial is steady state velocity-strengthening whenever the factor in brackets is positive. In high strain regimes, the activation energy is a constant, $A_*(q) = A$, and the material is strengthening whenever $A > 1$. For rate-and-state models, stick-slip instabilities can only occur when the system is velocity weakening. Therefore this steady state, homogeneous analysis suggests that stick-slip instabilities are governed by the activation energy A_*, and that no instabilities occur when $A_* > 1$.

However, the STZ effective temperature model is a partial differential equation, and there is no reason that velocity weakening should be required for stick-slip behavior in a PDE. We know from previous sections that the system can develop shear bands, and that band formation coincides with a rapid weakening of the system. In other words, the stress drops much more quickly in a material that exhibits strain localization. It is possible that this rapid weakening associated with shear bands allows stick-slip instabilities; this is an important open question and a direction of future research. Interestingly, the effective temperature instability is not governed exclusively by the velocity weakening parameter. Shear bands occur even when $A_* > 1$, as illustrated by the shear band that occurs for $A_* > 1.5$ shown in Figs. 6.6 and 6.5. However, it is also true that steady state velocity weakening materials are more susceptible to strain localization; χ_{crit} and the localization ratio R are functions of A_* and shear bands occur in a wider parameter range when $A_* < 1$.

While the velocity-weakening parameter is evaluated in steady state, experiments, simulations and models suggest that sheared amorphous systems may never achieve steady state because internal degrees of freedom evolve very slowly. For example, the macroscopic stress calculated using the STZ model (Figure 6.5), appears to reach a steady state quickly (after about 4% strain), but the effective temperature does not reach equilibrium during the integration period (more than 20% strain). This idea is supported by experiments on sheared granular fault gouge. Researchers find that the velocity weakening parameter $A - B$ decreases with increasing slip, indicating that the gouge is not in steady state [4]. They also find that weakening coincides with the formation of shear bands, as predicted by STZ theory. While much remains to be done, these considerations suggest that the velocity-weakening/strengthening parameter does not completely describe the dynamics of materials that exhibit strain localization.

We also note that the transient shear bands might occur in start-up flows of other soft condensed matter systems. In the past, researchers have assumed that in a constant stress geometry, shear bands only occur when the internal state variable is a multi-valued function of the strain rate [52, 88]. However, the above analysis suggests that any model with a positive feedback between structure and deformation rate can develop transient shear bands, and that these bands will

persist if the internal dynamics are sufficiently slow. These type of shear bands have been identified in models for wormlike micelles and polymers [88, 83, 92], and are likely to appear in free volume models for granular materials as well.

6.6 Elastodynamic Rupture Simulations

As mentioned in the previous section, the STZ partial differential equations provide a model for friction between surfaces when the interface is bridged by an amorphous material such as granular fault gouge. Recently, we have used the rate-dependent STZ model to study the effect of strain localization on surface friction and elastodynamic rupture simulations for earthquakes.

In previous studies, we specified the velocity at the boundary, V_0, and used the STZ model to find the deviatoric stress s and the internal state $\chi(y)$. We now study the STZ friction law coupled to a non-inertial single degree of freedom elastic slider, so that the velocity at the boundary evolves dynamically. A layer of gouge of width $2w$ separates two blocks, one of which is pulled by a spring of stiffness k at at velocity V_0. Figure 6.10 is a schematic diagram of this geometry.

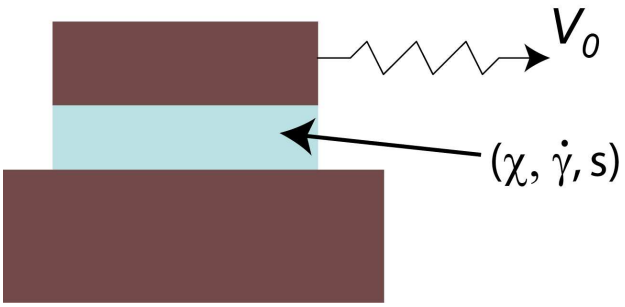

Figure 6.10: Schematic diagram of a spring-slider system. The brown block on top is pulled by a spring, while the bottom block remains at rest. An STZ model is used to describe the amorphous material (blue) between the blocks, assuming no slip boundary conditions.

As in previous sections, the effective temperature has periodic boundary conditions. To mimic the rapid loading and slip acceleration that occurs during dynamic seismic slip, we let $V_0 = 1$ m/s, $k = 100\,000$ M Pa/m. As a first approximation, we disregard the glassy effective temperature dynamics ($\alpha_{eff}(\chi) = 0$) and assume that the system is at high enough strain rates that $\hat{\chi}$ is always simply activated. The activation energy is $A = 0.5$ so that the system is steady state velocity weakening, as described in Section 6.5.

Other STZ parameters include the yield stress scale, $s_0 = 50$ MPa, the STZ rearrangement timescale $\tau_0 = 10^{-6}s$, the diffusion length scale $a = 10^{-5}$ m, and the number of particles that participate in an STZ, $\epsilon_0 = 10$. Daub and Carlson have shown that granular materials are well-described by an STZ rate switching function $R(s)$ which contains only the Eyring component of the rate factor [9]. We adopt their fit for $f(s)$: $f(s) = \exp(-f_0)\cosh(s/s_1)$, where $s_1 = 0.5$ MPa and $f_0 = 118$. We add a small-amplitude symmetric step function perturbation of height $\delta\chi = 2\times10^{-7}$ to the initial conditions for $\chi(y)$, specify the initial deviatoric stress $s_{ini} = 70MPa$ and numerically integrate the STZ equations of motion.

We compare the shear stress as a function of displacement for both dynamically localizing strain and homogeneous strain in Figure 6.11(a). Figures 6.11(b) and 6.11(c) show snapshots of the strain rate in the gouge layer for dynamically localizing strain at a series of representative points. As in the previous numerical simulations (Fig. 6.6), the system develops a diffusion-limited shear band that coincides with a rapid decrease in the shear stress, and the shear band persists for the duration of the numerical simulation.

We next investigate the impact of strain localization on the propagation of spontaneous elastodynamic ruptures. The fault gouge is modeled as a thin layer with half width $w = 1$ m between two homogeneous, isotropic, linear elastic solids of length 2 km. A schematic of this geometry is shown in Fig 1.5(a). Rupture is initiated by a small patch (0.2 km) on the fault with a higher stress, 79 MPa, while the rest of the fault remains at $s_{ini} = 70$ MPa. A spectral boundary integral method is used to integrate the equations of motion in time.

Figure 6.12(a) compares how stress weakens with slip for two ruptures, one which is kept homogeneous by symmetry constraints and the other which spontaneously develops a shear band. Again, the rupture that develops a diffusion-limited shear band weakens much more rapidly. Figure 6.12(b) is a plot of the slip velocity as a function of time for homogeneous and localized deformation. Localized deformation in the 1 m-wide gouge results in delayed rupture front and a much larger peak slip rate compared to homogeneous deformation in the 1 m wide gouge. For comparison, we also calculate responses for systems with thinner fault gouge layers, 0.375m and 0.1 m wide, respectively. Again, we constrain these models so that they deform homogeneously. We find that the localization dynamics can *not* be captured by a thinner homogeneous (ODE) gouge model.

These results show that localization affects the macroscopic dynamics of spring-slider systems and earthquake ruptures. In both cases, localization leads to higher slip rates and a rapid weakening with slip. Although many mechanisms have been suggested for rapid weakening on earthquake faults, including pore pressurization and flash heating at asperity contacts, localization occurs before significant

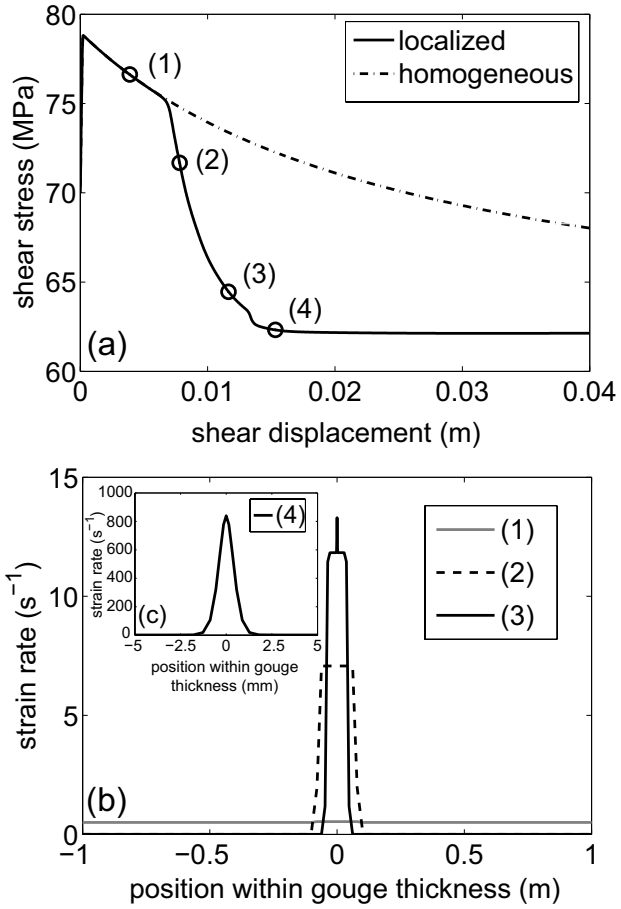

Figure 6.11: (a) Shear stress as a function of displacement for both dynamically localization strain and homogeneous strain. (b) Snapshots of the strain rate in the gouge layer for dynamically localization strain at a series of representative points.(c) Rescaled view of final strain rate profile, which is a thin, diffusion-limited shear band.

changes to the thermal temperature. Thermal and pore pressurization effects likely become important at the high strain rates that occur after the system has localized, and combining these models is an interesting avenue for further research.

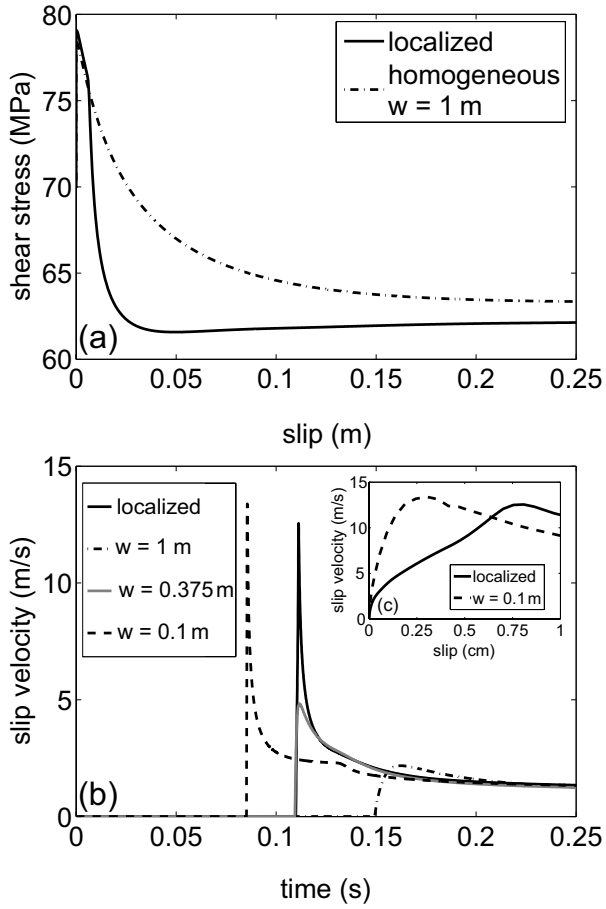

Figure 6.12: (a) Stress vs. slip for two ruptures. The solid line represents a simulation which is kept homogeneous by symmetry constraints and the dashed line is a rupture that spontaneously develops a shear band. Again, the rupture that develops a diffusion-limited shear band weakens much more rapidly. (b) Slip velocity as a function of time for homogeneous and localized deformation

6.7 Conclusions for Chapter 6

In previous sections, we have showed that shear banding in the STZ model results from an instability that occurs during the start-up response when a material is driven from rest. In addition, the dynamics of the internal state $\chi(y)$ becomes very slow, and therefore shear bands persist for long times.

By including information about the rate dependence of the steady state effective temperature, $\hat{\chi}(q)$, we show that the STZ model generates a deformation map

that includes homogeneous deformation, thick "disorder-limited" shear bands, and thin "diffusion-limited" shear bands. The model predicts that at high strain rates the shear band width should be about the size of an STZ, and in extreme circumstances localization can lead to a break down of the solid-like STZ description, "melting", and material failure. In addition, the model predicts a "ductile to brittle" transition as a function of the strain rate and initial conditions.

We have also shown that these localization dynamics can not be captured by a single degree of freedom rate-and-state friction law, and that analyzing steady state model dynamics can often be misleading. This is because the structural degrees of freedom parameterized by $\chi(y)$ evolve much more slowly than the stress dynamics, so that the microstructure continues to evolve although the stress appears to have reached a steady state. This insight is particularly important for materials that develop highly localized shear bands, as the friction law based on homogeneous dynamics is vastly different from one that accounts for transient shear band development.

While this is an exciting starting point for studying deformation and failure for amorphous materials, many fundamental questions remain. We discuss a few of them below.

What is $\hat{\chi}(q)$ for various amorphous materials? Throughout this chapter, we have used a fit to data generated by Haxton and Liu [53] as the definition for $\hat{\chi}(q)$. HL simulated a 2D amorphous packing of harmonically repulsive discs at thermal temperatures above and below the glass transition temperature, and used FDT to extract an effective temperature at each thermal temperature and strain rate. To our knowledge, this is the only such data set. It would be very interesting to use FDT to extract effective temperatures from simulations of other types of amorphous packings, such as the Lennard Jones glass studied by Shi et. al [40], foams, amorphous silicon, or bulk metallic glasses. Is $\hat{\chi}(q)$ similar for all of these materials? Is the effective glass transition temperature, χ_0, universal?

One possibility is that the transition from glassy behavior to simply activated behavior should occur when $q = 1$, (i.e., when the strain rate is the same as the internal rate $1/\tau_0$). However, it is also possible that in complicated materials like bulk metallic glasses, the transition occurs at slower rates than $1/\tau_0$, since the STZs in these systems are large, multi-component regions that likely evolve more slowly than the phonon frequency.

Are there other ways to measure $\hat{\chi}(q)$, such as looking at the behavior of a tracer harmonic oscillator inside a simulation box? Is it possible to define the effective temperature by quantifying the change in configurational entropy as a function of the potential energy? These are important questions because it is very

difficult to measure fluctuations in position or stress precisely enough in experiments to extract an effective temperature using FDT.

What are the effects of geometry and boundary conditions? We have so far restricted ourselves to the simplest possible shear geometry and periodic boundary conditions on the effective temperature. As discussed in detail in Chapter 5, the boundary conditions on the effective temperature help determine the location of shear bands within the material as well as the steady states of the system. In many experiments and in some earthquake faults, shear bands tend to localize along the boundary. Why does this occur?

One suggestion is that an amorphous material adjacent to a rigid solid surface should be modeled by no conduction boundary conditions on the effective temperature, because no disorder can propagate into the rigid solid. Another possibility is that a crystalline solid imposes a constant, more ordered boundary condition on the effective temperature. It would be very interesting to investigate the effects of these conditions on shear band evolution.

In addition, many engineering materials are tested under tension and compression, or a "notch" is placed on the surface of the material. In these cases there is a free boundary which can deform, leading to a coupling between deformation and stress. The necking instability has been investigated using earlier STZ models [93] – it would be interesting to repeat this analysis with our improved understanding of the coupling between structure and deformation.

Are there healing, relaxation, or aging mechanisms not yet included in the STZ model? Currently, the athermal STZ model contains no explicit healing or relaxation mechanisms. Although the steady state effective temperature depends on strain rate, there is no athermal mechanism for the effective temperature to relax below χ_0, even at rest. Even in the thermal STZ formulation no relaxation occurs below the thermal glass transition temperature. The aging seen in a wide variety of glassy materials, as well as stress peaks seen in materials subjected to stop-start experiments, suggests that relaxation terms should be added to the theory.

One possibility is that environmental noise such as vibrations or seismic waves causes fluctuations in the particle positions, activating relaxation. Another possibility is that the STZs are not perfectly degenerate bistable states. Instead, one of the metastable states might have a slightly lower energy, so that even in the absence of stress there is a finite probability that an STZ flips to the lower energy state. This would also lead to relaxation and aging.

Another related question is how the initial effective temperature is determined

by the quench/preparation procedure. Shi et al have shown that the average potential energy per atom decreases (and presumably the effective temperature also decreases) when a simulated glass is quenched more slowly [40]. Can we use a modified STZ theory with relaxation to model the quench process?

What is the lowest possible effective temperature? Haxton and Liu have suggested that for their MD simulation, the effective glass transition temperature χ_0 is the same as the thermal glass transition temperature T_0. If this is true, it is difficult to see how the system could be quenched to state where the initial effective temperature is below χ_0. According to the linear stability analysis presented above, stress peaks and shear bands would not occur in this material. Are there some materials that will not exhibit shear bands because they can not be quenched below χ_{crit}?

Is the localized state weaker in absolute terms than the homogeneous state? Does this matter? Although strain localization leads to a rapid decrease in the shear stress, the final stress state of the localized system is not necessarily lower than the final stress state of a homogeneous system. Fig. 6.11 [89] shows that in the special case where the initial effective temperature perturbation is a step function, the final stress of the localized state is smaller than the homogeneous stress. However, in most numerical solutions to the STZ equations (e.g. Fig. **??**), the final stress state in the localized system is equal to or higher than the stress in the homogeneous system. In absolute terms, the localized system is stronger (or at least no weaker) than the homogeneous system, which is counter-intuitive.

There are several ways to reconcile this information with intuition. First, we note that the *rate* at which the localized system weakens is much more rapid than the homogeneous system. For dynamic phenomena, such as stick-slip instabilities and stop-start experiments, it is possible that the weakening rate is more important than the total stress drop. Another possibility is that many of these systems attain strain rates at which the STZ solid-like description breaks down. Although we don't explicitly model this here, it seems likely that the liquid-like material in the band possess a vastly reduced strength compared to the solid outside the band. Lastly, healing or relaxation mechanisms, discussed above, alter the final stress state. It is possible that relaxation permits the localized systems to weaken further than a homogeneous system, and this is a direction of future research.

Chapter 7

Final Thoughts

Now is an exciting time to study deformation in amorphous systems. New experimental and simulation techniques are generating data that requires theoretical explanation. Faster computers, parallel processing and novel algorithms such as the Bond-Boost method [94] have allowed researchers to simulate larger systems under a wide variety of conditions. Confocal microscopy [95, 96] permits high-fidelity imaging of experimental three-dimensional systems; Scientists can now quantify dynamic heterogeneities in space and time that arise in glassy systems [97, 98]. Static packing experiments and simulations have shed light on the nature of jamming and emphasized the importance of configurational degrees of freedom in jammed systems [99, 64].

In many cases, STZ theory explains new experimental results. As with all good science, some features of experimental and simulation data are not captured by the original formulation, forcing us to re-examine our assumptions and figure out which essential physics needs to be included in the model. STZ captures the dynamics of many (Avogadro's number) degrees of freedom using a few internal state variables and fields (i.e. s and $\chi(y)$); to achieve this simplification we must necessarily neglect some physical processes and hope that they are not important. The success of the STZ model validates this approach. It suggests that in many cases one need not keep track of $F = ma$ for Avogadro's number of particles, and that the large number of particles permits a statistical description of system properties.

Although the STZ formulation is based on the physics of microstructural rearrangements, several parts of the theory have not yet been derived from first principles. For example, the rate function $R(s)$ that describes how STZs flip as a function of the applied shear stress, is not well-constrained. In principle, $R(s)$ could be derived from a complicated many-body calculation, but so far this has re-

mained intractable. Instead, we recognize that physical principles constrain $R(s)$ in the limits of large and small stresses, and interpolate between these extremes. Although these types of assumptions are necessary to make any progress at all, we should be explicit about when we make them. In addition, STZ theory could be further improved by re-examining these assumptions and validating them using careful comparisons to experiments and simulations.

Overall, STZ theory is incredibly useful because it is one of the few models that generates a physics-based, Navier-Stokes like description for deformation in amorphous solids. Because it is based on microscopic physics instead of a fit to data, this model is applicable to a wide range of materials and environmental conditions – from quasi-static deformation in bulk metallic glasses to rapid slip on earthquake faults. In this work we have shown that the STZ model captures important features of amorphous materials and makes novel predictions for macroscopic system response. We first present a synopsis of these results, and then discuss open questions and future directions.

7.1 Synopsis

Amorphous materials are found in many natural and industrial applications, and yet engineers have lacked a basic theoretical continuum framework for describing them. Although their dynamics are complex and multi-scale, the microscopic structure of these materials is simple and fluid-like. By using minimal microscopic models that capture the basic physics of glassy, jammed systems, we have been able to develop continuum equations for deformation in these materials.

The previous chapters outlined a framework for understanding deformation in amorphous solids. In Chapter 3 we developed an STZ theory to describe the steady state dynamics of an amorphous, glassy system above and below the thermal glass transition temperature. We found that the effective temperature is an important state variable for describing the system and that the strain rate is activated by the effective temperature. In fact, the nondimensionalized strain rate q is simply activated at high effective temperatures, but at low effective temperatures the activation energy is super-Arrhenius, much like the viscosity as a function of thermal temperature. In Chapter 4 we demonstrated that STZ models involving the free volume as an activation parameter (instead of the effective temperature) result in nearly the same continuum description. This suggests that athermal experiments which probe macroscopic properties can be described equally well by either formulation.

We have also shown that the microstructural dynamics have dramatic con-

sequences for macroscopic material properties. Chapter 5 focuses on the low-temperature, low strain rate limit. In this regime, when the effective temperature field is permitted to vary within the material (by introducing slightly heterogeneous initial conditions), the system spontaneously develops shear bands. The shear bands arise due to an interesting "frozen-time" instability that occurs during the transient STZ dynamics, and this explains the existence of shear bands in athermal or low-temperature materials such as granular fault gouge.

In Chapter 6 we show that when this instability is combined with the rate-dependent $\hat{\chi}$ discussed in Chapter 3, the resulting shear bands can be very thin. This suggests that failure in amorphous materials such as bulk metallic glasses is caused by an effective temperature shear band instability. Prominent fracture surfaces seen in earthquake faults might result from a similar instability, which has important implications for friction on these faults.

In this work, we have shown that an STZ theory with effective temperature explains universal features of amorphous systems across a broad range of scales. In the future, we hope that this framework will lead to better multi-scale predictions for friction and material failure.

7.2 Open Questions

While the aforementioned results are exciting, there is still much to be done. An important open question is whether the effective temperature measured by FDT comparisons also describes the distribution of configurational packings. Ono *et al.* have presented simulation data suggesting this is true, but only in a homogeneously deforming system. It would be interesting to insert a harmonic oscillator into simulations to study the *local* fluctuations. In simulations with shear bands, does such a local "thermometer" read a higher effective temperature inside the bands? From an alternate perspective, it is possible to characterize the *local* entropy of configurational packings? Donev *et al.* suggest a binning method for determining local configurational entropy in static packings [99]. It would be informative to compare this measure of local configurational entropy to local FDT results in simulations.

We have used STZ theory to describe sheared systems. In many studies, the system is permitted to age without any applied shear forces. Experiments have shown that even below the thermal glass transition temperature, material properties change over time. In the absence of shear forces, the STZ equations as written in Chapter 2 exhibit no aging below the thermal glass transition temperature. As discussed in Section 6.7, there are two ways to modify the STZ model

to include aging: the first is to add an additional relaxation term to the effective temperature, much like the FV law in Chapter 4. This relaxation term could model sources of external vibrational noise, such as seismic waves in granular fault gouge, or other chemical effects (such as sedimentation). Daub [100] has seen that a relaxation (or *healing*) term generates pulses in earthquake rupture simulations. Alternatively, modeling STZs as regions with two degenerate stable states and a single characteristic yield stress is a caricature of reality. Langer [57] has developed an STZ formulation that accounts for a distribution of STZ yield stresses. It would be exciting to generalize this model to account for not-quite-degenerate STZ states, as the resulting system might exhibit aging as STZs return to their lowest energy states.

Questions also remain about shear band phenomenology. Shi *et al.* [40] and Hays *et al.* [17] find that amorphous systems begin to develop multiple shear bands at the highest strain rates, but there is no theoretical explanation for the onset of multiple bands. The effective temperature STZ formulation provides a framework for analyzing and predicting the number and spacing of shear bands.

An additional open question regarding shear bands is what determines their location within a material. In simulations with periodic boundary conditions, (and in the STZ equations with periodic BCs on the effective temperature), the shear bands generally occur at the same frequency everywhere in the solid [70, 40]. As discussed at the end of Chapter 5, Varnik et al [41] have shown that in simulations with rough no-slip boundary conditions, shear bands occur right along the boundary. In addition, Shi and Falk have shown that shear bands tend to localize around notches or flaws in the amorphous material [86], indicating that boundary conditions play an important role in strain localization. It would be interesting to investigate the effects of various boundary conditions on the effective temperature, such as no conduction or constant effective temperature, to see if the model can recover/explain these phenomena.

7.3 Future Directions

In the past, friction on earthquake faults and nanomachine controllers have been modeled using either 1) a linear slip weakening law, which is a simple constraint that relates stress to strain rate, or 2) a rate-and-state law, which is a coupled set of ODEs that relate stress to strain and an internal variable, θ. We have shown that by accounting for the internal degrees of freedom in the granular material – essentially assuming that the material has a finite thickness with material properties that can vary across the width – one can predict the exis-

tence of a prominent fracture surface and dynamic weakening. This is interesting, because many researchers in the friction and earthquake communities use the rate-and-state law (Eq. 1.1) to characterize their experimental results and make predictions for earthquake ruptures.

For example, it has been shown that for a rate-and-state friction law, earthquakes and stick slip instabilities can only initiate in regions that are velocity weakening [91]. However, if one replaces the rate-and-state ordinary differential equations by the effective temperature partial differential equations, this result no longer holds. Shear band formation is a dynamic instability that prevents the granular system from ever reaching a steady state. Therefore terms such as "velocity weakening", which are only defined in steady state, do not reveal much about the system dynamics. It is possible that granular degrees of freedom and their associated dynamics generate stick slip behavior even in regions that are not "velocity weakening" in steady state. This is a particularly interesting avenue for research – one that might fundamentally change how we understand friction on lubricated or granular surfaces.

The non equilibrium statistical mechanics approach used to develop the STZ model might be useful in other situations. Large, non equilibrium systems generally have a huge number of degrees of freedom. However, if the system maintains a steady state, one can usually identify extensive variables (such as the volume or potential energy) that are conserved. By associating the conserved quantity with an extensive entropy, we can define an intensive state variable which is the derivative of the entropy with respect to the conserved quantity, and this state variable is an excellent candidate for use in continuum descriptions. In addition, the STZ model coarse grains the system by identifying small regions where deformation takes place. The paradigm of coarse graining a system using its dynamic properties instead of physical locations is interesting and probably widely applicable.

One situation where these approaches might prove useful is in continuum models for the mechanics of biological tissues. Tissues are composed of many individual cells, which interact chemically and mechanically. By identifying internal state variables such as the stress, configurational disorder, and morphogen concentration, and coarse graining the system by identifying regions of high deformation, chemical activity, or reproductive rates, one could develop a set of equations for tissue development.

Bibliography

[1] J. Dieterich, Pure and Applied Geophys. **116**, 790 (1978).

[2] A. Ruina, J. of Geophys. Res. **88**, 10359 (1983).

[3] J. H. Dieterich and B. D. Kilgore, Tectonophysics **256**, 219 (1996).

[4] C. Marone, Annual Reviews in Earth and Planetary Sciences **26**, 643 (1998).

[5] G. D. Toro, D. L. Goldsby, and T. E. Tullis, Nature **427**, 436 (2004).

[6] K. Xia, A. J. Rosakis, and H. Kanamori, Science **303**, 1859 (2004).

[7] X. Lu, N. Lapusta, and A. J. Rosakis, Proceedings of the National Academy of Sciences **104**, 18931 (2007).

[8] E. M. Dunham and R. J. Archuleta, Geophysical Research Letters **32**, L03302 (2005).

[9] E. Daub and J. M. Carlson, submitted to J. Geophys. Res. (2007).

[10] N. Lapusta and J. R. Rice, Journal of Geophysical Research **108**, 2205 (2003).

[11] R. G. Horn and J. N. Israelachvili, The Journal of Chemical Physics **75**, 1400 (1981).

[12] J. N. Israelachvili, P. M. Mcguiggan, and A. M. Homola, Science **240**, 189 (1988).

[13] M. L. Gee, P. M. McGuiggan, J. N. Israelachvili, and A. M. Homola, The Journal of Chemical Physics **93**, 1895 (1990).

[14] M. Schoen, C. L. Rhykerd, D. J. Diestler, and J. H. Cushman, Science **245**, 1223 (1989).

[15] H. Yoshizawa, P. McGuiggan, and J. Israelachvili, Science **259**, 1305 (1993).

[16] H. Yoshizawa and J. Israelachvili, Journal of Physical Chemistry **97**, 11300 (1993).

[17] C. C. Hays, C. P. Kim, and W. L. Johnson, Physical Review Letters **84**, 2901 (2000).

[18] J. Lu, G. Ravichandran, and W. Johnson, Acta Mater. **51**, 3429 (2003).

[19] D. Griggs and D. Baker, Properties of Matter Under Unusual Conditions. Wiley/Intersciences, New York , 23 (1969).

[20] J. Lewandowski and A. Greer, Nat. Mater. **5**, 15 (2005).

[21] J.-C. Tsai and J. P. Gollub, Phys. Rev. E **72**, 051304 (2005).

[22] D. Fenistein and M. Van Hecke, Nature **425**, 256 (2003).

[23] J. Lauridsen, M. Twardos, and M. Dennin, Phys. Rev. Lett. **89**, 098303 (2002).

[24] A. Kabla and G. Debrégeas, Phys. Rev. Lett. **90**, 258303 (2003).

[25] R. Mair and P. Callaghan, Europhys. Lett. **36**, 719 (1996).

[26] R. Makhloufi, J. Decruppe, A. Ait-Ali, and R. Cressely, Europhys. Lett. **32**, 253 (1995).

[27] W. Johnson, J. Lu, and M. Demetriou, Intermetallics **10**, 1039 (2002).

[28] C. Marone, C. Raleigh, and C. Scholz, J. Geophys. Res **95**, 7007 (1990).

[29] F. M. Chester and J. S. Chester, Tectonophysics **295**, 199 (1998).

[30] M. L. Falk, M. Toiya, and W. Losert, 0802.1752 (2008).

[31] G. Tarjus and D. Kivelson, *The viscous slowing down of supercooled liquids and the glass transition: phenomenology, concepts, and models*, chapter Model Uncertainty: Probabilities for Models?, Taylor and Francis Inc., New York, 2001.

[32] A. J. Liu, S. R. Nagel, and A. J, *Jamming and Rheology: Constrained Dynamics on Microscopic and Macroscopic Scales*, CRC Press, 2001.

[33] M. Wyart, S. Nagel, and T. Witten, Europhysics Letters **72**, 486 (2005).

[34] S. Henkes, C. S. O'Hern, and B. Chakraborty, Physical Review Letters **99**, 038002 (2007).

[35] A. Mehta and S. Edwards, Physica A **157**, 1091 (1989).

[36] D. Chandler, *Introduction to Modern Statistical Mechanics*, Oxford University Press, New York, 1987.

[37] L. Cugliandolo, J. Kurchan, and L. Peliti, Phys. Rev. E **55**, 3898 (1997).

[38] I. K. Ono et al., Phys. Rev. Lett. **89**, 095703 (2002).

[39] N. Xu, C. S. O'Hern, and L. Kondic, Phys. Rev. E **72**, 041504 (2005).

[40] Y. Shi, M. B. Katz, H. Li, and M. L. Falk, Physical Review Letters **98**, 185505 (2007).

[41] F. Varnik, L. Bocquet, J.-L. Barrat, and L. Berthier, Phys. Rev. Lett. **90**, 095702 (2003).

[42] M. Bazant, Mech. of Mater. **38**, 717 (2006).

[43] P. Sollich, F. Lequeux, P. Hébraud, and M. Cates, Phys. Rev. Lett. **78**, 2020 (1997).

[44] F. Spaepen, Acta Metall. **25**, 407 (1977).

[45] A. Argon, Acta Metall. **27**, 47 (1979).

[46] V. V. Bulatov and A. S. Argon, Model. Simul. Mater. Sci. Eng. **2**, 1994 (1994).

[47] M. Falk and J. Langer, Phys. Rev. E **57**, 7192 (1998).

[48] M. Falk and J. Langer, MRS Bull. **25**, 40 (2000).

[49] L. Pechenik, Phys. Rev. E **72**, 021507 (2005).

[50] E. Bouchbinder, J. Langer, and I. Procaccia, Phys. Rev E **75**, 036108 (2007).

[51] A. Lemaitre, Phys. Rev. Lett. **89**, 195503 (2002).

[52] J. Langer, Phys. Rev. E **70**, 041502 (2004).

[53] T. K. Haxton and A. J. Liu, Physical Review Letters **99**, 195701 (2007).

[54] A. Lemaître and J. Carlson, Physical Review E **69**, 061611 (2004).

[55] C. E. Maloney and A. Lemaitre, Physical Review E (Statistical, Nonlinear, and Soft Matter Physics) **74**, 016118 (2006).

[56] A. S. Argon and M. J. Demkowicz, Philosophical Magazine **86**, 4153 (2006).

[57] J. S. Langer, Physical Review E **77**, 021502 (2008).

[58] R. Bagnold, Proc. R. Soc. London **255** (1954).

[59] J. S. Langer and M. L. Manning, Physical Review E **76**, 056107 (2007), Copyright (2007) by the American Physical Society.

[60] P. Sollich, F. Lequeux, P. Hebrand, and M. E. Cates, Phys. Rev. Lett. **78**, 2020 (1997).

[61] L. Berthier and J.-L. Barrat, Phys. Rev. Lett. **89**, 095702 (2002).

[62] L. Berthier and J.-L. Barrat, The Journal of Chemical Physics **116**, 6228 (2002).

[63] J.-L. Barrat and L. Berthier, Physical Review E **63**, 012503 (2000).

[64] C. O'Hern, A. Liu, and S. Nagel, Phys. Rev. Lett. **93**, 165702 (2004).

[65] P. Ilg and J.-L. Barrat, EPL (Europhysics Letters) **79**, 26001 (2007).

[66] E. Bouchbinder, J. Langer, and I. Procaccia, Phys. Rev E **75**, 036107 (2007).

[67] J. S. Langer, Physical Review E **73**, 041504 (2006).

[68] J. S. Langer, Physical Review Letters **97**, 115704 (2006).

[69] M. Cross, Journal of Colloid Science **20**, 417 (1965).

[70] M. L. Manning, J. S. Langer, and J. M. Carlson, Physical Review E **76**, 056106 (2007).

[71] J. Rottler, private communication, 2008.

[72] T. Haxton and A. Liu, private communication, 2007.

[73] E. Bouchbinder, 0801.4131 (2008).

[74] Y. Shi and M. L. Falk, Physical Review B (Condensed Matter and Materials Physics) **73**, 214201 (2006).

[75] C. Maloney and A. Lemaître, Phys. Rev. Lett. **93**, 195501 (2004).

[76] S. Braeck and Y. Y. Podladchikov, Physical Review Letters **98**, 095504 (2007).

[77] G. Lois, A. Lemaître, and J. Carlson, Phys. Rev. E **72**, 51303 (2005).

[78] Lifshitz and Pitaevskii, *Statitical Physics 3rd Edition Part 1*, Pergamon Press, Elmsford, N.Y., 1980.

[79] P. Jop, Y. Forterre, and O. Pouliquen, Nature **441**, 727 (2006).

[80] M. Urbakh, J. Klafter, D. Gourdon, and J. Israelachvili, Nature **430**, 525 (2004).

[81] A. Foglia, arXiv **cond-mat/0608451** (2006).

[82] R. Huang, Z. Suo, and W. Prevost, J.H.and Nix, J. of the Mech. and Phys. of Solids **50**, 1011 (2002).

[83] S. M. Fielding and P. D. Olmsted, Phys. Rev. Lett. **90**, 224501 (2003).

[84] A. Foglia, *Shear Localization in the Shear Transformation Zone theroy of plasticity in amorphous systems*, PhD thesis, University of California, Santa Barbara, 2006.

[85] C. Damgaard, Gini coefficient, Technical report, From MathWorld – A Wolfram Web Resource, created by Eric W. Weisstein, 2007.

[86] Y. Shi and M. Falk, private communication, 2006.

[87] M. Falk and Y. Shi, Mat. Res. Soc. Proc. **754**, 20 (2003).

[88] C.-Y. D. Lu, P. D. Olmsted, and R. C. Ball, Phys. Rev. Lett. **84**, 642 (2000).

[89] E. G. Daub, M. L. Manning, and J. M. Carlson, submitted to Geophys. Res. Lett. (2007).

[90] I. Cohen, B. Davidovitch, A. B. Schofield, M. P. Brenner, and D. A. Weitz, Physical Review Letters **97**, 215502 (2006).

[91] J. Rice, Pure and Applied Geophysics **121**, 443 (1983).

[92] J. M. Adams and P. D. Olmsted, 0805.0679 (2008).

[93] L. O. Eastgate, J. S. Langer, and L. Pechenik, Phys. Rev. Lett. **90**, 045506 (2003).

[94] W. K. Kim and M. Falk, private communication, 2008.

[95] A. Dinsmore, E. Weeks, V. Prasad, A. Levitt, and D. Weitz, Applied Optics **40**, 4152 (2001).

[96] U. Gasser, E. Weeks, A. Schofield, P. Pusey, and D. Weitz, Science **292**, 258 (2001).

[97] R. E. Courtland and E. R. Weeks, Journal of Physics Condensed Matter **15**, 359 (2003).

[98] L. J. Kaufman and D. A. Weitz, The Journal of Chemical Physics **125**, 074716 (2006).

[99] A. Donev, F. H. Stillinger, and S. Torquato, Physical Review Letters **96**, 225502 (2006).

[100] E. G. Daub, private communication, 2008.